THESIS FOR THE DEGREE OF DOCTOR OF PHILOSOPHY

Tunable superconducting resonators

Subharmonic oscillations and manipulation of microwaves

IDA-MARIA SVENSSON

Quantum Technology Laboratory
Department of Microtechnology and Nanoscience (MC2)
Chalmers University of Technology
SE-412 96 Göteborg
Sweden
Telephone: +46 (0)31-772 1000

Cover:
A histogram illustrating period tripling subharmonic oscillations with an additional probe signal applied slightly detuned from the measurement freqeuncy.

Tunable superconducting resonators
Subharmonic oscillations and manipulation of microwaves
Thesis for the degree of Doctor of Philosophy
IDA-MARIA SVENSSON
Department of Microtechnology and Nanoscience (MC2)
Chalmers University of Technology

Abstract

In this thesis I present different types of manipulations of microwave fields using tunable superconducting resonators. A resonator is made tunable by adding one or more superconducting quantum interference devices, SQUIDs. The SQUID consists of a superconducting loop with two Josephson junctions and acts as a tunable nonlinear inductor. Modulation of the SQUID nonlinearity can be performed to induce different types of non-trivial oscillator dynamics.

The first project I present is on subharmonic oscillations. Here, the SQUID in a tunable resonator is driven with an external signal at an integer multiple of the frequency ω. When ω is placed slightly below the first resonator mode, I show generation of radiation at ω, which is known as frequency down-conversion. In my measurements, subharmonic oscillations have been detected from period doubling up to period quintupling. For the specific case of period tripling, theory is developed and I show good agreement between theory and experiments.

The second project of the thesis is on a doubly tunable resonator. Here, I show creation of a superconducting resonator with two independently tunable boundary conditions. The idea with this system is to operate the resonator in a breathing or a translational mode and compare the two. For static dc magnetic flux the performance is very good. As a second step, I perform fast modulation of both SQUIDs to generate radiation. Even though some of the measurement results are promising, I also show some contradicting observations. These indicate that the actual modulation mechanism of the SQUID is not pumping of the magnetic flux in the SQUID loop as intended, but rather direct current driving of the SQUID. However, the system remains a promising idea for microwave manipulation and creation of interesting non-classical states.

As a possible application of the doubly tunable resonator, I present a theory proposal on how to use it for measurements on relativistic effects. By using the tunability of the resonator boundary conditions, the resonator can simulate a space rocket and time dilation could be measured. However, due to the crosstalk problems in the doubly tunable resonator this experiment was never realized.

Finally, I finish the thesis by presenting a design for a tunable microwave coupling. Papers E and F show a high on-off ratio for the coupler and demonstrate how it can be used for storage of microwave signals. Furthermore, the tunable coupler can be used to shape a microwave signal by tuning the strength of the coupling.

Keywords: subharmonic oscillations, parametric oscillations, frequency down-conversion, driven nonlinear systems, superconducting resonator, tunable resonator, SQUID, circuit-QED, microwave manipulation

Till farmor för din nyfikenhet som inspirerat mig att alltid vilja veta lite mer och till mormor för att du med din envishet övertygat mig om att allt är möjligt.

To my most loyal support, my family, sincerest thanks. Till mamma och pappa, tack för att ni stöttar och på något självklart sätt alltid tar för givet att jag klarar allt. Tack Mikael, min bror, vi har inte alltid varit sams men du är helt klart en stöttepelare i mitt liv. Till min extrafamilj, Marie, Kurt, Jimmy och Emil, tack för att ni får mig att känna mig hemma även hos er. Till släkten, en trofast skara människor som jag vet alltid finns där i vått och torrt, ni ger mig trygghet.

The last thought goes to the person who, apart from me, has experienced the most of my PhD mood swings. Simon, I think you are happy this is over. Tack för att du står med fötterna på jorden stabilt vid min sida, du tar bort bubblan i min kompass och hjälper mig styra rätt.

Ida-Maria Svensson, Trollhättan, 28/2-2018

List of publications

This thesis is based on the work contained in the following papers:

Paper A   I.-M. Svensson, A. Bengtsson, P. Krantz, J. Bylander, V. Shumeiko, and P. Delsing. Period-tripling subharmonic oscillations in a driven superconducting resonator. *Physical Review B* **96**: 174503, 2017

Paper B   I.-M. Svensson, A. Bengtsson, J. Bylander, V. Shumeiko, and P. Delsing. Period multiplication in a parametrically driven superconducting resonator. *Submitted manuscript.* arXiv: `1802.09259`

Paper C   I.-M. Svensson, M. Pierre, M. Simoen, W. Wustmann, P. Krantz, A. Bengtsson, J. Bylander, V. Shumeiko, and P. Delsing. Microwave photon generation in a doubly tunable superconducting resonator. *Journal of Physics: Conference series* **969**: 1146, 2018

Paper D   J. Lindkvist, C. Sabín, I. Fuentes, A. Dragan, I.-M. Svensson, P. Delsing, and G. Johansson. Twin paradox with macroscopic clocks in superconducting circuits. *Physical Review A* **90**: 052113, 2014

Paper E   M. Pierre, I.-M. Svensson, S. Raman Sathyamoorthy, G. Johansson, and P. Delsing. Storage and on-demand release of microwaves using superconducting resonators with tunable coupling. *Applied Physics Letters* **104**: 232604, 2014

Paper F   M. Pierre, S. Sathaymoorty, I.-M. Svensson, P. Delsing, and G. Johansson. Resonant and off-resonant microwave signal manipulations in coupled superconducting resonators. *Submitted manuscript.* arXiv: `1802.09034`

Other papers that are outside the scope of this thesis:

Paper I   A. Bengtsson, P. Krantz, M. Simoen, I.-M. Svensson, B. H. Schneider, V. Shumeiko, P. Delsing, and J. Bylander. Nondegenerate parametric oscillations in a tunable superconducting resonator. *Submitted manuscript.* arXiv: `1801.04566`

Paper II   B. H. Schneider, A. Bengtsson, I.-M. Svensson, T. Aref, G. Johansson, J. Bylander, and P. Delsing. Observation of broadband entanglement in radiation from the dynamical Casimir effect. *Submitted manuscript.* arXiv: `1802.05529`

CONTENTS

Thesis

1

Introduction

In 1900, Max Planck studied the spectrum of radiation emitted by a black body in thermal equilibrium. He presented the idea that energy only could be emitted in multiples of elementary units, $E = \hbar\omega$, where $\hbar$ is Planck's constant and ω the radiating frequency [9]. These discrete packages, or quantas of energy were later named photons [10]. Since photons are quantas of electromagnetic energy, their propagation is governed by Maxwell equations for electromagnetic waves. However, when Einstein was explaining the photoelectric effect, he used the theory proposed by Planck about discrete energy packages and treated the light as particles to explain the effect [11]. It was found that photons could be treated both as particles and as waves, the particle-wave duality.

Photons are very fast moving objects, and to interact with them, it is convenient to trap them. This can be done in cavities. A simple cavity is formed by two mirrors placed opposite to each other, where the photons bounce back and forth. Within the cavity, the photons can interact with for instance an atom under controlled conditions. The field studying the interaction between light and matter confined in a cavity is called cavity quantum electrodynamics, cavity QED [12].
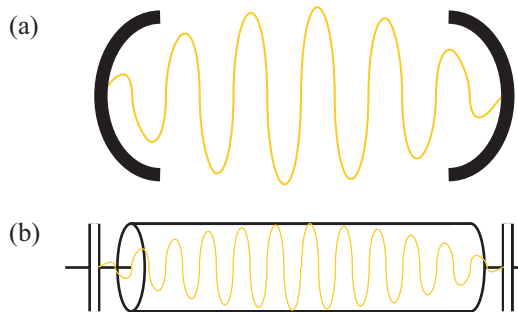
Figure 1.1: *(a) Sketch of a Fabry-Perot cavity that confines optical photons between two mirrors. (b) Sketch of a superconducting transmission line resonator where the microwave photons are confined between two capacitors that act as semi-transparent mirrors.*

In this thesis, the cavities used are microwave transmission line resonators. A piece of microwave transmission line placed between two capacitors resembles a cavity with two semi-transparent mirrors for the electromagnetic field, see Fig. 1.1, replacing the optical cavities with microwave resonators, optical photons with microwave photons, and natural atoms by artificial atoms. The microwave photons are excitations of the electromagnetic field and form the research field of circuit QED [13–16]. The circuits allow for large flexibility, with properties that can be designed using a wide parameter range. In circuitry acting as atoms, energy levels can be tailor made. These atoms are also known as quantum bits, qubits, the building blocks of a quantum computer.

Circuit QED is a promising approach to build a larger quantum network, such as a quantum computer. In these networks, basic components are needed for storing the quantum information. This is in addition to more complicated circuitry to implement quantum algorithms. In this thesis, I use circuit QED to manipulate microwave fields. My contribution to future quantum networks consists of three different systems. Two of the systems, the subharmonic oscillator and the doubly tunable resonator, rely on frequency down-conversion. In these experiments I apply a modulation signal at a given frequency and detect radiation at subharmonics of this modulation frequency. When operated in the quantum regime, the generated radiation could form interesting non-classical states, potentially useful for continuous variable quantum information processing. The third system is a resonator with a tunable external coupling. By turning off the coupling to a fixed frequency resonator, quantum information can be stored in the resonator. A similar tunable coupler could also be designed between quantum bits.

All three systems rely on one key element, the tunable superconducting resonator [17, 18]. A resonator is made tunable by adding a superconducting quantum interference device, SQUID. The SQUID is essentially a tunable nonlinear inductance that can be used to create nonlinear as well as non-classical effects. It also establishes a coupling between the different resonator modes [19]. This coupling can, for instance, be used to create entanglement between resonator modes [20].

This thesis consists of five chapters which give the background of the appended papers and provide a broader view of our results. In addition, I have tried to include interesting material that is unpublished at the time of writing this thesis.

In chapter 2, I introduce the theoretical framework needed to analyse and understand the measurement results. Here, I introduce the key element of the thesis, the tunable resonator. In this chapter, there are two parts which I explore in detail. One is the derivation of the energy spectra of the tunable resonators. This is essential to understand my measurement results that are consequences of interaction between modes. The other detailed derivation is the theory behind the third order subharmonic oscillations. Although this derivation exists in Paper A, the version included in the thesis is more detailed and easier to follow. Furthermore, I present the equations of parametric pumping for a regular single SQUID tunable resonator as well as the doubly tunable resonator. These equations are useful for understanding the results of Paper C. I briefly review the experimental aspect of measuring the twin paradox in a doubly tunable resonator, the detailed calculations are found in Paper D. Finally, I introduce how a tunable resonator can be used as a tunable coupling for the microwave field, the system treated in Papers E and F.

The technical details of the fabrication and measurements are outlined in chapter 3.

Parts of this chapter are rather technical, but are also of high importance for ensuring the accuracy, reliability and repeatability of measurements. I start by briefly describing the different fabrication techniques used. Then I explain how the samples are installed in a measurement setup. Furthermore, I introduce some measurement techniques and discuss some elements of the circuit design.

Measurement results are presented in chapter 4. Here, I first go through the resonator characterization in more detail than what was done in the papers. Among other things, I show dc tuning measurements on the doubly tunable resonators for different flux pump line designs. Then I describe the interesting results that did not fit in Paper A or B due to space limitations. Here, you find a library of measurements from different samples and flux bias values. There is also a discussion on more technical aspects of the measurement results.

The second part of the SQUID modulation treats parametric pumping at two times the resonance frequency. As a reference I show a regular parametric oscillator. Then I continue by reviewing some complementary measurement results from the doubly tunable resonator that did not fit in Paper B. In the final section of chapter 4, I review the most important findings of the tunable coupling system.

In the last chapter of the thesis, I summarise and discuss the outlook of the different systems. Here, I comment on the weaknesses and strengths of the systems and highlight some possible future routes of the projects.

2

Theory

This chapter is an introduction to all the different theoretical concepts needed to understand the results of the thesis. First, I introduce the basic concepts of superconductivity and the microwave resonator. Some portions of this chapter are expanded over and beyond my master thesis [21]. This introduction leads to the key element of the thesis, the tunable superconducting resonator, which is described in detail in section 2.3. Here I have included the full derivations of the energy spectra for the main resonator types used in the thesis.

Then I go through the theory of different types of microwave manipulation and frequency conversion techniques investigated. Section 2.4 gives the background on different types of fast modulation of the SQUID current or flux. This section covers the derivation of the subharmonic oscillations [1] and the theory for the doubly tunable resonator [3]. Derivations of parametric frequency conversion and the parametric oscillator are not included in this thesis but can be found elsewhere [22–25]. Finally, the section 2.5 gives a short introduction to the tunable coupling circuit.

2.1   Superconductivity

A superconductor is a material where current can flow without resistance. Entering the superconducting regime, many electrical components benefit highly from decreased losses, both for low and high frequency applications [26].

In 1911, H. K. Onnes found the superconducting transition in mercury [27]. Cooling mercury to liquid helium temperature he observed a significant drop in electrical resistivity. The temperature, at which the transition occurs, is called the critical temperature, and at this temperature the electrons start to pair up into Cooper pairs [28]. A Cooper pair consists of two electrons which attract each other as a result of electron-phonon interaction. In a crude picture, this can be explained by the fact that electrons are very light and fast, compared to the heavy metal ions. When a fast electron is passing through a metal ion lattice, the slow but positively charged ions are attracted and move closer together, forming a positively charged region attracting the other electron. The theory explaining
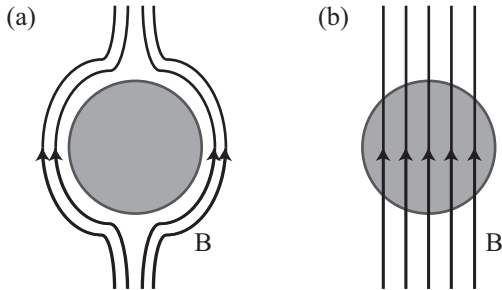
Figure 2.1: *(a) In a superconductor, the applied magnetic field is expelled due to the Meissner effect. (b) In a perfect conductor, the applied magnetic field penetrates the conductor.*

the electron pairing mechanism in conventional superconductors is called BCS-theory after its founders Bardeen, Cooper and Schrieffer [29].

Electrons are fermions and therefore spin up electrons are only allowed to pair with spin down electrons due to the Pauli principle. Furthermore, when the electrons form Cooper pairs, these pairs become bosons. Therefore, the Cooper pairs can condense into a single quantum state $\Psi = \sqrt{n}e^{i\theta}$, where θ is the superconducting phase, and $\Psi\Psi^* = n$ the Cooper pair density. The minimum energy required to break up a pair is the superconducting gap energy $2\Delta_{BCS}$. The superconducting gap is a feature of the superconductor density of states, which is formed by two energy bands symmetrically around the Fermi energy. The distance between the bands is $2\Delta_{BCS}$. This energy difference gives the threshold for single particle excitations. Another property of the Cooper pairs is that they cannot transfer heat. This is very useful in experimental setups to thermally isolate between different temperature stages.

The most commonly used superconducting materials are aluminium, niobium, tin and lead. These materials have critical temperatures that ranges from $1.2\,\mathrm{K}$ for bulk aluminium up to $9.3\,\mathrm{K}$ for niobium. They are all conventional superconductors and described by the BCS theory [29]. It can be noted that some materials with good conductance at room temperature like gold, silver and copper never undergo a superconducting transition. This is because good conductance at room temperature is often connected with a weak electron-phonon coupling, while superconductivity arises from this very interaction. Therefore good superconductors can be relatively bad conductors in their normal state.

While the property of zero resistance is very similar for a superconductor and a perfect conductor, there is another property that distinguish them. Superconductors expel any externally applied magnetic field, and thereby display near-perfect diamagnetism, unlike perfect conductors, see illustration in Fig. 2.1. This phenomenon is known as the Meissner effect [30]. However, if the applied field is stronger than the critical field of the superconductor, all Cooper pairs will be broken and the conductor transitions back to the normal state.

Figure 2.2: *A superconductor-insulator-superconductor (SIS) junction. The white line indicates the BCS wavefunction, and the fact that the wavefunctions Ψ_1 and Ψ_2 overlap indicate that Cooper pairs can tunnel.*

2.1.1 The Josephson effect

Two superconducting electrodes placed close to each other can allow electron tunnelling through the potential barrier in between. In 1962, Brian Josephson predicted the Cooper pair tunnelling between two superconducting electrodes [31]. Therefore, the effect is called the Josephson effect and the junction formed by the two electrodes is called a Josephson junction. These junctions are important nonlinear building blocks that are used in circuit QED [15]. There are different types of Josephson junctions but in this thesis the junctions consist of two superconducting electrodes, separated by a thin insulating layer, see Fig. 2.2. In these superconducting junctions the current depends on the phase difference of the wave functions on each side of the junction, $\theta = \theta_2 - \theta_1$, as

$$I = I_c \sin \theta. \tag{2.1}$$

This is known as the DC Josephson relation and I_c is the junction critical current, *i.e.* the maximum super current that the junction can support. The superconducting phase difference, θ, can be related to the voltage over the junction as

$$\frac{d\theta}{dt} = \frac{2e}{\hbar} V, \tag{2.2}$$

known as the AC Josephson relation.

From the Josephson equations, Eqs. (2.1) and (2.2), it can be seen that a Josephson junction behaves as a nonlinear inductor

$$V = L_J \frac{dI}{dt},$$

with the inductance

$$L_J = \frac{\hbar}{2eI_c \cos \theta}. \tag{2.3}$$

The junction also have an intrinsic capacitance. Approximating the junction as a parallel plate capacitance, it can be estimated

$$C_J = \frac{\epsilon_0 \epsilon_r A}{t}. \tag{2.4}$$

Here ϵ_0 is the permittivity of vacuum, ϵ_r the relative permittivity of the insulating layer between the electrodes, A the junction overlap area and t the thickness of the insulating
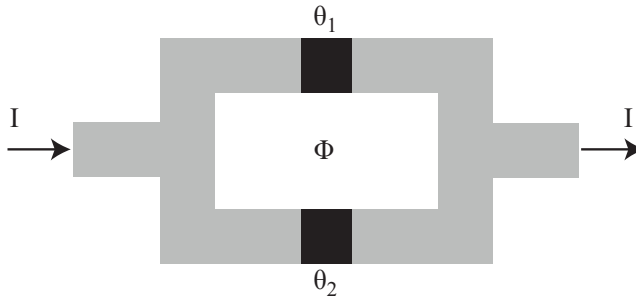
Figure 2.3: *Two Josephson junctions in parallel form a SQUID, a nonlinear device that is very sensitive to magnetic flux.*

layer. Energy can be stored in the junction as both inductive and capacitive energy. Depending on the frequency regime, the response is different. For frequencies well below the plasma frequency, $\omega_p = 1/\sqrt{L_J C_J}$, the response is mainly inductive. In this thesis, the junctions are operated mainly in the inductive regime and the inductive energy, the Josephson energy of a junction, is written

$$E_J = \frac{\hbar I_c}{2e}. \tag{2.5}$$

2.1.2 The SQUID

Two Josephson junctions connected in parallel in a superconducting loop is called a Superconducting Quantum Interference Device (SQUID). This device is very sensitive to magnetic flux [26]. From the London equations [32] we have the gradient of the superconducting phase θ. It depends on the supercurrent, $\vec{J}_s$ and an electromagnetic vector potential, $\vec{A}$ as

$$\nabla \theta = -\Lambda \vec{J}_s - \frac{2e}{\hbar} \vec{A},$$

with the London parameter $\Lambda = m_e/2ne^2$ and m_e is the electron mass. Integrating over a closed loop and choosing a path well inside the conductor gives $\vec{J}_s = 0$, since supercurrents are only flowing on the surfaces. The integral can be written

$$\oint \nabla \theta dl = -\oint \Lambda \vec{J}_s dl - \frac{2e}{\hbar} \oint \vec{A} dl$$

and rewritten

$$2\pi n - \theta_1 + \theta_2 = 0 - \frac{2e}{\hbar} \int \nabla \times \vec{A} dS = -\frac{2e}{\hbar} \int \vec{B} dA = -\frac{2e}{\hbar} \Phi,$$

where Φ denotes magnetic flux. Introducing the magnetic flux quantum, $\Phi_0 = \frac{h}{2e}$, this can be rewritten again as

$$\theta_1 - \theta_2 = 2\pi n + 2\pi \frac{\Phi}{\Phi_0}.$$

The total current flowing in the SQUID is

$$I = I_{c,1} \sin\theta_1 + I_{c,2} \sin\theta_2 = I_{c,1} \sin\left(\theta + \frac{\Phi}{\Phi_0}\pi + 2\pi n\right) + I_{c,2} \sin\left(\theta - \frac{\Phi}{\Phi_0}\pi + 2\pi n\right),$$

where $\theta = (\theta_1 + \theta_2)/2$. This can be rewritten

$$I = (I_{c,1} + I_{c,2})\left(\sin\theta\cos\frac{\Phi\pi}{\Phi_0} + \frac{I_{c,1} - I_{c,2}}{I_{c,1} + I_{c,2}}\cos\theta\sin\frac{\Phi\pi}{\Phi_0}\right).$$

If we denote the sum of the critical currents of the two junctions $I_{c,1} + I_{c,2} = I_c$, and the difference $I_{c,1} - I_{c,2} = \Delta I_c$ then

$$\frac{dI}{dt} = I_c\left(\cos\theta\cos\frac{\Phi\pi}{\Phi_0} - \frac{\Delta I_c}{I_c}\sin\theta\sin\frac{\Phi\pi}{\Phi_0}\right)\frac{d\theta}{dt}.$$

Using the AC Josephson relation, Eq. (2.2), a definition of the SQUID inductance is found

$$\frac{dI}{dt} = I_c\left(\cos\theta\cos\frac{\Phi\pi}{\Phi_0} - \frac{\Delta I_c}{I_c}\sin\theta\sin\frac{\Phi\pi}{\Phi_0}\right)\frac{2e}{\hbar}V \equiv \frac{1}{L_{SQ}}V.$$

Explicitly the SQUID inductance is written

$$L_{SQ} = \frac{L_{SQ,0}}{\cos\theta\cos\frac{\Phi\pi}{\Phi_0} - \frac{\Delta I_c}{I_c}\sin\theta\sin\frac{\Phi\pi}{\Phi_0}}, \tag{2.6}$$

where $L_{SQ,0} = \hbar/2eI_c$. Note how similar the SQUID inductance for a symmetric SQUID, $\Delta I_c = 0$, is the single junction inductance, Eq. (2.3). The difference is found in the flux dependence. The SQUID inductance, Eq. (2.6), can be rewritten in terms of the current I instead of the superconducting phase using the DC Josephson relation, Eq. (2.1), as

$$L_{SQ} = \frac{L_{SQ,0}}{\sqrt{\cos^2\frac{\Phi\pi}{\Phi_0} + \left(\frac{\Delta I_c}{I_c}\right)^2\sin^2\frac{\Phi\pi}{\Phi_0} - \left(\frac{I}{I_c}\right)^2}}, \tag{2.7}$$

which for low signal levels, $I \ll I_c$, is simplified

$$L_{SQ} = \frac{L_{SQ,0}}{\sqrt{\cos^2\frac{\Phi\pi}{\Phi_0} + \left(\frac{\Delta I_c}{I_c}\right)^2\sin^2\frac{\Phi\pi}{\Phi_0}}}. \tag{2.8}$$

For a symmetric SQUID, $I_{c,1} = I_{c,2}$, further simplifying the inductance

$$L_{SQ} = \frac{L_{SQ,0}}{\left|\cos\frac{\Phi\pi}{\Phi_0}\right|}. \tag{2.9}$$

For room temperature characterization of SQUIDs or junctions we have the expression

$$I_c = \frac{R_Q}{R_N}\frac{e\Delta_{BCS}}{\hbar},$$

which relates the normal state resistance of the SQUID (junction) to its critical current [33]. Here $R_Q = h/4e^2$ is the superconducting resistance quantum, $\Delta_{BCS} = 1.76k_B T_c$ the superconducting energy gap of aluminium, k_B is Boltzmann's constant, and T_c is the critical temperature, which for bulk aluminium is $1.2\,\text{K}$.
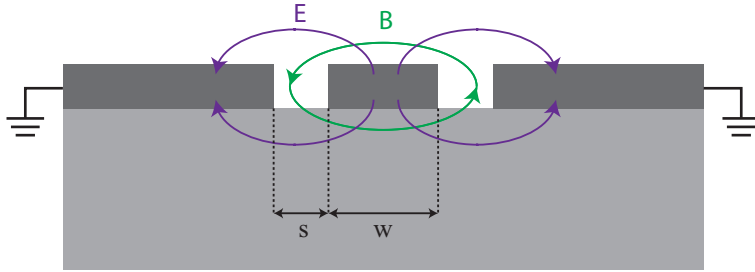
Figure 2.4: *A coplanar waveguide is a planar transmission line structure with a centre conductor capacitively coupled to the ground planes. The figure illustrates a cross-section of a coplanar waveguide transmission line on top of a substrate.*

2.2 Microwave transmission line resonators

The general picture of a resonator is two mirrors placed opposite of each other forming a cavity that confines light: an optical cavity, a confinement where light bounces back and forth and interfere with itself, called a Fabry-Perot cavity [34]. Instead of optical light and mirrors, we use superconducting circuits and impedance differences to confine microwave signals.

The circuits consist of microwave transmission lines and the size of the components is of the order of a wavelength. Therefore, transmission line theory is used instead of normal circuit theory. In transmission line theory, the voltage and current vary in magnitude and phase over distance. In this thesis the transmission lines are of the coplanar waveguide (CPW) type [35]. The CPW consists of a centre conductor, capacitively coupled to a ground plane via a gap, as shown in Fig. 2.4. Compared to other types of transmission lines, the CPW is convenient to fabricate in small scales at the surface of a chip. In superconducting coplanar waveguides, where the width of the centre conductor is much smaller than the wavelength of the transmitted wave, only a quasi-TEM wave can propagate [36].

The voltage and current signals propagating forward and backwards in a microwave transmission line are written

$$V(x) = V^+ e^{-\gamma x} + V^- e^{\gamma x} \tag{2.10a}$$

$$I(x) = I^+ e^{-\gamma x} + I^- e^{\gamma x} \tag{2.10b}$$

where $\gamma = \alpha + i\beta = \sqrt{(R + i\omega L)(G + i\omega C)}$ is the complex propagation constant and R, L, G and C are the resistance, inductance, conductance and capacitance of the transmission line. The losses are represented by the parameter α and hence for a lossless transmission line $\gamma = i\beta$. The impedance of the transmission line is given by $Z = \sqrt{(R + i\omega L)/(G + i\omega C)}$, which in a lossless line simplifies to $Z = \sqrt{L/C}$.

The properties of a coplanar waveguide transmission line are set by the materials of the circuit and substrate as well as geometry: the centre conductor width, w, and the size of the gap between the centre conductor and the ground plane, s, see illustration in Fig. 2.4. From these dimension and material choices, the geometric inductance and
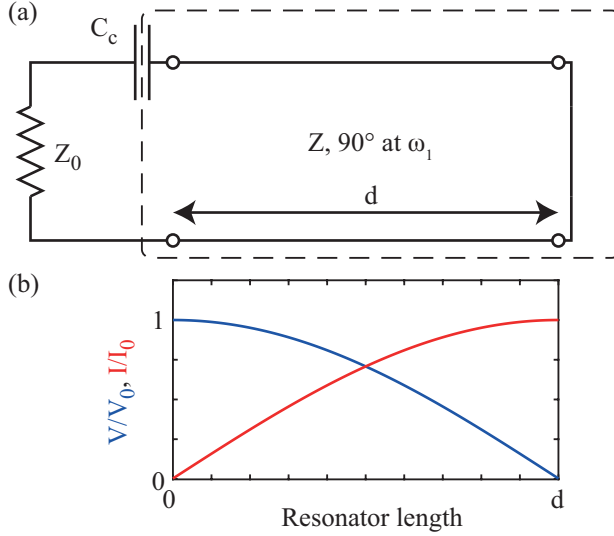
Figure 2.5: *(a) Schematic of a transmission line resonator with impedance Z, physical length d and electrical length $90°$. The resonator is connected via a coupling capacitor to an environment with the characteristic impedance Z_0. (b) The voltage and current distribution in the resonator.*

capacitance per unit length can be calculated [35–38]

$$L_0 = \frac{\mu_0}{4} \frac{K(k_0')}{K(k_0)} \tag{2.11a}$$

$$C_0 = 4\epsilon_0 \epsilon_{eff} \frac{K(k_0)}{K(k_0')}, \tag{2.11b}$$

where K denotes the complete elliptic integral of the first kind and $k_0 = w/(w+2s)$, and $k_0' = \sqrt{1-k_0^2}$. μ_0 and ϵ_0 are the vacuum permeability and permittivity respectively, and together they give the speed of light in vacuum $c = 1/\sqrt{\mu_0 \epsilon_0}$. In a coplanar waveguide transmission line, part of the signal is transmitted inside the substrate, therefore the permittivity is increased by a scaling factor, ϵ_{eff}. The scaling depend on substrate material and geometry. Hence, the speed of light in the coplanar waveguide transmission line is $v = 1/\sqrt{\mu_0 \epsilon_0 \epsilon_{eff}} = 1/\sqrt{L_0 C_0}$.

A microwave resonator consists of a finite length transmission line, see illustration in Fig. 2.5(a). The resonator is defined by its impedance Z, its length d, and the electrical length. The electrical length defines how many wavelengths that fit inside the resonator boundaries at a specific frequency. Here, one quarter of a period at ω_1 implies that the length of the resonator corresponds to a quarter of the first resonator mode wavelength, a quarter wavelength ($\lambda/4$) resonator. The voltage and current in the resonator are distributed as shown in Fig. 2.5(b). As seen, the voltage has an anti node at the coupling capacitor and a node at the grounded end. The current has a node at the capacitively coupled port and an anti node at the grounded end. The resonator is connected to an environment with impedance Z_0 via the coupling capacitor C_c.
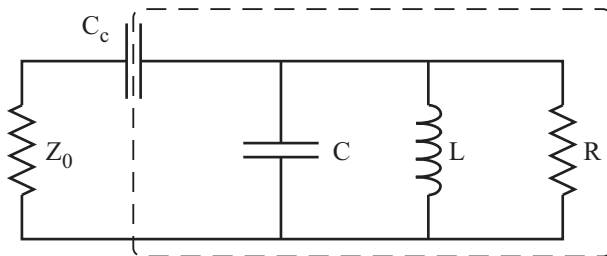
Figure 2.6: *Using a lumped element method, a transmission line resonator (Fig. 2.5(a)) can be modelled as a capacitance, inductance and resistance in parallel.*

The resonator stores energy as oscillator standing waves. For these standing waves only certain discrete energy values are allowed, *i.e.* the set of modes in the energy spectra is discrete [39].

Losses in a resonator can be described by its quality factor, which is defined

$$Q = \frac{\text{Stored energy}}{\text{Dissipated energy/radian}}.$$

The total Q-value accounts for both internal losses inside the resonator and external losses due to coupling the resonator to the outside world. The total Q-value can be divided into internal/external losses as

$$\frac{1}{Q_{tot}} = \frac{1}{Q_{ext}} + \frac{1}{Q_{int}}. \tag{2.12}$$

The Q-value relates to the line width of the resonance as

$$Q_{tot} = \frac{\omega_r}{2\Gamma}, \tag{2.13}$$

where ω_r is the resonance frequency and 2Γ is the total damping of the resonator, *i.e.* the line width of the resonance. The larger the Q-value, the smaller the line width.

Close to resonance the circuit can be modelled as a lumped element circuit. In Fig. 2.6 an equivalent circuit schematic is presented for a resonator capacitively coupled to a transmission line (Fig. 2.5(a)). The resistance represents the internal losses in the resonator. The capacitively coupled end of the resonator acts as a semi-transparent mirror and the grounded end is a perfectly reflecting mirror. The resonance frequency of the resonator is

$$\omega_r \approx \frac{1}{\sqrt{L_{tot}(C_{tot} + C_c)}}, \tag{2.14}$$

and the internal and external quality factors can be expressed as [39]

$$Q_{int} = \frac{\omega_r RC((\omega_r C_c Z_0)^2 + 1 + C_c/C)}{(\omega_r C_c Z_0)^2 + 1}, \tag{2.15a}$$

$$Q_{ext} = \frac{((\omega_r C_c Z_0)^2 + 1)C + C_c}{Z_0 C_c^2 \omega_r}. \tag{2.15b}$$
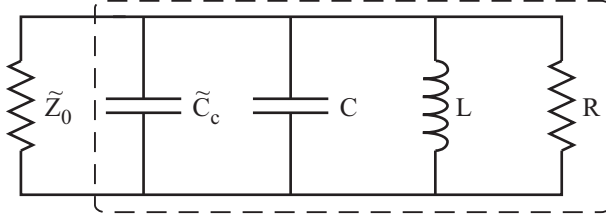
Figure 2.7: *The characteristic impedance and coupling capacitance from the circuit diagram in Fig. 2.6 have been replaced by equivalent parallel ones in order to simplify calculations.*

Using the assumption that the coupling is small $\omega_r C_c Z_0 \ll 1$, this can be rewritten

$$Q_{int} = \omega_r R(C + C_c), \tag{2.16a}$$

$$Q_{ext} = \frac{C + C_c}{\omega_r C_c^2 Z_0}. \tag{2.16b}$$

Comparing incoming and outgoing signals for the resonator an expression for the reflection coefficient can be given as follows [39]

$$S_{11} = \frac{Z_L - Z_0}{Z_L + Z_0}, \tag{2.17}$$

where Z_L is the load impedance of the resonator and Z_0 is the characteristic impedance of the environment. To simplify calculations the resonator lumped element model can be modified to the circuit diagram in Fig. 2.7. The coupling capacitance C_c and impedance Z_0 have been replaced by equivalent parallel elements $\tilde{Z}_0 = 1/\omega_r^2 Z_0 C_c^2$ and $\tilde{C}_c \approx C_c$. For this circuit, the external Q-value is written $Q_{ext} = \omega_r \tilde{Z}_0 (C + C_c)$. With parallel elements, the load admittance of the resonator circuit is

$$Y_L = \frac{1}{Z_L} = \frac{1}{R} + i\omega(C + C_c) + \frac{1}{i\omega L},$$

which can be rewritten as

$$Y_L = \frac{1}{R} + i\omega(C + C_c)\left(1 - \frac{1}{\omega^2 L(C + C_c)}\right).$$

Inserting (2.14) gives

$$Y_L = \frac{1}{R} + i\omega(C + C_c)\left(1 - \frac{\omega_r^2}{\omega^2}\right),$$

where the last part can be simplified further

$$\left(1 - \frac{\omega_r^2}{\omega^2}\right) = \frac{\omega^2 - \omega_r^2}{\omega^2} = \frac{\overbrace{(\omega - \omega_r)}^{=\Delta\omega}(\omega + \omega_r)}{\omega^2} = \frac{\Delta\omega}{\omega}\left(1 + \frac{\omega_r}{\omega}\right) = \frac{\Delta\omega}{\omega}\left(1 + \frac{1}{1 + \frac{\Delta\omega}{\omega_r}}\right) \approx 2\frac{\Delta\omega}{\omega},$$

15

assuming $\Delta\omega \ll \omega_r$. Hence

$$Y_L = \frac{1}{R} + 2i\underbrace{(C + C_c)}_{=\frac{Q_{int}}{\omega_r R}}\Delta\omega = \frac{1}{R} + i\frac{2\Delta\omega Q_{int}}{\omega_r R},$$

using (2.16a). To simplify further calculations it is noticed that (2.17) can be rewritten

$$S_{11} = \frac{\tilde{Y}_0 - Y_L}{\tilde{Y}_0 + Y_L},$$

where $\tilde{Y}_0 = 1/\tilde{Z}_0$. When inserting the expression for the load admittance the resulting expression is

$$S_{11} = \frac{\frac{1}{\tilde{Z}_0} - \frac{1}{R} - i\frac{2\Delta\omega Q_{int}}{\omega_r R}}{\frac{1}{\tilde{Z}_0} + \frac{1}{R} + i\frac{2\Delta\omega Q_{int}}{\omega_r R}} = \frac{\frac{R}{\tilde{Z}_0} - 1 - i2Q_{int}\frac{\Delta\omega}{\omega_r}}{\frac{R}{\tilde{Z}_0} + 1 + i2Q_{int}\frac{\Delta\omega}{\omega_r}}$$

and using $\frac{R}{\tilde{Z}_0} = \frac{Q_{int}}{Q_{ext}}$, the result is

$$S_{11} = \frac{\frac{1}{Q_{ext}} - \frac{1}{Q_{int}} - 2i\frac{\Delta\omega}{\omega_r}}{\frac{1}{Q_{ext}} + \frac{1}{Q_{int}} + 2i\frac{\Delta\omega}{\omega_r}}. \tag{2.18}$$

This can also be written in terms of total and external Q-values as

$$S_{11} = \frac{2Q_{tot}/Q_{ext}}{1 + 2iQ_{tot}(\omega/\omega_r - 1)}e^{i\varphi_{ext}} - 1. \tag{2.19}$$

Here an extra phase factor is added to the external Q-value, φ_{ext}, that accounts for impedance mismatches between the resonator and environment. In addition, the full environment that the resonator is connected to can be taken into account by adding some extra background scaling

$$S_{11} = S_{11}^{back.} \cdot S_{11}^{ideal} = ke^{i(\varphi_{off} + (\omega - \omega_r)\tau_{delay})}\left[\frac{2Q_{tot}/Q_{ext}}{1 + 2iQ_{tot}(\omega/\omega_r - 1)}e^{i\varphi_{ext}} - 1\right], \tag{2.20}$$

where k is a scaling parameter to adjust the background level, φ_{off} is a phase offset, and τ_{delay} is the electrical delay.

Depending on how the internal and external losses in the resonator compare to each other, the resonator can be in different regimes, see Fig. 2.8. When $Q_{ext} > Q_{int}$ the resonator is undercoupled (green), implying that more energy is lost inside the resonator than in the coupling to other circuitry. If $Q_{ext} < Q_{int}$, more energy is lost through the coupling than inside and the resonator is said to be overcoupled (blue) instead. At the critical point were $Q_{int} = Q_{ext}$, the resonator is critically coupled (red). Depending on applications, different regimes are preferable. However, to maximize the intensity of a general output signal, an overcoupled resonator is preferable.

Internal losses of a superconducting resonator can have many reasons. For a detailed description of these loss mechanisms I recommend the theses of de Graaf and Burnett [40, 41]. The internal quality factor can be divided into contributions from each source of loss

$$\frac{1}{Q_{int}} = \frac{1}{Q_{rad}} + \frac{1}{Q_{TLF}} + \frac{1}{Q_{\mu W}} + \frac{1}{Q_B} + \frac{1}{Q_{QP}} + ...$$
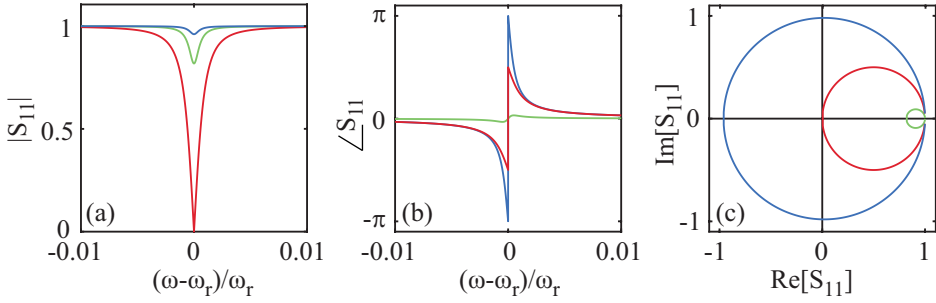
Figure 2.8: *Illustration of an* undercoupled, overcoupled *and* critically coupled *resonator. (a) Magnitude of the reflected signal. Note that the response of the overcoupled and the undercoupled resonators are very similar. (b) Phase of the reflected signal. (c) Polar plot of the real and imaginary part of the reflected signal. Here the undercoupled resonator forms just a small dot at the point $S_{11} = 1$.*

Here Q_{rad} represents radiation losses which are usually very small. Q_{TLF} represents dielectric losses. These are mainly due to interaction with two-level fluctuators that are situated in the substrate-superconductor interfaces [42, 43]. This is usually the main loss mechanism when operating the resonator at low temperature and low signal levels. It has been shown that an increase in temperature can lead to reduced losses due to saturation of two-level fluctuators [44]. Furthermore, the two-level fluctuators can also be saturated by increased signal levels [45]. Other possible loss mechanisms can for instance be mistakes in the microwave engineering that makes the system lossy, $Q_{\mu W}$, losses induced by an applied magnetic field Q_B, or quasi particle losses Q_{QP}.

2.3 The tunable resonator

The superconducting resonator (Fig. 2.9(a)) is made tunable by adding a SQUID (Fig. 2.9(b)), which acts as a tunable inductance. This means that by controlling the magnetic flux in the SQUID loop, the total inductance of the resonator can be controlled *in situ*. Effectively, this means that the electric length of the resonator can be tuned, and consequently also its resonance frequency. In Fig. 2.9(c) the voltage profile of the first resonator mode is plotted for the static resonator in (a) and the tunable resonator in (b). As seen the SQUID inductance changes the boundary condition of the electromagnetic field in the tunable resonator (red) compared to the static resonator (blue). This tuning is a tuning of the resonator field boundary condition. This can be seen as an analogy of mechanically moving one of the mirrors confining the light in an optical cavity.

2.3.1 The resonator spectrum

In a resonator, energy can only be stored at certain energies. These energy levels form a spectrum of modes. The spacing between the modes depend on the boundary conditions of the resonator and can be different for different types of resonators. The resonator in
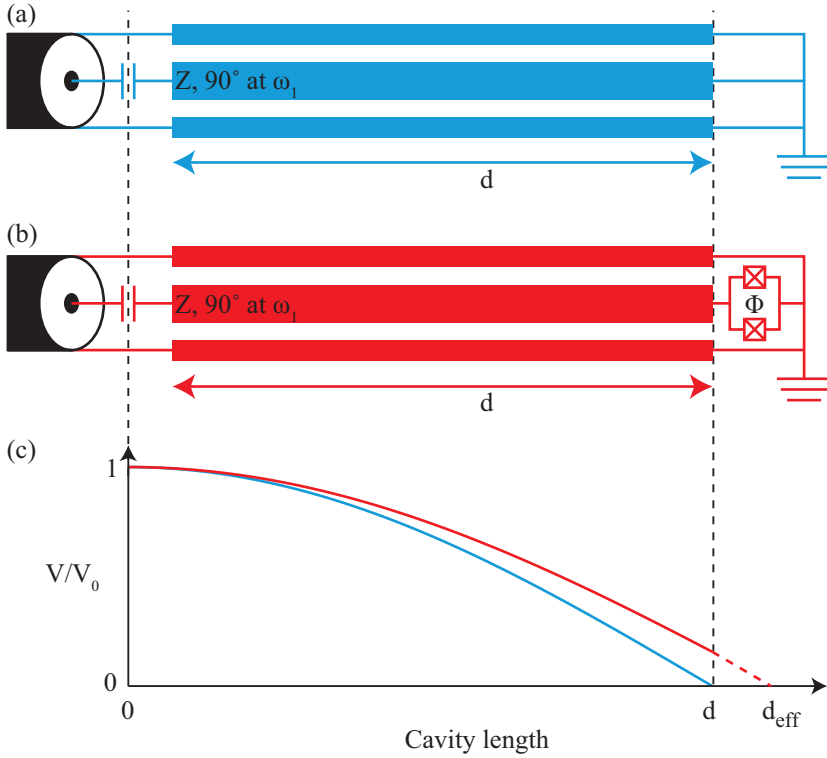
Figure 2.9: *(a) Schematic of a circuit for a coplanar waveguide microwave resonator, similar to Fig. 2.5(a). (b) Resonator with a SQUID attached in the grounded end, a tunable resonator. (c) Voltage profile for the resonators in (a) and (b). Due to the extra inductance of the SQUID, the effective length of the tunable resonator is longer than that of the static resonator.*
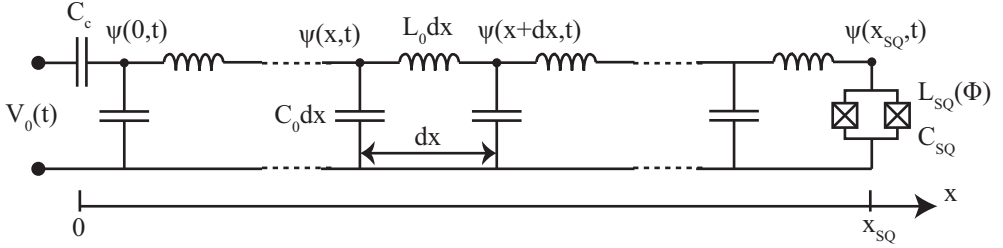
Figure 2.10: *Model of the resonator in Fig. 2.9(b) using a distributed network of small elements.*

Fig. 2.9(a) has modes with equidistant spacing while the SQUID-terminated resonator in (b) has a different boundary condition, and therefore a different spectrum. Due to the nonlinearity of the SQUID, the resonator spectrum becomes non-equidistant. The higher the mode number, the smaller (or larger, depending on the exact resonator parameters) the separation between modes.

The resonator in Fig. 2.9(b) can be modelled by a distributed network of small capacitive and inductive elements, see Fig. 2.10. The field inside the resonator is characterised by the generalized flux $\psi(x,t) = \int_{-\inf}^{t} V(x,t)dx$, which can be evaluated for each node in the distributed network. To model the dynamics of the resonator field, the Lagrangian formalism [46, 47] can be used. The Lagrangian expression represents the difference between capacitive and inductive energy in the circuit. Each element can be treated individually and the different contributions are summed up to the Largangian of the full circuit.

The Lagrangian for the different parts of the circuit are written as the following, for a coupling capacitor at position $x = 0$

$$\mathcal{L}_{C_c} = \frac{C_c}{2} \left(\dot{\psi}(0,t) - V_0(t) \right)^2,$$ (2.21)

for the SQUID

$$
\begin{aligned}
\mathcal{L}_{SQ} =& \frac{C_{SQ}}{2} \dot{\psi}^2(x_{SQ},t) + \frac{1}{L_{SQ}(\Phi)} \left(\frac{\Phi_0}{2\pi} \right)^2 \cos \left(\frac{2\pi\psi(x_{SQ},t)}{\Phi_0} \right) \\
=& \frac{C_{SQ}}{2} \dot{\psi}^2(x_{SQ},t) + \frac{1}{L_{SQ}(\Phi)} \left(\frac{\Phi_0}{2\pi} \right)^2 \left[1 - \left(\frac{2\pi}{\Phi_0} \right)^2 \frac{\psi^2(x_{SQ},t)}{2} + ... \right] \\
=& \frac{C_{SQ}}{2} \dot{\psi}^2(x_{SQ},t) - \frac{\psi^2(x_{SQ},t)}{2L_{SQ}(\Phi)},
\end{aligned}
$$ (2.22)

and for the coplanar waveguide transmission line

$$\mathcal{L}_{res} = \int_0^{x_{SQ}} \left(\frac{C_0}{2} \dot{\psi}^2(x,t) - \frac{[\partial_x \psi(x,t)]^2}{2L_0} \right) dx.$$ (2.23)

Then the total Lagrangian is a sum of the different contributions. We extract a small action $\delta\mathcal{S} = \int dt \delta\mathcal{L}$ which should be equal to zero. This requirement leads to the boundary

19

conditions of the resonator energy spectrum. Different resonator designs result in different boundary conditions. The following subsections will present the resonator types used in this thesis.

The quarter-wavelength resonator

Here I will derive the dispersion relation for the resonator in Fig. 2.9(b). At one end, the resonator is capacitively coupled to the transmission line. While the other end of the resonator is grounded via a SQUID. The boundary conditions for the resonator field at the capacitively coupled end, where $x = 0$, is $\psi'_0 = 0$. In the SQUID terminated end, $x = d$, the boundary condition is less trivial. To understand this we consider a small action

$$\delta \mathcal{S} = \int dt \left[\delta \mathcal{L}_{C_c} + \delta \mathcal{L}_{res} + \delta \mathcal{L}_{SQ} \right] = 0.$$

Since the coupling is static it can be assumed $\delta \mathcal{L}_{C_c} = 0$. The resonator contribution is written

$$\delta \mathcal{S}_{res} = \int dt \int_0^d dx \left[C_0 \dot{\psi} \delta \dot{\psi} - \frac{1}{L_0} \psi' \delta \psi' \right],$$

where the inductive part is integrated by part as

$$-\int_0^d dx \frac{1}{L_0} \psi' \delta \psi' = \frac{1}{L_0} \int_0^d \psi'' \delta \psi dx - \frac{1}{L_0} \left[\psi' \delta \psi \right]_0^d$$

$$= \frac{1}{L_0} \int_0^d \psi'' \delta \psi dx - \frac{1}{L_0} \left(\psi'_d \delta \psi_d - \psi'_0 \delta \psi_0 \right).$$

The last term is zero, since the field is static at the capacitively coupled edge, $\delta \psi_0 = 0$. The capacitive part is written

$$\int_0^d dx \int dt C_0 \dot{\psi} \delta \dot{\psi} = \int_0^d dx C_0 \left[-\int dt \ddot{\psi} \delta \psi + \left[\psi \delta \dot{\psi} \right]_0^{t_0} \right],$$

where $\left[\psi \delta \dot{\psi} \right]_0^{t_0} = 0$, under the assumption that the state of the system is fixed ($\delta \psi = 0$) at the beginning and the end of time. Then the full resonator contribution to the dynamics is

$$\delta \mathcal{S}_{res} = -\int dt \left[C_0 \int_0^d \left(\ddot{\psi} \delta \psi - \frac{1}{v^2} \psi'' \delta \psi \right) dx + \frac{1}{L_0} \psi'_d \delta \psi_d \right] = -\int dt \frac{1}{L_0} \psi'_d \delta \psi_d, \quad (2.24)$$

where the wave equation $\ddot{\psi} - \frac{1}{v^2} \psi'' = 0$ is used, remember that the phase velocity $v = 1/\sqrt{L_0 C_0}$. The SQUID contribution is written

$$\delta \mathcal{S}_{SQ} = \int dt \left[C_{SQ} \dot{\psi}_d \delta \dot{\psi}_d - \frac{1}{|L_{SQ}(\Phi)|} \psi_d \delta \psi_d \right] \quad (2.25)$$

and using the same technique as for the resonator part this results in

$$\delta \mathcal{S}_{SQ} = -\int dt \left[C_{SQ} \ddot{\psi}_d \delta \psi_d + \frac{1}{|L_{SQ}(\Phi)|} \psi_d \delta \psi_d \right]. \quad (2.26)$$

To sum up

$$\delta \mathcal{S} = \delta \mathcal{S}_{res} + \delta \mathcal{S}_{SQ} = -\int dt \left[\frac{1}{L_0} \psi'_d \delta\psi_d + C_{SQ}\ddot{\psi}_d \delta\psi_d + \frac{1}{|L_{SQ}(\Phi)|}\psi_d \delta\psi_d \right] = 0,$$

which results in the boundary condition for the SQUID terminated end of the resonator

$$C_{SQ}\ddot{\psi}_d + \frac{|\cos(\Phi_{ext}\pi/\Phi_0)|}{L_{SQ,0}}\psi_d + \frac{1}{L_0}\psi'_d = 0 \qquad (2.27)$$

For static biasing, $\Phi_{ext} = \Phi_{dc}$. The field is assumed to be on the form $\psi_n \propto e^{\pm i\omega_n t}\cos k_n x$, where $k_n = \omega_n/v$ is the wave number. Inserted in the boundary condition, Eq. (2.27), the resulting equation is

$$-C_{SQ}\omega_n^2 e^{\pm i\omega_n t}\cos k_n d + \frac{|\cos(\Phi_{ext}\pi/\Phi_0)|}{L_{SQ,0}}e^{\pm i\omega_n t}\cos k_n d - \frac{k_n}{L_0}e^{\pm i\omega_n t}\sin k_n d = 0,$$

which can be rewritten

$$k_n d\tan k_n d = \frac{|\cos(\Phi_{dc}\pi/\Phi_0)|}{\gamma_0} - c(k_n d)^2. \qquad (2.28)$$

Here the inductive participation ratio, $\gamma_0 = L_{SQ,0}/(L_0 d)$, is the ratio between the SQUID inductance and the resonator inductance and the capacitive participation ratio $c = \frac{C_{SQ}}{C_0 d}$ is the ratio between the SQUID capacitance and the resonator capacitance. This dispersion relation is derived in several different earlier works, see for example Ref. [22, 24, 47, 48].

The dispersion relation is a transcendental function, meaning that it can not be solved analytically. Instead, it has to be solved numerically. This has been done as a function of flux for the four lowest modes of a $\lambda/4$-resonator, as shown in Fig. 2.11. The frequency on the vertical axis is normalised to the zero flux frequency of the first resonator mode. Multiples of $\omega_1(0)$ are indicated by dashed black lines. We find that the spectrum is slightly non-equidistant, with the zero flux frequencies of higher modes being slightly below the odd multiples of the fundamental mode frequency. This is a result of the nonlinearity induced by the SQUID. We can also note that the first mode frequency is tuned all the way to zero when approaching half a flux quantum, while the higher modes reach a finite minimum value. In addition, we find that the higher modes have a smaller frequency spacing between maxima and minima. This can be understood if we look at the dispersion relation, the larger the mode number, n, the larger the capacitive term on the right hand side in Eq. 2.28 is, and therefore the smaller the influence of the inductive term that depends on flux.

The doubly tunable resonator

Next we study the doubly tunable resonator, which is grounded at each end via a SQUID, see Fig. 2.12. In the middle, there is a capacitively coupled probe. The coordinate system is defined so that the capacitive coupling is placed at $x = 0$ and the SQUIDs at $x = \pm d/2$.
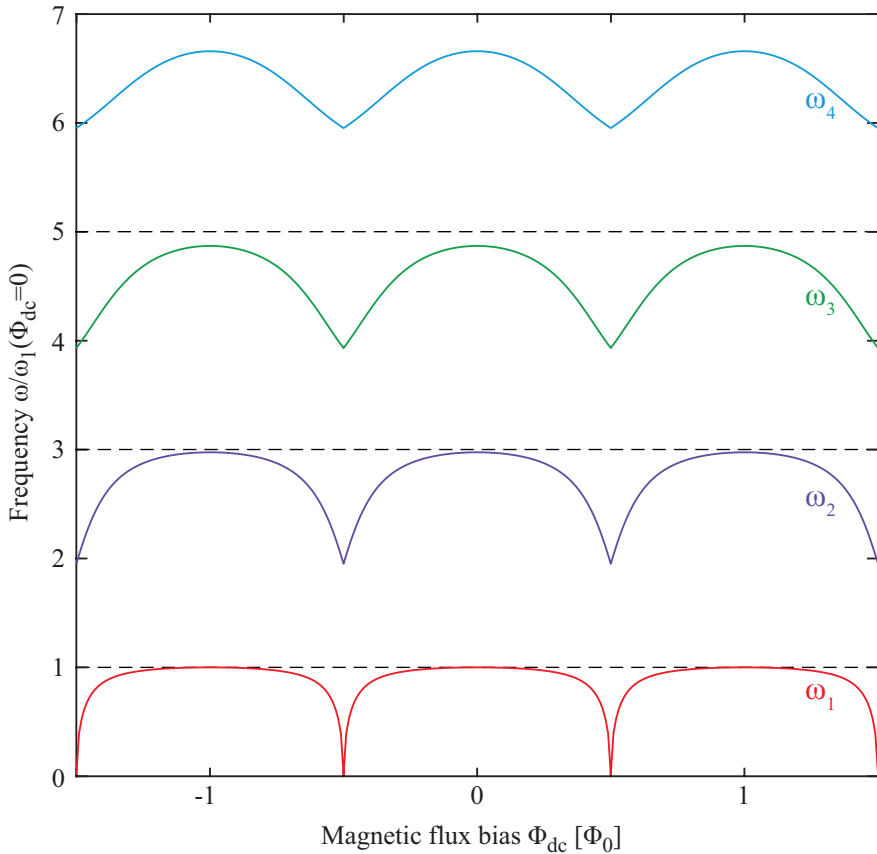
Figure 2.11: *The four lowest modes of a $\lambda/4$-resonator. Note how the first mode frequency goes to zero at half flux quantas while the higher modes reach a finite value. For this specific calculation the following parameters have been used, $d = 5.08\,mm$, $I_c = 1.9\,\mu A$, $\gamma_0 = 7.7\%$, $C_{SQ} = 86\,fF$, $c = 11\%$ and $v = 1.2 \cdot 10^8\,m/s$.*
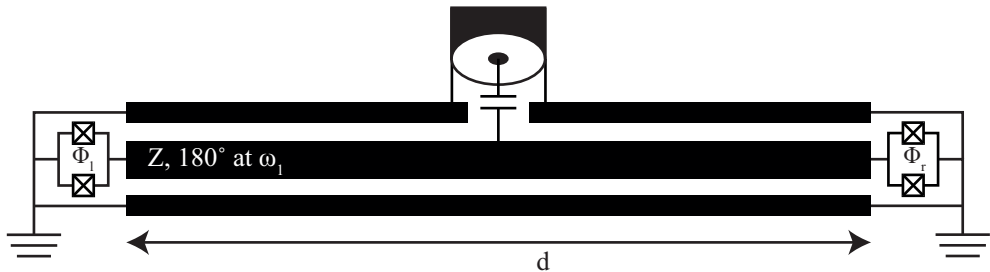
Figure 2.12: *Schematic of the doubly tunable resonator used in Paper C. Here the resonator has two SQUIDs, one at each end, i.e. two tunable boundary conditions.*

Again the coupling is static and can be neglected. The boundary condition for a SQUID terminated resonator end can be found using Eq. (2.27). Then the boundary conditions for the doubly tunable resonator can be written

$$C_{SQ,l}\ddot{\psi}_{-d/2} + \frac{|\cos\left(\Phi_{dc,l}\pi/\Phi_0\right)|}{L_{SQ,0,l}}\psi_{-d/2} - \frac{1}{L_0}\psi'_{-d/2} = 0 \tag{2.29a}$$

$$C_{SQ,r}\ddot{\psi}_{d/2} + \frac{|\cos\left(\Phi_{dc,r}\pi/\Phi_0\right)|}{L_{SQ,0,r}}\psi_{d/2} + \frac{1}{L_0}\psi'_{d/2} = 0, \tag{2.29b}$$

where the subscripts l/r denote the left and right SQUID. Here it is assumed that the SQUIDs are placed at $x = -d/2$ and $x = d/2$ respectively. We use an ansatz for the resonator field on the form $\psi_n \propto e^{\pm i\omega_n t}\cos(k_n x + \beta_n)$. Inserting this in the boundary conditions, Eq. (2.29) give

$$\left(-\omega_n^2 C_{SQ,l} + \frac{|\cos\left(\Phi_{dc,l}\pi/\Phi_0\right)|}{L_{SQ,0,l}}\right)\cos\left(-\frac{k_n d}{2} + \beta_n\right) + \frac{k_n}{L_0}\sin\left(-\frac{k_n d}{2} + \beta_n\right) = 0 \tag{2.30a}$$

$$\left(-\omega_n^2 C_{SQ,r} + \frac{|\cos\left(\Phi_{dc,r}\pi/\Phi_0\right)|}{L_{SQ,0,r}}\right)\cos\left(\frac{k_n d}{2} + \beta_n\right) - \frac{k_n}{L_0}\sin\left(\frac{k_n d}{2} + \beta_n\right) = 0. \tag{2.30b}$$

which can be rewritten

$$\left[\left(\gamma_l^{-1} - c_l(k_n d)^2\right)\cos(k_n d/2) - k_n d\sin(k_n d/2)\right]\cos\beta_n +$$
$$\left[\left(\gamma_l^{-1} - c_l(k_n d)^2\right)\sin(k_n d/2) + k_n d\cos(k_n d/2)\right]\sin\beta_n = 0, \tag{2.31a}$$
$$\left[\left(\gamma_r^{-1} - c_r(k_n d)^2\right)\cos(k_n d/2) - k_n d\sin(k_n d/2)\right]\cos\beta_n -$$
$$\left[\left(\gamma_r^{-1} - c_r(k_n d)^2\right)\sin(k_n d/2) + k_n d\cos(k_n d/2)\right]\sin\beta_n = 0. \tag{2.31b}$$

Here the inductive and the capacitive participation ratios are $\gamma_i = L_{SQ,0,i}/L_0 d|\cos\Phi_{dc,i}\pi/\Phi_0|$ and $c_i = C_{SQ,i}/C_0 d$, where $i \in \{l, r\}$. From both equations, expressions for $\tan\beta_n$ can be extracted

$$\tan\beta_n = \frac{\left(\gamma_l^{-1} - c_l(k_n d)^2\right)\cos(k_n d/2) - k_n d\sin(k_n d/2)}{\left(\gamma_l^{-1} - c_l(k_n d)^2\right)\sin(k_n d/2) + k_n d\cos(k_n d/2)} \tag{2.32a}$$

$$\tan\beta_n = -\frac{\left(\gamma_r^{-1} - c_r(k_n d)^2\right)\cos(k_n d/2) - k_n d\sin(k_n d/2)}{\left(\gamma_r^{-1} - c_r(k_n d)^2\right)\sin(k_n d/2) + k_n d\cos(k_n d/2)}. \tag{2.32b}$$

The dispersion relation is found by eliminating $\tan\beta_n$ from Eq. (2.32). Then we get

$$k_n d\tan\left(k_n d\right)\left[1 - \frac{1}{(k_n d)^2}\left(\frac{1}{\gamma_r} - c_r\left(k_n d\right)^2\right)\left(\frac{1}{\gamma_l} - c_l\left(k_n d\right)^2\right)\right]$$
$$= \frac{1}{\gamma_l} - c_l\left(k_n d\right)^2 + \frac{1}{\gamma_r} - c_r\left(k_n d\right)^2. \tag{2.33}$$
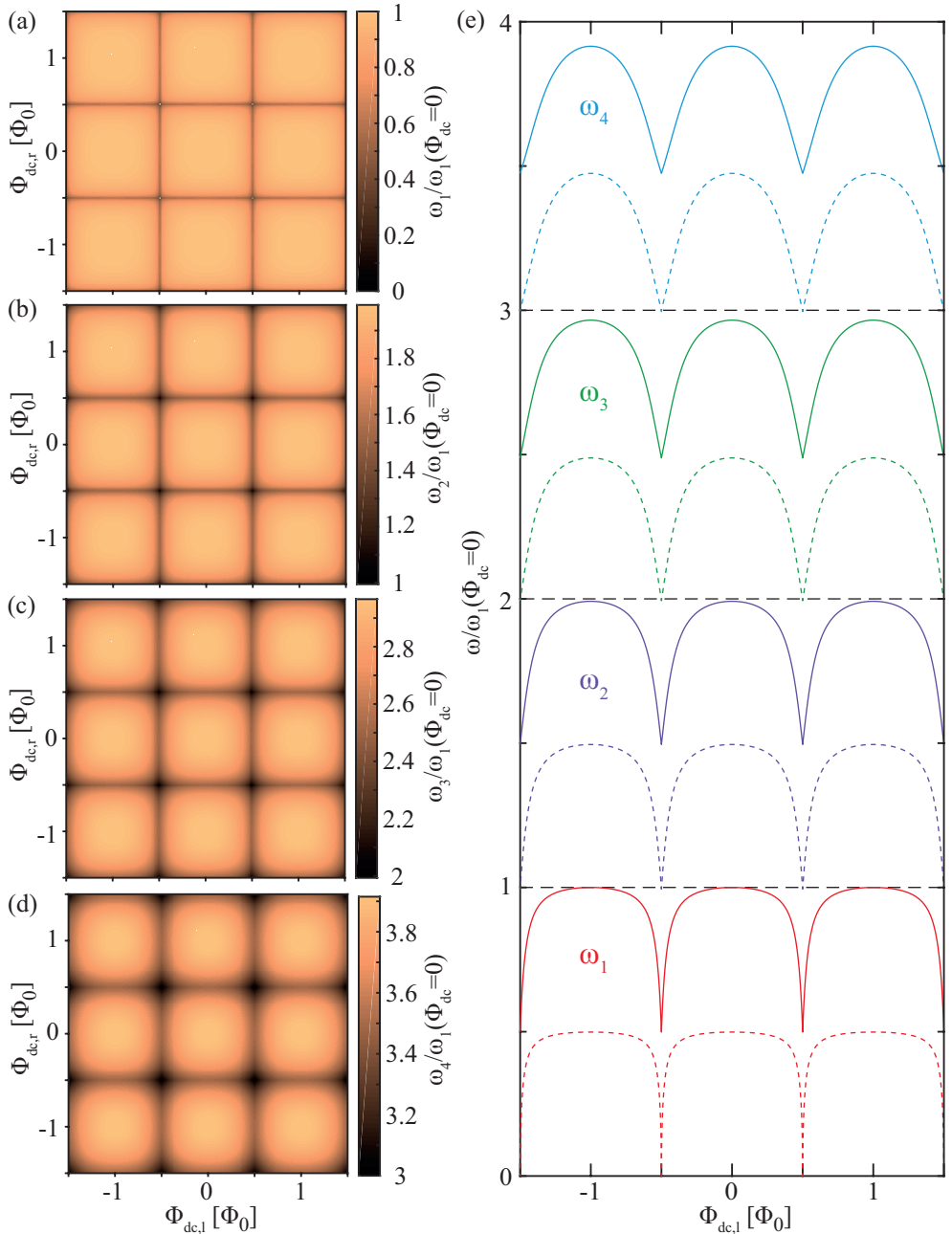
Figure 2.13: *(a-d) The four lowest modes of the doubly tunable resonator. On the horizontal axis, the magnetic flux bias in the left SQUID and on the vertical axis, the magnetic flux bias in the right SQUID. In colour scale you find the resonance frequency of respective mode scaled by the zero flux frequency of the first mode. (e) Linecuts of the graphs in (a-d), solid lines represent $\Phi_{dc,r} = 0$ and dashed lines $\Phi_{dc,r} = 0.5\,\Phi_0$. For this simulation the following parameters have been used: $d = 10.16\,mm$, $I_c = 1.47\,\mu A$, $\gamma_0 = 5\%$, $C_{SQ} = 86\,fF$, $c = 5.5\%$ and $v = 1.2 \cdot 10^8\,m/s$.*
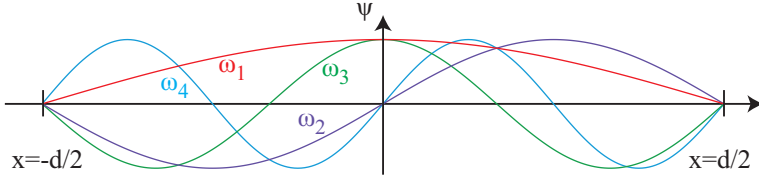
Figure 2.14: *Schematic figure of the four lowest resonator modes. Mode one and three are so called even modes and two and four are odd modes.*

With numbers of a typical resonator measured during this thesis, Fig. 2.13 illustrates the four lowest modes given by the dispersion relation. The frequency is scaled by the zero flux frequency of the lowest mode. Panel (a) to (d) shows the dc-tuning of the resonance frequency for the individual modes using the two different SQUIDs. In panel (e) line cuts are extracted from the other graphs, the solid lines represent $\Phi_{dc,r} = 0$ and dashed lines $\Phi_{dc,r} = 0.5\,\Phi_0$. Here, it is found that there is a mode close to every integer multiple of the lowest resonator mode. This is in contrast to the $\lambda/4$-resonator where the modes only appear close to odd multiples of the lowest mode frequency (Fig. 2.11).

For a symmetric resonator, $\gamma_l = \gamma_r = \gamma$ and $c_l = c_r = c$, the coefficients in the expressions (2.31) are the same

$$
\begin{aligned}
\left[\left(\gamma^{-1} - c(k_n d)^2\right)\cos(k_n d/2) - k_n d\sin(k_n d/2)\right]\cos\beta_n \pm \\
\left[\left(\gamma^{-1} - c(k_n d)^2\right)\sin(k_n d/2) + k_n d\cos(k_n d/2)\right]\sin\beta_n = 0.
\end{aligned}
\tag{2.34}
$$

This forms two subsets of modes, even modes

$$
\begin{aligned}
\left(\gamma^{-1} - c(k_n d)^2\right)\cos(k_n d/2) - k_n d\sin(k_n d/2) = 0 \\
\sin\beta_n = 0,\ \beta_n = \pm j\pi,\ j = 0, 1, 2, \ldots
\end{aligned}
\tag{2.35}
$$

where the phase field, $\psi_n(x,t) \propto e^{-i\omega_n t}(-1)^j \cos(k_n x)$, is symmetric with respect to the centre of the resonator, and odd modes

$$
\begin{aligned}
\left(\gamma^{-1} - c(k_n d)^2\right)\sin(k_n d/2) + k_n d\cos(k_n d/2) = 0 \\
\cos\beta_n = 0,\ \beta_n = \pm(2j+1)\pi/2,\ j = 0, 1, 2, \ldots
\end{aligned}
\tag{2.36}
$$

where the phase field, $\psi_n(x,t) \propto e^{-i\omega_n t}(-1)^{j+1}\sin(k_n x)$, is antisymmetric with respect to the resonator centre. For an illustration of symmetric and antisymmetric modes, see Fig. 2.14, where the phase field for the different modes is plotted for $j = 0$. It can be noted that the phase field and thereby the voltage has maximas in the middle for even modes and is zero for odd modes. This means that the coupling between the resonator and the external transmission line is strong for even modes but zero for odd modes.

The coupling resonator

In order to create the tunable coupling in Paper E and F, we use a tunable $\lambda/2-$resonator. Both ends of the resonator have semi-transparent mirrors, and in the middle a SQUID,
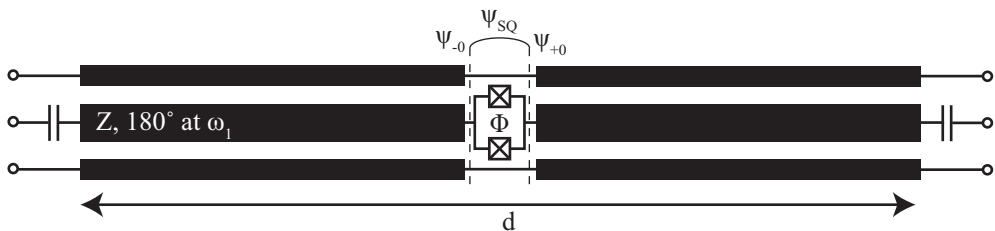
Figure 2.15: *Schematic of the coupling resonator used in Paper E and F.*

see schematic Fig. 2.15. We assume the SQUID to be placed at position $x = 0$, and the length of the resonator to be d, *i.e.* the coupling capacitors are placed at positions $x = \pm d/2$. Then the system can be divided into two parts, left and right resonator and two Lagrangians can be set up as

$$\mathcal{L}_{left} = C_0 \int_{-d/2}^{-0} dx (\dot{\psi}^2 - v^2 \psi'^2) + \frac{C_{SQ}}{2} \dot{\psi}_{SQ}^2 + \frac{\psi_{SQ}^2}{2 L_{SQ}(\Phi)} \tag{2.37a}$$

$$\mathcal{L}_{right} = C_0 \int_{+0}^{d/2} dx (\dot{\psi}^2 - v^2 \psi'^2) - \frac{C_{SQ}}{2} \dot{\psi}_{SQ}^2 - \frac{\psi_{SQ}^2}{2 L_{SQ}(\Phi)} \tag{2.37b}$$

following definitions of Eqs. (2.23) and (2.22). Here the superconducting phase over the SQUID is $\psi_{SQ} = \psi(-0) - \psi(+0)$. Following the techniques used before, the resulting boundary conditions are

$$\frac{1}{L_0} \psi'_{-0} + C_{SQ} \left(\ddot{\psi}_{-0} - \ddot{\psi}_{+0} \right) + \frac{\psi_{-0} - \psi_{+0}}{L_{SQ}(\Phi)} = 0 \tag{2.38a}$$

$$-\frac{1}{L_0} \psi'_{+0} + C_{SQ} \left(\ddot{\psi}_{+0} - \ddot{\psi}_{-0} \right) + \frac{\psi_{+0} - \psi_{-0}}{L_{SQ}(\Phi)} = 0. \tag{2.38b}$$

We assume the field is on the form

$$\psi(x < 0) = a_- \cos \left[k_n(x + d/2) \right] e^{-i\omega_n t}, \ \psi(x > 0) = a_+ \cos \left[k_n(x - d/2) \right] e^{-i\omega_n t}.$$

Inserting the ansatz in Eq. (2.38) gives

$$a_- \left(-\frac{k_n}{L_0} \sin \frac{k_n d}{2} - \omega_n^2 C_{SQ} \cos \frac{k_n d}{2} + \frac{1}{L_{SQ}(\Phi)} \cos \frac{k_n d}{2} \right) +$$
$$a_+ \left(\omega_n^2 C_{SQ} \cos \frac{k_n d}{2} - \frac{1}{L_{SQ}(\Phi)} \cos \frac{k_n d}{2} \right) = 0 \tag{2.39a}$$

$$a_- \left(\omega_n^2 C_{SQ} \cos \frac{k_n d}{2} - \frac{1}{L_{SQ}(\Phi)} \cos \frac{k_n d}{2} \right) +$$
$$a_+ \left(-\frac{k_n}{L_0} \sin \frac{k_n d}{2} - \omega_n^2 C_{SQ} \cos \frac{k_n d}{2} + \frac{1}{L_{SQ}(\Phi)} \cos \frac{k_n d}{2} \right) = 0. \tag{2.39b}$$
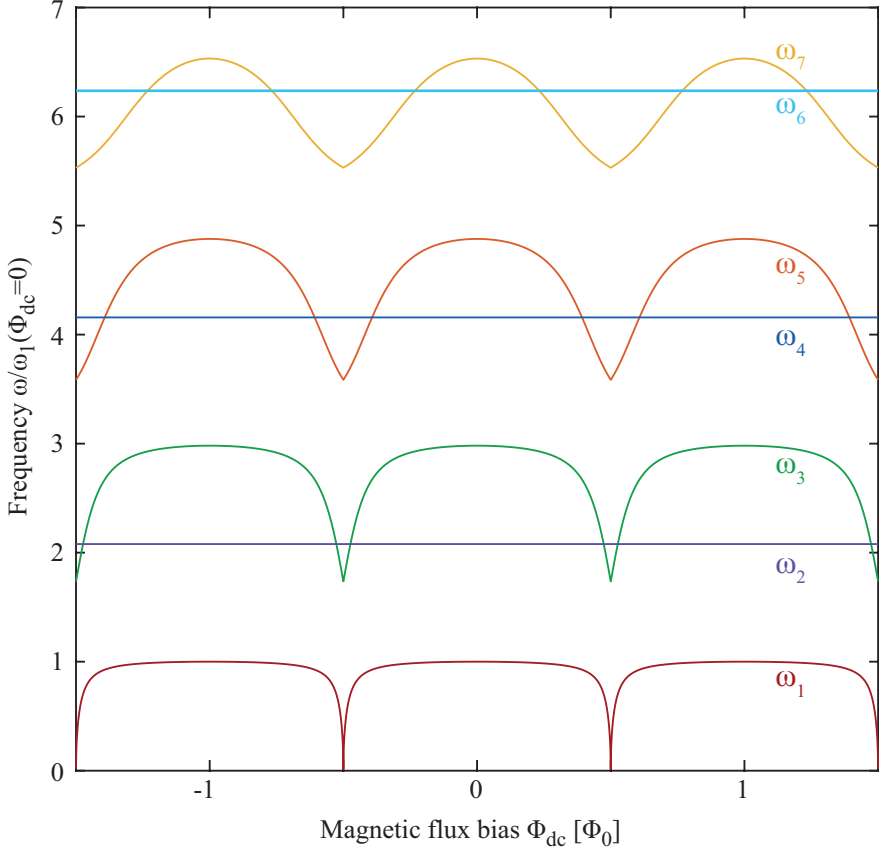
Figure 2.16: *Calculation of the four lowest SQUID-sensitive and the three lowest SQUID-insensitive modes in the coupling resonator, Eq. (2.40).*

By taking the determinant of the system equal to zero we find

$$\sin \frac{k_n d}{2} \left(k_n d \tan \frac{k_n d}{2} - \frac{2}{\gamma_0} \cos \frac{\Phi \pi}{\Phi_0} + 2c(k_n d)^2 \right) = 0, \tag{2.40}$$

which defines two sets of modes. One set that is independent of the SQUID, where $\sin(k_n d/2) = 0$, and one set that depend on the SQUID, defined by the parenthesis equal to zero. It can be noted that the SQUID-dependent part is very close to the dispersion relation for a $\lambda/4$-resonator, compare with Eq. (2.28). A calculation of the resonator spectrum is found in Fig. 2.16.

For the lowest resonator mode, the capacitive contribution is negligible and the dispersion relation can be rewritten

$$\frac{1}{k_1 d} \cot \frac{k_1 d}{2} = \frac{\gamma_0}{2 \cos \frac{\Phi \pi}{\Phi_0}}.$$

$\cot k_1 d/2$ can be expanded around $k_1 d/2 = \pi/2$ which corresponds to a plain resonator without a SQUID, yielding

$$-\frac{1}{k_1 d}\left(\frac{k_1 d}{2} - \frac{\pi}{2}\right) = \frac{\gamma_0}{2\cos\frac{\Phi\pi}{\Phi_0}},$$

which can be simplified

$$\omega_1 = \frac{\omega_0}{1 + \frac{\gamma_0}{\cos\frac{\Phi\pi}{\Phi_0}}}.$$

Here ω_0 denotes the bare resonance frequency of the resonator without a SQUID. When we only care about the lowest mode, this simplified formula is enough.

2.3.2 The nonlinearity parameter and bifurcation

The SQUID in the resonator induces a Kerr-type nonlinearity denoted α. For weak excitation, the nonlinear superconducting resonator can be compared to a Duffing oscillator [49]. The nonlinearity in mode n depends on the inductive participation ratio γ and is expressed [23, 24]

$$\alpha_n = \frac{\hbar\omega_n^2}{2\gamma E_{L,cav}}\left[\frac{\cos(k_n d)^2}{M_n(k_n d)^2}\right]^2,$$

for the $\lambda/4$-resonator in Fig. 2.9(b). Here $M_n = 1 + \sin(2k_n d)/(2k_n d) + 2c\cos^2(k_n d)$ is the generalized mode mass, and $E_{L,cav} = (\hbar/2e)^2/L_0 d$ is the inductive energy of the resonator. Note that α is flux dependent since ω_n, k_n and γ all depend on flux.

For the doubly tunable resonator, the nonlinearity parameter is a sum of the two SQUID contributions

$$\alpha_n = \alpha_{n,r} + \alpha_{n,l} = \frac{\hbar\omega_n^2}{2\gamma_r E_{L,cav}}\left[\frac{\cos(k_n d + \beta_n)^2}{M_n(k_n d)^2}\right]^2 + \frac{\hbar\omega_n^2}{2\gamma_l E_{L,cav}}\left[\frac{\cos(k_n d - \beta_n)^2}{M_n(k_n d)^2}\right]^2$$

$$= \frac{1}{2E_{L,cav}}\frac{\hbar\omega_n^2}{M_n^2(k_n d)^4}\left[\frac{\cos(k_n d + \beta_n)^4}{\gamma_r} + \frac{\cos(k_n d - \beta_n)^4}{\gamma_l}\right]. \qquad (2.41)$$

and the mode mass for the doubly tunable resonator is $M_n = 1 + \sin(k_n d)\cos(2\beta_n)/(k_n d) + 2c_r\cos^2(k_n d/2 + \beta_n) + 2c_l\cos^2(k_n d/2 - \beta_n)$.

The nonlinear effect in the tunable resonator arises due to the limited critical current in the SQUIDs. When the resonator is loaded with a microwave signal, a current flows through the SQUID. If this current $I \ll I_c$, the resonator gives a linear response to a probe signal. If this current $I \gg I_c$, the SQUID loses its superconductivity and does not behave like a SQUID any more. In this case the resonator response should be weak due to the losses in the normal state metal. However, there is also a regime in the middle where the current does not cause saturation but only a nonlinear response to a probe signal.

If the input microwave field is denoted B and the field built up inside the resonator is called A, the resonator response is [24]

$$|A|^2 = \frac{2\Gamma_{ext}}{|\zeta + i\Gamma|^2}|B|^2, \qquad (2.42)$$
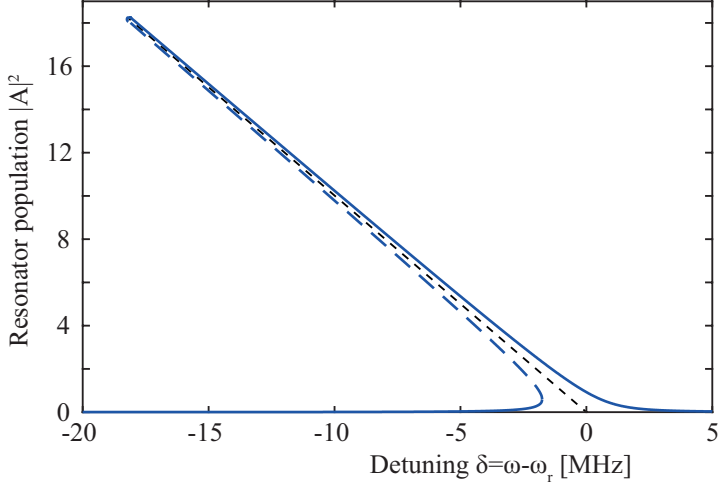
Figure 2.17: *Bifurcated standard Duffing oscillator for a fixed value of $|B|^2$. The dashed line illustrates the unstable branch, and the solid line the stable.*

where $\zeta = \delta - \delta\omega$. Here $\delta = \omega - \omega_r$ is the detuning between the probe signal and the resonance frequency. The microwave fields A and B are normalized such that $|A|^2$ is given in number of photons and $|B|^2$ is in number of photons per second. The nonlinear shift of the resonance frequency is denoted $\delta\omega$ and can be expressed

$$\delta\omega = -\alpha|A|^2. \tag{2.43}$$

To analyse the nonlinear behaviour, the response in Eq. (2.42) can be rewritten as

$$|A|^2 = \frac{2\Gamma_{ext}}{\delta^2 + 2\alpha\delta|A|^2 + |A|^4 + \Gamma^2}|B|^2.$$

This equation has for some regimes several solutions, A, for a given input field, B, and detuning δ. The resonator response bifurcates, it splits into two branches, see Fig. 2.17. The dashed black line correspond to the exact resonance that is shifted due to the nonlinearity. The two branches are marked as dashed blue line for the unstable solution, and solid blue line for the stable solution.

2.4 Nonadiabatic modulation of a SQUID

The SQUID nonlinearity can be used in different ways. Effectively, this nonlinearity acts as a tunable inductance, Eq. (2.7), which can be modulated using either an external drive signal, I which drives a current through the SQUID (current driving) or by modulating the flux, $\Phi_{ext} = \Phi_{ac}(t) + \Phi_{dc}$ in the SQUID loop (flux pumping). What I here define as current driving is commonly referred to in the literature as just "driving the SQUID" or "driving with an external signal".
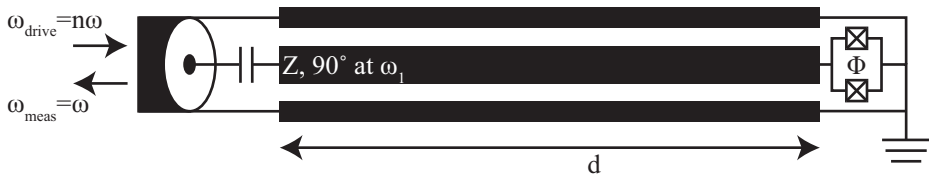
Figure 2.18: *To create subharmonic oscillations, the system is driven by an external signal at a frequency $n\omega$, through frequency down-conversion, a response is produced at the frequency ω.*

In the case of current driving, an input signal B is applied to the input port. This signal generates a current through the SQUID. As explained by the DC Josephson relation, $I = I_c \sin\theta$, this current drives the superconducting phase difference in the SQUID. By modulating the SQUID nonlinearity I can generate subharmonic oscillations through frequency down-conversion. My definition of subharmonic oscillations is that I modulate the SQUID at a frequency $n\omega$, where n is an integer, and I measure a response at ω, see illustration in Fig. 2.18.

In the case of flux pumping a symmetric SQUID, the pump directly modulates the inductance of the SQUID, thus acting as a parametric pump. This is a direct modulation of the resonator boundary condition, which could be thought of as the analogy of moving a physical mirror [50, 51]. At frequencies around $10\,\mathrm{GHz}$ (two times the resonance frequency of a $5\,\mathrm{GHz}$ resonator), this is equivalent to a mirror that is moved at a speed around 25% of the speed of light. Flux pumping a symmetric SQUID only gives frequency down-conversion if the flux pump is fixed to an even multiple of ω. However, if the SQUID junctions are different then the SQUID is asymmetric. With an asymmetric SQUID frequency down-conversion can occur and subharmonic oscillations can be measured for both even and odd multiples. The asymmetry of the SQUID generate a current when flux pumped, in turn this current drives the SQUID.

I follow theory and notation from Refs. [23, 24]. In this thesis both current driving and flux pumping has been used. Current driving has been used to generate subharmonic oscillations through frequency down-conversion (Paper A) while flux pumping has been used for parametric pumping (Paper C) as well as generating subharmonic oscillations (Paper B) and frequency up-conversion. In this thesis I have chosen to go into detail on the theory behind the current driven period tripling subharmonic oscillations and I present the theory for photon generation through flux pumping the doubly tunable resonator.

The concepts presented here are interesting from a fundamental physics point of view because they allow the manipulation of single photons. An understanding and control of the system could allow for applications in a quantum network as sources of nonclassical states, such as multipartite entanglement, squeezing and Schrödinger cat states.

2.4.1 Period tripling subharmonic oscillations

Recently a theoretical study on period-tripling in the quantum regime has been published [52]. Searching some years back in time also theoretical studies of three-photon down-conversion in optical systems are found [53–55]. In this thesis the subharmonic oscillations

Figure 2.19: *Frequency diagram indicating the first two modes of a $\lambda/4$-resonator with positive anharmonicity, $3\omega_1 - \omega_2 > 0$. The arrows indicate a measurement signal, ω and the drive signal at 3ω. The measurement signal is placed at negative detuning δ_1, which results in a positive detuning δ_2.*

are treated quasi-classically.

For current driving of a $\lambda/4$ resonator at 3ω, the configuration is found in Fig. 2.19. The measurement frequency, ω, is placed slightly below ω_1, at negative detuning δ_1. Then the driving frequency 3ω is placed slightly above ω_2, assuming an anharmonicity of the resonator spectrum as in Fig. 2.11. We assume a scenario with two interacting modes. In principle also the higher modes could contribute, however since they are far away we neglect these presumably small contributions. The equations of motion can be written in the rotating frame of ω_1 and ω_2 as [56, 57]

$$i\dot{a}_1 + (\delta_1 + i\Gamma_1 + \alpha_1 a_1^\dagger a_1 + 2\alpha a_2^\dagger a_2)a_1 + \tilde{\alpha}a_1^{\dagger 2}a_2 = 0 \tag{2.44a}$$

$$i\dot{a}_2 + (\delta_2 + i\Gamma_2 + \alpha_2 a_2^\dagger a_2 + 2\alpha a_1^\dagger a_1)a_2 + \frac{\tilde{\alpha}}{3}a_1^3 = \sqrt{2\Gamma_{2,ext}}B_2. \tag{2.44b}$$

where $\alpha = \sqrt{\alpha_1\alpha_2}$ and $\tilde{\alpha} = \sqrt[4]{\alpha_1^3\alpha_2}$ and $a_{1/2}$ and $a_{1/2}^\dagger$ are the annihilation and creation operators of the first and second resonator mode. In the second equation, the external drive signal, B_2, is found on the right hand side. On the left hand side, in both equations, contributions from both the Kerr and the cross Kerr effect can be found. In Eq. (2.44a), the last term, $\tilde{\alpha}a_1^{\dagger 2}a_2$, gives a very special type of interaction rarely observed. The drive signal populates the second mode which in turn becomes a parametric pump on the first mode. In fact, the existence of the second mode strongly enhances the down-conversion effect. In the bottom equation, an a_1^3-term can be found, this is the back-action of the subharmonic oscillations, on the second mode.

The equations of motion in Eqs. (2.44) can be derived from the quantum Hamiltonian

$$H/\hbar = -\sum_{n=1,2}\left(\delta_n a_n^\dagger a_n + \frac{\alpha_n}{2}a_n^{\dagger 2}a_n^2\right) - 2\alpha\, a_1^\dagger a_1 a_2^\dagger a_2$$

$$-\frac{\tilde{\alpha}}{3}\left(a_1^{\dagger 3}a_2 + a_1^3 a_2^\dagger\right) + \sqrt{2\Gamma_{2,ext}}\left(B_2 a_2^\dagger + B_2^* a_2\right). \tag{2.45}$$

This Hamiltonian generates a phase space distribution with four maximas and minimas, four states, one in the middle with zero amplitude, and three in a triangle with finite amplitude, see Fig. 2.20.

For solving Eqs. (2.44) it is convenient to use the parametrization

$$a_1 = r_1 e^{i\phi_1}, \quad a_2 = \frac{r_2}{\beta}e^{i\phi_2}, \quad \beta = \sqrt[4]{\alpha_2/\alpha_1}.$$
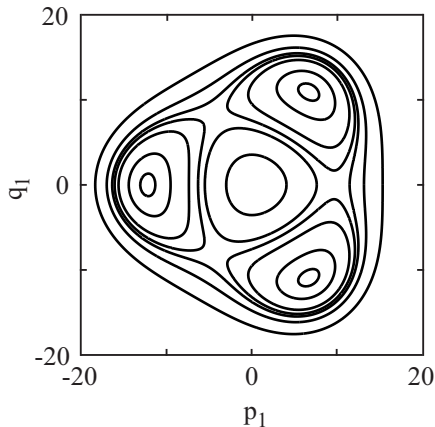
Figure 2.20: *Phase portrait, contours of the phase space distribution described by the Hamiltonian in Eq. (2.45), of a third order subharmonic oscillator. This specific plot is generated for $\delta_1/2\pi = 12$ MHz, $\alpha_1/2\pi = 85$ kHz and $|B_2|^2 = 6.25 \times 10^{10}$ photons/s.*

Then it follows from the equations of motion that in the stationary state, the system is described by

$$\left(\frac{\delta_1}{\alpha_1} + i\frac{\Gamma_1}{\alpha_1} + r_1^2 + 2r_2^2\right)r_1 + r_1^2 r_2 e^{-i\theta} = 0 \tag{2.46a}$$

$$\left(\frac{\delta_2}{\alpha_1} + i\frac{\Gamma_2}{\alpha_1} + \beta^2(r_2^2 + 2r_1^2)\right)r_2 + \frac{\beta^2}{3}r_1^3 e^{i\theta} = \frac{\beta}{\alpha_1}\sqrt{2\Gamma_{2,ext}}B_2 e^{-i\phi_2}, \tag{2.46b}$$

where $\theta = 3\phi_1 - \phi_2$. First, note the trivial solution to Eq. (2.46a), $r_1 = 0$. This solution describes an oscillator with zero amplitude, which could be called a silent oscillator state. To investigate the stability of this trivial solution we linearise Eq. (2.44a) for a small fluctuation δa_1 around the solution $a_{1,0}$. This gives the equation

$$i\delta\dot{a}_1 + \left(\delta_1 + i\Gamma_1 + \alpha_1|a_{1,0} + \delta a_1|^2 + 2\alpha|a_2|^2\right)(a_{1,0} + \delta a_1) + \tilde{\alpha}(a_{1,0}^* + \delta a_1^*)^2 a_2 = 0. \tag{2.47}$$

We assume $a_1 \propto e^{\lambda_0 t}$ and insert the trivial solution $a_{1,0} = 0$. We also neglect higher order δa_1-terms since they are small, yielding $i\delta a_1 \lambda_0 + (\delta_1 + i\Gamma_1 + 2\alpha|a_2|^2)\delta a_1 = 0$, which can be rewritten as

$$\lambda_0 = i(\delta + 2\alpha|a_2|^2) - \Gamma_1.$$

Since $\text{Re}[\lambda_0]$ is negative everywhere, the trivial solution is always stable.

Separating Eq. (2.46a) into real and imaginary part, we get

$$\frac{\delta_1}{\alpha_1} + r_1^2 + 2r_2^2 = -r_1 r_2 \cos\theta \tag{2.48a}$$

$$\frac{\Gamma_1}{\alpha_1} = r_1 r_2 \sin\theta. \tag{2.48b}$$

Then the phase θ can be eliminated by combining the two equations

$$r_1^2 = -\frac{\delta_1}{\alpha_1} - \frac{3}{2}r_2^2 \pm \sqrt{-\frac{\delta_1}{\alpha_1}r_2^2 - \frac{7}{4}r_2^4 - \frac{\Gamma_1^2}{\alpha_1^2}}. \tag{2.49}$$

Since r_1^2 should be real, this implies the condition $-(\delta_1/\alpha_1)r_2^2 - (7/4)r_2^4 - \Gamma_1^2/\alpha_1^2 > 0$ which defines a range

$$r_2^2 \in \{r_{2-}^2,\ r_{2+}^2\}, \quad r_{2\pm}^2 = \frac{2|\delta_1|}{7\alpha_1}\left[1 \pm \sqrt{1 - 7\frac{\Gamma_1^2}{\delta_1^2}}\right], \tag{2.50}$$

where the solution exist. Furthermore, this implies that the possible solutions only exist at finite negative detuning, given by the damping rate

$$\delta_1 \ \leq\ -\sqrt{7}\,\Gamma_1. \tag{2.51}$$

The phase $\theta = 3\phi_1 - \phi_2$ is given by Eq. (2.48)

$$\sin(3\phi_1 - \phi_2) = \frac{\Gamma_1}{\alpha_1 r_1 r_2} > 0 \tag{2.52a}$$

$$\cos(3\phi_1 - \phi_2) = \pm\sqrt{1 - \left(\frac{\Gamma_1}{\alpha_1 r_1 r_2}\right)^2} = -\frac{\frac{\delta_1}{\alpha_1} + r_1^2 + 2r_2^2}{r_1 r_2}. \tag{2.52b}$$

For every value of ϕ_2, there are three possible solutions for ϕ_1, a threefold degeneracy and the solutions are phase shifted by $2\pi/3$ with respect to each other. Summarizing, Eqs. (2.44) have a stable trivial solution, $r_1 = 0$, as well as some non-trivial solutions, $r_1 > 0$ (since it is an amplitude r_1 has to be positive). The Eqs. (2.49) and (2.52) give two possible amplitude solutions and a triplet phase solution.

To investigate the stability of the nontrivial solutions we use the linearised system Eq. (2.47). To simplify the analysis we assume $|\delta_1| \gg \Gamma_1$. Remembering that both r_1 and r_2 go as δ_1, simplifies Eq. (2.48b) to $\sin\theta = 0$, which implies $\theta = 3\phi_1 - \phi_2 = 0, \pi$. In turn, this allows us to simplify Eq. (2.48a) to

$$r_1 \cos\theta = \pm\left(\frac{1}{2}r_2 \pm \sqrt{-\frac{\delta_1}{\alpha_1} - \frac{7}{4}r_2^2}\right), \tag{2.53}$$

where the sign in front of the parentheses is given by the value of the phase θ. We rewrite Eq. (2.47), neglecting the damping and expanding the terms

$$|a_{1,0} + \delta a_1|^2 = (a_{1,0} + \delta a_1)(a_{1,0}^* + \delta a_1^*) = |a_{1,0}|^2 + a_{1,0}\delta a_1^* + a_{1,0}^*\delta a_1 + |\delta a_1|^2$$

and

$$(a_{1,0}^* + \delta a_1^*)^2 = a_{1,0}^{*2} + 2a_{1,0}^*\delta a_1^* + \delta a_1^{*2}$$

to

$$i\delta\dot{a}_1 + (\delta_1 + \alpha_1(|a_{1,0}|^2 + a_{1,0}\delta a_1^* + a_{1,0}^*\delta a_1) + 2\alpha|a_2|^2)(a_{1,0} + \delta a_1) + \tilde{\alpha}(a_{1,0}^{*2} + 2a_{1,0}^*\delta a_1^*)a_2 = 0.$$

Sorting the terms give

$$i\delta\dot{a}_1 + a_{1,0}(\delta_1 + \alpha_1|a_{1,0}|^2 + 2\alpha|a_2|^2) + \tilde{\alpha}a_{1,0}^{*2}a_2$$
$$+\delta a_1(\delta_1 + 2\alpha_1|a_{1,0}|^2 + 2\alpha|a_2|^2)$$
$$+\delta a_1^*(\alpha_1 a_{1,0}^2 + 2\tilde{\alpha}a_{1,0}^*a_2) = 0.$$

We are only interested in the dynamic part and therefore we extract this part and we substitute δa_1 with $\delta\tilde{a}_1 e^{i\phi_1}$. In addition we insert $a_{1,0} = r_1 e^{i\phi_1}$ and $a_2 = \frac{r_2}{\beta}e^{i\phi_2}$, which gives

$$i\delta\dot{\tilde{a}}_1 e^{i\phi_1} + \delta\tilde{a}_1 e^{i\phi_1}(\delta_1 + 2\alpha_1 r_1^2 + 2\alpha_1 r_2^2) + \delta\tilde{a}_1^* e^{-i\phi_1}(\alpha_1 r_1^2 e^{i2\phi_1} + 2\alpha_1 r_1 r_2 e^{i(\phi_2-\phi_1)}) = 0.$$

The last term can be rewritten

$$\delta\tilde{a}_1^* e^{-i\phi_1}(\alpha_1 r_1^2 e^{i2\phi_1} + 2\alpha_1 r_1 r_2 e^{i(\phi_2-\phi_1)})$$
$$= \alpha_1 e^{i\phi_1}\delta\tilde{a}_1^*(r_1^2 \pm 2r_1 r_2),$$

where the plus is for $\phi_2 - 3\phi_1 = 0$ and the minus sign is for $\phi_2 - 3\phi_1 = -\pi$. Then we have

$$i\delta\dot{\tilde{a}}_1 + \delta\tilde{a}_1(\delta_1 + 2\alpha_1 r_1^2 + 2\alpha_1 r_2^2) + \delta\tilde{a}_1^*(\alpha_1 r_1^2 \pm 2\alpha_1 r_1 r_2) = 0.$$

From Eq. (2.52b) we have $\pm r_1 r_2 = -\left(\delta_1/\alpha_1 + r_1^2 + 2r_2^2\right)$, which yields

$$i\delta\dot{\tilde{a}}_1 + \delta\tilde{a}_1(\delta_1 + 2\alpha_1 r_1^2 + 2\alpha_1 r_2^2) - \delta\tilde{a}_1^*(2\delta_1 + \alpha_1 r_1^2 + 4\alpha_1 r_2^2) = 0.$$

If we then set $\delta\tilde{a}_1 = x + iy$, assuming x and y are real numbers $\propto e^{\lambda_1\alpha_1 t}$, and sum up the real and imaginary parts of the equation

$$-\lambda_1\alpha_1 y + x(-\delta_1 + \alpha_1 r_1^2 - 2\alpha_1 r_2^2) = 0 \qquad (2.54a)$$
$$\lambda_1 x + 3y(\delta_1 + \alpha_1 r_1^2 + 2\alpha_1 r_2^2) = 0. \qquad (2.54b)$$

Eliminating x/y gives

$$-\alpha_1^2\lambda_1 = 3\left(\delta_1 + \alpha r_1^2 + 2\alpha_1 r_2^2\right)\left(-\delta_1 + \alpha_1 r_1^2 - 2\alpha_1 r_2^2\right),$$

where δ_1 can be eliminated using Eq. (2.52b),

$$-\alpha_1^2\lambda_1 = 3\alpha_1^2\left(\mp r_1 r_2\right)\left(2r_1^2 \pm r_1 r_2\right)$$

which in turn can be rewritten

$$\lambda_1^2 = \pm 6r_1^2 r_2\left(r_1 \pm \frac{r_2}{2}\right). \qquad (2.55)$$

Note that $r_1 \pm \frac{r_2}{2} = \pm\sqrt{-\frac{\delta_1}{\alpha_1} - \frac{7}{4}r_2^2}$ from Eq. (2.53). This yields, for the minus sign in front of Eq. (2.55),

$$\lambda_1^2 = -6r_1^2 r_2\left(\pm\sqrt{-\frac{\delta_1}{\alpha_1} - \frac{7}{4}r_2^2}\right).$$

Here $\lambda_1^2 < 0$ for the positive root, *i.e.* the positive root gives a stable solution. Hence, for a stable solution we need the combination of a minus sign in front of the parentheses and plus in front of the root in Eq. (2.53), which implies that the plus sign in front of the root in Eq. (2.49) corresponds to a stable triplet solution. The other possible sign combination lead to $\lambda^2 > 0$ and hence an unstable solution. To summarize, the stable solution is

$$r_1^2 = -\frac{\delta_1}{\alpha_1} - \frac{3}{2}r_2^2 + \sqrt{-\frac{\delta_1}{\alpha_1}r_2^2 - \frac{7}{4}r_2^4 - \frac{\Gamma_1^2}{\alpha_1^2}} \qquad (2.56)$$

and the phase $\theta = \pi$.

A closer look at Eq. (2.46b) shows it to be of the format of a Duffing oscillator perturbed by the back-action of the subharmonic oscillations. The phase ϕ_2 is defined by the imaginary part of that equation

$$\frac{\Gamma_2}{\alpha_1}r_2 + \frac{\beta^2}{3}r_1^3\sin(3\phi_1 - \phi_2) = \frac{\beta}{\alpha_1}\sqrt{2\Gamma_{2,ext}}\,|B_2|\sin(\phi_B - \phi_2), \qquad (2.57)$$

where ϕ_B denotes the phase of the drive signal B_2. If we assume small damping, $\Gamma_2 \ll \delta_1$, and remember that $3\phi_1 - \phi_2 = 0, \pi$, we conclude that also $\phi_B - \phi_2 = 0, \pi$. Consequently, given that $3\omega_1 - \omega_2 = \Delta$, the spectrum anharmonicity, the amplitude of the response is given by

$$\left[\left(3\frac{\delta_1}{\alpha_1} + \frac{\Delta}{\alpha_1} + \beta^2\left(r_2^2 + 2r_1^2\right)\right)r_2 - \frac{\beta^2}{3}r_1^3\right]^2 + \frac{\Gamma_2^2}{\alpha_1^2}r_2^2 = 2\beta^2\frac{\Gamma_{2,ext}}{\alpha_1^2}|B_2|^2. \qquad (2.58)$$

Analytical analysis can only be done on a simplified system. Therefore stability analysis on the full system has to be done graphically. From Eq.(2.58) $r_2^2(\delta)$ can be evaluated for different values of B_2, see the contours in Fig. 2.21. Here the phase ϕ_2 is taken into account as the sign of B_2, $B_2 > 0$ corresponds to $\phi_2 = \phi_B$ (red coloured contours) and $B_2 < 0$ corresponds to $\phi_2 = \phi_B + \pi$ (blue coloured contours). The exact resonance $B_2 = 0$ is given by the dashed black line. The analogy with a Duffing oscillator, see Fig. 2.17, tells which solutions are stable and which are unstable. Below resonance the solutions are unstable and above resonance they are stable. This means that in panel (a) of Fig. 2.21 most solutions were $B_2 > 0$ are stable, while the solutions where $B_2 < 0$ are unstable. In panel (b) and (c), the lower branch of $B_2 > 0$ correspond to stable solutions while the blue part is unstable together with the upper red branch. In panel (d), where the anharmonicity has changed sign from positive to negative, there is a second resonance. Above this second resonance the solutions are stable.

To further investigate the stability, line cuts of Fig. 2.21 can be extracted, see Fig. 2.22. Here B_2 is squared and no information of ϕ_2 can be deduced. Unstable branches are marked by dashed lines while the stable are solid lines. In this graph we find, at small r_2-values, the lower blue branch from Fig. 2.22, which is unstable. In addition we find a backbending of the curve at larger r_2-values most pronounced for smaller anharmonicity $\Delta/\alpha_1 \leq 50$, where $\Delta = 3\omega_1 - \omega_2$. This backbending correspond to the upper red branch in Fig. 2.21, claimed to be unstable. This effectively decreases the upper boundary for the subharmonic oscillations. For $\Delta/\alpha_1 = -10$ there is an additional structure at large r_2, this corresponds to the upper blue branch of Fig. 2.21(d) and is supposedly stable.
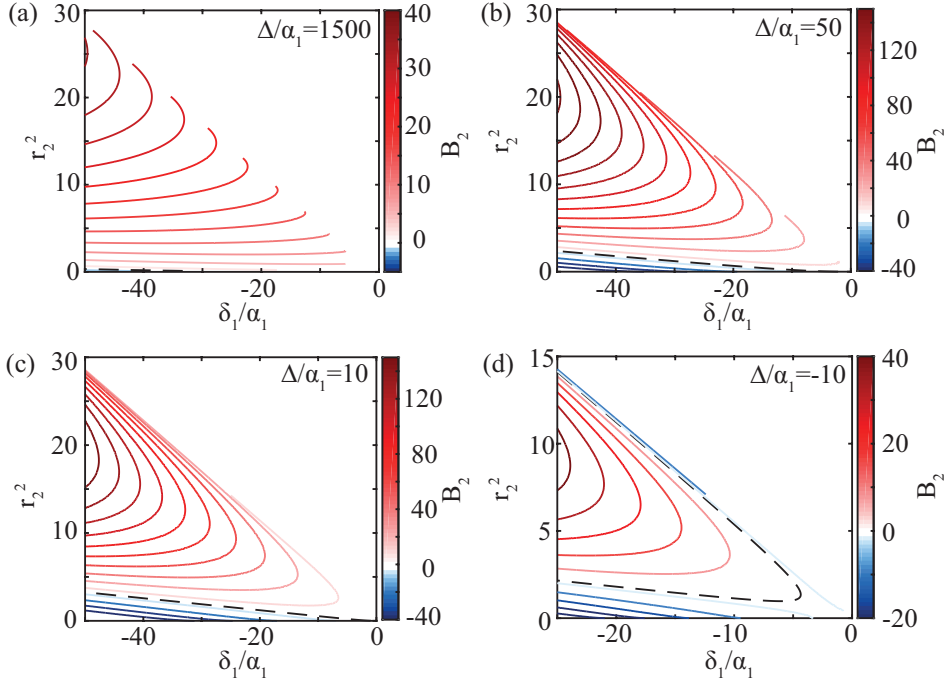
Figure 2.21: *Graphs illustrating the dependence $r_2^2(\delta)$ given by Eq. (2.58). The sign on the colour scale gives the phase ϕ_2. The curves in the figure can be compared to a Duffing oscillator (Fig. 2.17). Exact resonance, $B_2 = 0$, is highlighted by the dashed black line and the branch above the resonance can be assumed stable and below unstable. The four panels are shown for different values of the anharmonicity, $\Delta = 3\omega_1 - \omega_2$.*
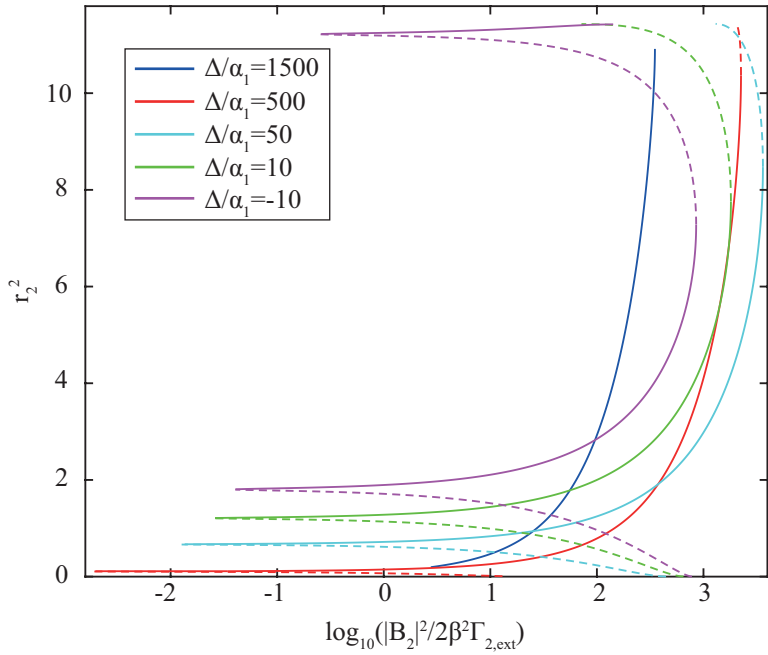
Figure 2.22: *Illustration of the $r_2^2(B_2)$-dependence for different anharmonicities, $\Delta = 3\omega_1 - \omega_2$, of the spectrum, i.e. different flux values. The dashed lines correspond to supposedly unstable branches and the solid lines to stable.*

For analysis of measurement data it is convenient to work with simplified formulas. For a resonator where the anharmonicity is much larger than the detuning, $|\delta_1| \ll 3\omega_1 - \omega_2$, and r_1^2, $r_2^2 \lesssim |\delta_1|/\alpha_1$, the expression in Eq. (2.58) can be simplified to

$$(3\omega_1 - \omega_2)^2 r_2^2 = 2\beta^2 \Gamma_{2,ext} |B_2|^2. \tag{2.59}$$

Here r_2^2 can be rewritten in terms of r_1^2 using Eq. (2.49). This is then a direct relation between the drive signal, B_2, and the measured output signal, which depend on r_1^2. In addition, the maximum output produced by the drive can be calculated by taking the derivative of Eq. (2.49) with respect to δ_1. This gives

$$r_{1,max}^2 = \frac{4}{7\alpha_1} \left(|\delta_1| + \sqrt{|\delta_1|^2 - 7\Gamma_1^2} \right). \tag{2.60}$$

Notably the intensity of the oscillations is decreasing when the flux bias approaches $\pm\Phi_0/2$, since the nonlinearity parameter α_1 is increasing.

2.4.2 Standard parametric oscillations

Standard parametric oscillations are created by modulating the flux in the SQUID-loop at two times the resonance frequency of a resonator mode or at the sum of two modes, so called degenerate or non-degenerate photon generation [7, 58, 59]. In this section I focus on parametric oscillations in the $\lambda/4$ resonator of Fig. 2.9(b). The dynamics of the flux pumped SQUID in the resonator end is described by the equation of motion (for degenerate pumping)

$$i\dot{A}_n + \delta A_n + \epsilon A_n^* + \alpha_n |A_n|^2 A_n + i\Gamma_{0,n} A_n = 0. \tag{2.61}$$

Here, A_n denotes the field inside the resonator in mode n, δ is the detuning between half the pump and the mode frequency, $\delta = \omega_p/2 - \omega_n$. Similar to the subharmonic oscillations the equation of motion contains a term related to the Kerr effect. The effective pump strength, ϵ, is given by the expression

$$\epsilon = \frac{(\Phi_{ac}\pi/\Phi_0)\,\omega_n \tan(\Phi_{dc}\pi/\Phi_0)}{\gamma_0/|\cos(\Phi_{dc}\pi/\Phi_0)|} \frac{\cos^2 k_n d}{M_n (k_n d)^2}, \tag{2.62}$$

where Φ_{ac} is the flux pump amplitude in number of flux quanta, Φ_{dc} is the static flux bias, $k_n = \omega_n/v$ is the mode wave number, γ_0 is the inductive participation defined in Section 2.3.1 and the mode mass M_n is given in Section 2.3.2. The parametric oscillations occur above a certain threshold given by the damping Γ and the detuning δ,

$$\epsilon_{thresh,deg} = \sqrt{\Gamma_n^2 + \delta^2}, \tag{2.63}$$

see the dashed black lines in Fig. 2.23. Note that this is the expression for degenerate pumping, pumping where $\omega_p = 2\omega_n$.

The flux pump modulates the resonance frequency following the tuning curves of Fig. 2.11. These curves are nonlinear, which means that the modulation of the resonance

frequency is nonlinear. The stronger the pump, the more nonlinear is the modulation. This leads to an effective shift of the resonance frequency, a pump induced frequency shift

$$\omega_n(\epsilon) - \omega_n(0) = -\frac{\chi_n \epsilon^2}{\Gamma_n},$$

where $\chi_n = \Gamma_n \cos^2\left(\frac{\Phi_{dc}}{\Phi_0}\pi\right) / \left(\omega_n \gamma_0 \left|\sin\left(\frac{\Phi_{dc}}{\Phi_0}\pi\right)\right|\right)$. Hence the effective detuning of the pump can be written

$$\delta_{eff} = \delta + \frac{\chi_n \epsilon^2}{\Gamma_n},$$

which modifies the threshold condition accordingly

$$\epsilon_{thresh,eff} = \sqrt{\Gamma_n^2 + \left(\delta + \frac{\chi_n \epsilon_{thresh,eff}^2}{\Gamma_n}\right)^2}.$$

Solving for $\epsilon_{thresh,eff}$ gives

$$\frac{\epsilon_{thresh,eff}}{\Gamma_n} = \frac{1}{\sqrt{2}\chi_n}\sqrt{1 - \frac{2\delta\chi_n}{\Gamma_n} \pm \sqrt{1 - 4\chi_n(\frac{\delta}{\Gamma_n} + \chi_n)}}. \tag{2.64}$$

This equation is used to calculate the region boundaries (solid lines) presented in Fig. 2.23 for two different flux bias points. The blue lines correspond to the minus sign in Eq. (2.64) and the red line to the plus sign. Within the parametric oscillation region, photons are generated through parametric down-conversion. The number of photons in the resonator is given by the modulus square of the intra resonator field

$$|A_n|^2 = \frac{1}{\alpha_n}(-\delta + \sqrt{\epsilon^2 - \Gamma_n^2}). \tag{2.65}$$

The parametric oscillator can be described by the Hamiltonian

$$H(Q, P) = \frac{\epsilon - \delta}{2}P^2 - \frac{\epsilon + \delta}{2}Q^2 - \frac{\alpha}{8\hbar}(Q^2 + P^2)^2. \tag{2.66}$$

This Hamiltonian defines a metapotential, which can be thought of as a potential with potential wells, between which virtual particles can travel. These potential wells define the possible states of the system. The parametric oscillator can be found in three different regimes, as illustrated in Fig. 2.24. In panel (a) the system has a silent state in the middle and two meta-stable π-shifted states on the sides. In the (b) and (c)-panels the middle state has disappeared and there are only the two π-shifted excited states. Finally, in the (d)-panel there is a squeezed state.

For non-degenerate parametric pumping, the pump frequency is close to the sum of two different mode frequencies, $\omega_p = \omega_n + \omega_m + 2\delta$. The effective pump strength is then

$$\epsilon = \frac{(\Phi_{ac}\pi/\Phi_0)\tan(\Phi_{dc}\pi/\Phi_0)}{\gamma_0/|\cos(\Phi_{dc}\pi/\Phi_0)|}\left(\frac{\sqrt{\omega_n}\cos(k_n d/2)}{\sqrt{M_n}k_n d}\right)\left(\frac{\sqrt{\omega_m}\cos(k_m d/2)}{\sqrt{M_m}k_m d}\right). \tag{2.67}$$
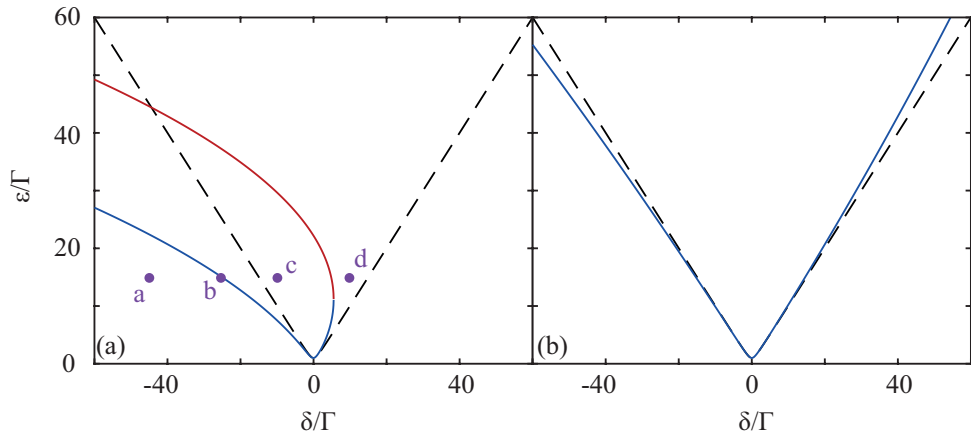
Figure 2.23: *Boundaries of the parametric oscillation region. The dashed black lines illustrate the threshold defined by Eq. (2.63). The solid lines represent the threshold taking into account the pump induced frequency shift, Eq. (2.64). Note that the nonlinearity of the pumping is stronger and more pronounced at $0.1\,\Phi_0$ (a) than at $0.3\,\Phi_0$ (b). This can be understood from the fact that the tuning curve is close to linear to a first approximation at larger flux values. The purple dots in (a) correspond to the points for the phase space distributions in Fig. 2.24.*

Moreover, the threshold for non-degenerate pumping is

$$\epsilon^2_{thresh,non-deg.} = \Gamma_n \Gamma_m + \delta^2 \left[1 - \left(\frac{\Gamma_n - \Gamma_m}{\Gamma_n + \Gamma_m} \right)^2 \right] \qquad (2.68)$$

and the amplitude of the intra resonator field, in mode n is

$$|A_n|^2 = \frac{-\delta + \sqrt{\frac{\Gamma_n}{\Gamma_m}} \sqrt{\epsilon^2 - \Gamma_n \Gamma_m}}{\alpha_n + 2\alpha \frac{\Gamma_n}{\Gamma_m}} \qquad (2.69)$$

with an effective nonlinearity parameter $\alpha = \sqrt{\alpha_n \alpha_m}$. Note that the amplitudes of the two modes follow the relation

$$\Gamma_n |A_n|^2 = \Gamma_m |A_m|^2.$$

2.4.3 Flux pumping the doubly tunable resonator

The doubly tunable resonator is in principle two $\lambda/4$-resonators, coupled with a very strong coupling, compare Fig. 2.9(b) and 2.12. The flux pumped double SQUID resonator can also behave as a parametric oscillator. However, the resonator spectrum is different, there are even and odd modes which gives a parity effect. In addition there are two pump tones that can cause interference effects.

In this system, the flux modulated boundary conditions are an analogy of two moving mirrors. Assuming the two pump frequencies are equal, these mirrors can be set to
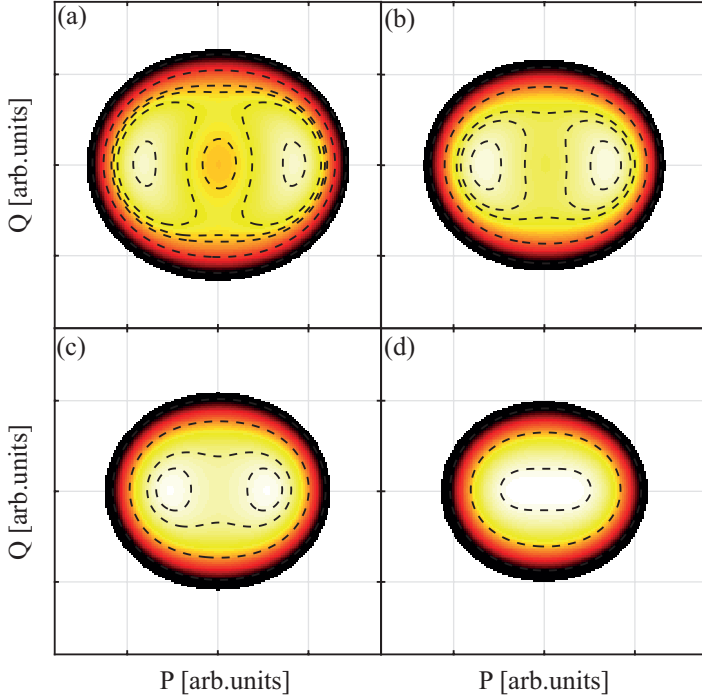
Figure 2.24: *Phase portraits of the different regimes given by the metapotential in Eq. (2.66) of points a-d as indicated by the purple dots in Fig. 2.23. (a) At negative detuning, below the parametric region, the metapotential forms one stable state in the middle and two metastable π-shifted states on the sides. (b) At the lower boundary, the middle state disappears and there are only two π-shifted states. (c) Also in this point we find two π-shifted metastable states. (d) Above the parametric oscillation region the metapotential forms a squeezed state.*

oscillate and form a translational mode, shaking resonator, or a breathing mode, where the effective length of the resonator varies. In literature, several theoretical works from the 1990s investigate this type of system [60–64]. They predict that if pumping at an even multiple of the fundamental mode frequency, there will be constructive interference in the breathing mode and destructive in the translational. On the other hand, if pumping at an odd multiple, there will be constructive interference in the translational mode and destructive in the breathing. These predictions had all in mind mechanical motion of the mirrors, where relativistic speeds are difficult to achieve. However, with a SQUID-tunable resonator this is not a limiting factor [50, 65].

As already mentioned, the flux pumped doubly tunable resonator is essentially a parametric oscillator, but with a different mode structure and two pumps instead of one. The effective pump strength of the system is given by the following set of cases for modes a and b being even (e) or odd (o)

$$
a, b \in (e), \epsilon^2 = \frac{\tan^2\left(\frac{\Phi_{dc}}{\Phi_0}\pi\right)}{4\gamma^2} \left(\frac{\omega_a \cos^2(k_a d/2)}{M_a(k_a d)^2}\right) \left(\frac{\omega_b \cos^2(k_b d/2)}{M_b(k_b d)^2}\right) |\delta f_r + \delta f_l|^2
\tag{2.70a}
$$

$$
a, b \in (o), \epsilon^2 = \frac{\tan^2\left(\frac{\Phi_{dc}}{\Phi_0}\pi\right)}{4\gamma^2} \left(\frac{\omega_a \sin^2(k_a d/2)}{M_a(k_a d)^2}\right) \left(\frac{\omega_b \sin^2(k_b d/2)}{M_b(k_b d)^2}\right) |\delta f_r + \delta f_l|^2
\tag{2.70b}
$$

$$
a \in (e), b \in (o), \epsilon^2 = \frac{\tan^2\left(\frac{\Phi_{dc}}{\Phi_0}\pi\right)}{4\gamma^2} \left(\frac{\omega_a \cos^2(k_a d/2)}{M_a(k_a d)^2}\right) \left(\frac{\omega_b \sin^2(k_b d/2)}{M_b(k_b d)^2}\right) |\delta f_r - \delta f_l|^2 .
\tag{2.70c}
$$

Even and odd modes of the doubly tunable resonator are defined in Fig. 2.14. Here $\delta f_{l/r} = 2\pi\Phi_{ac,l/r}e^{i\phi_{l/r}}/\Phi_0$, $i \in \{l, r\}$, denotes the pump amplitude and phase. The threshold for the double parametric oscillator is the same as for the regular parametric oscillator given for degenerate pumping, $a = b = n$ and $\omega_l = \omega_r = 2\omega_n$, by Eq. (2.63) and for nondegenerate pumping, $a \neq b$ and $\omega_l = \omega_r = \omega_a + \omega_b$, by Eq. (2.68). We find in Eqs. (2.70a) and (2.70b) that pumping at the sum of either two even or two odd modes result in very similar behaviour. Both these give its lowest threshold, constructive interference, at a phase difference $\phi_r - \phi_l = 0$ and a maximum threshold, destructive interference, for $\phi_r - \phi_l = \pm\pi$. In contrast, in the case where the pump is the sum of an even and an odd mode, the interference is the opposite, constructive for $\phi_r - \phi_l = \pm\pi$ and destructive for $\phi_r - \phi_l = 0$.

In Eq. (2.70) it is assumed that the two SQUIDs have the same flux bias and that there is no ac crosstalk. If we first allow the two SQUIDs to have different flux bias, the

formulas are written

$$\epsilon^2 = \frac{1}{4}\left(\frac{\omega_a \cos^2 \frac{k_a d}{2}}{M_a(k_a d)^2}\right)\left(\frac{\omega_b \cos^2 \frac{k_b d}{2}}{M_b(k_b d)^2}\right)\left|\frac{\tan^2\left(\frac{\Phi_{dc,r}}{\Phi_0}\pi\right)}{\gamma_r^2}\delta f_r + \frac{\tan^2\left(\frac{\Phi_{dc,l}}{\Phi_0}\pi\right)}{\gamma_l^2}\delta f_l\right|^2 \quad (2.71a)$$

$$\epsilon^2 = \frac{1}{4}\left(\frac{\omega_a \sin^2 \frac{k_a d}{2}}{M_a(k_a d)^2}\right)\left(\frac{\omega_b \sin^2 \frac{k_b d}{2}}{M_b(k_b d)^2}\right)\left|\frac{\tan^2\left(\frac{\Phi_{dc,r}}{\Phi_0}\pi\right)}{\gamma_r^2}\delta f_r + \frac{\tan^2\left(\frac{\Phi_{dc,l}}{\Phi_0}\pi\right)}{\gamma_l^2}\delta f_l\right|^2 \quad (2.71b)$$

$$\epsilon^2 = \frac{1}{4}\left(\frac{\omega_a \cos^2 \frac{k_a d}{2}}{M_a(k_a d)^2}\right)\left(\frac{\omega_b \sin^2 \frac{k_b d}{2}}{M_b(k_b d)^2}\right)\left|\frac{\tan^2\left(\frac{\Phi_{dc,r}}{\Phi_0}\pi\right)}{\gamma_r^2}\delta f_r - \frac{\tan^2\left(\frac{\Phi_{dc,l}}{\Phi_0}\pi\right)}{\gamma_l^2}\delta f_l\right|^2 , \quad (2.71c)$$

where the three subequations correspond to the three cases in Eq. (2.70). Then a possible ac crosstalk is inserted using the parameter $\xi_{ac,i}$, which could have both an amplitude and a phase, $\xi_{ac,i} = |\xi_{ac,i}|e^{i\phi_{\xi,i}}$. This yields

$$\epsilon^2 = \frac{1}{4}\left(\frac{\omega_a \cos^2 \frac{k_a d}{2}}{M_a(k_a d)^2}\right)\left(\frac{\omega_b \cos^2 \frac{k_b d}{2}}{M_b(k_b d)^2}\right)$$
$$\left|\frac{\tan^2\left(\frac{\Phi_{dc,r}}{\Phi_0}\pi\right)}{\gamma_r^2}[\delta f_r + \xi_{ac,l}\delta f_l] + \frac{\tan^2\left(\frac{\Phi_{dc,l}}{\Phi_0}\pi\right)}{\gamma_l^2}[\delta f_l + \xi_{ac,r}\delta f_r]\right|^2 \quad (2.72a)$$

$$\epsilon^2 = \frac{1}{4}\left(\frac{\omega_a \sin^2 \frac{k_a d}{2}}{M_a(k_a d)^2}\right)\left(\frac{\omega_b \sin^2 \frac{k_b d}{2}}{M_b(k_b d)^2}\right)$$
$$\left|\frac{\tan^2\left(\frac{\Phi_{dc,r}}{\Phi_0}\pi\right)}{\gamma_r^2}[\delta f_r + \xi_{ac,l}\delta f_l] + \frac{\tan^2\left(\frac{\Phi_{dc,l}}{\Phi_0}\pi\right)}{\gamma_l^2}[\delta f_l + \xi_{ac,r}\delta f_r]\right|^2 \quad (2.72b)$$

$$\epsilon^2 = \frac{1}{4}\left(\frac{\omega_a \cos^2 \frac{k_a d}{2}}{M_a(k_a d)^2}\right)\left(\frac{\omega_b \sin^2 \frac{k_b d}{2}}{M_b(k_b d)^2}\right)$$
$$\left|\frac{\tan^2\left(\frac{\Phi_{dc,r}}{\Phi_0}\pi\right)}{\gamma_r^2}[\delta f_r - \xi_{ac,l}\delta f_l] - \frac{\tan^2\left(\frac{\Phi_{dc,l}}{\Phi_0}\pi\right)}{\gamma_l^2}[\delta f_l - \xi_{ac,r}\delta f_r]\right|^2 . \quad (2.72c)$$

Of course the analogy of the translational and the breathing mode will be increasingly difficult, if not impossible to make for larger pump crosstalk.

The effective pump strengths of Eqs. (2.71) can be inserted in Eq. (2.64) to extract the parametric regions. If we only look at $\delta = 0$, there is no need to include the pump induced frequency shift. For three different types of flux bias points, the parametric thresholds are plotted in Fig. 2.25 for (a) pumping at the sum of two even modes and (b) for pumping at the sum of an even and an odd mode. The horizontal axes indicate the phase difference between the two pump signals $\phi_r - \phi_l$. The flux bias of the left SQUID is fixt to $\Phi_{dc,l} = 0.45\,\Phi_0$, which means that it is placed on a steep frequency slope
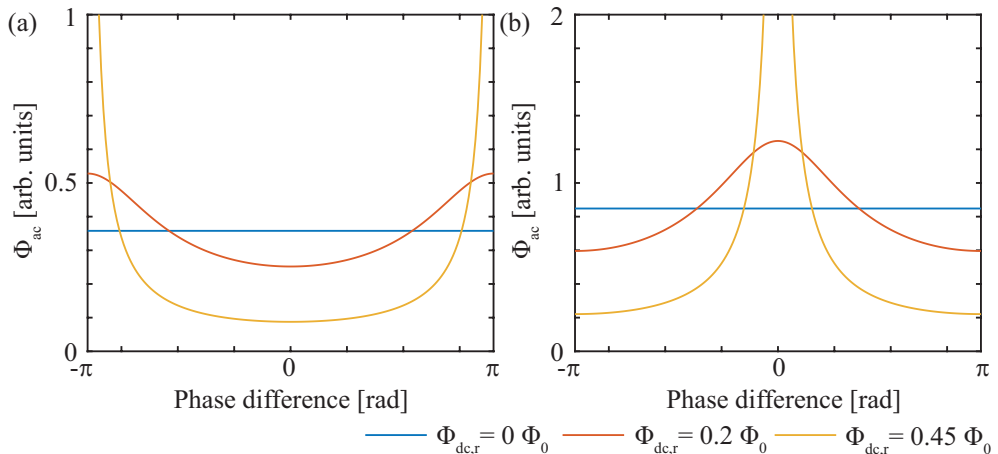
Figure 2.25: *Thresholds at zero detuning for parametric oscillations created by pumping the doubly tunable resonator using two pumps with a phase difference. (a) Pumping at a sum of two even modes. (b) Pumping at the sum of an even and an odd mode. Note how the threshold minimum in (a) is at zero phase difference while in (b) at $\pm\pi$. For all curves the magnetic flux bias in the left SQUID is $\Phi_{dc,l} = 0.45$, while the colours denote different flux bias values for the right SQUID.*

(Fig. 2.13). In contrast, the flux bias in the right SQUID varies for the three different lines. The blue line is given for $\Phi_{dc,r} = 0\,\Phi_0$, which corresponds to a bias point on a frequency maxima. This means that the right flux pump does not have any effect. Hence, the blue lines are not affected by the phase difference between the pumps and correspond to a single pump system, essentially a standard single SQUID parametric oscillator. The red and the yellow lines represent two non-zero values of $\Phi_{dc,r}$, where the yellow one is a symmetric bias point, $\Phi_{dc,r} = \Phi_{dc,l}$. Due to the symmetric bias point the yellow line shows full destructive interference while the red curve shows a weaker interference effect.

Figure 2.25 is made assuming zero crosstalk. A possible inductive crosstalk, $\phi_{\xi,i} = 0$ and $\xi_{ac,i} \in \mathbb{R}$, only affects the threshold level while a capacitive crosstalk, $\phi_{\xi,i} \neq 0$, shifts the phase position of minimum/maximum threshold.

2.4.4 Time dilation measurement in a doubly tunable resonator

In the early 20th century Einstein published the theory of relativity [66, 67]. The theory about what happens when things move very fast, at speeds comparable to the speed of light. One effect of relativistic motion is that a moving clock ticks slower than a still standing one, this is called time dilation. Thinking about time dilation leads to the twin paradox. Of two twins, one is sent on a space trip in a rocket, while the other one stays on earth. When the travelling twin returns he is suddenly younger than his twin sister. The paradox is found in the fact that constant motion is relative, from both the travellers and the earthbound twins frame, the other twin should have aged less. The paradox is resolved by taking the acceleration of the travelling twin into account. The acceleration
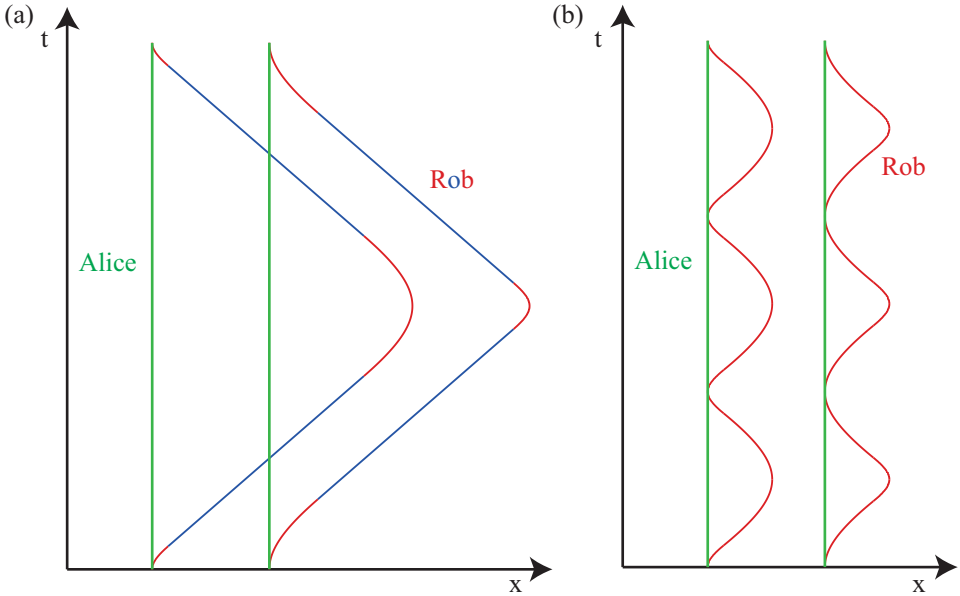
Figure 2.26: *Minkowski spacetime diagrams of the trajectories of the resonator boundary conditions, viewed in the laboratory frame. (a) Trajectories for Rob's resonator that is going on a space trip (red and blue) and Alice resonator that stays on earth (green). The red colour represents segments of constant proper acceleration and blue segments of motion at constant velocity. (b) Trajectory of the resonator boundary conditions for the shaking twin Rob. Note that in both these diagrams the displacement of the boundary conditions are over exaggerated for the cause of readability.*

of the travelling twin breaks the symmetry between the two reference frames.

In Paper D, the translational mode of the doubly tunable resonator system is proposed as a framework for measuring the time dilation of the twin paradox. The idea is that a resonator, loaded with a microwave signal, is sent on a space trip. When it returns after some time, the microwave signal is read out, and compared to a reference signal. Time dilation of the travelling signal would then be manifested by a phase shift. The twins are the observers, Alice and Rob. Alice is staying on earth, *i.e.* stays static in the laboratory frame, while Rob travels to space. His trip starts and ends at rest with respect to Alice. In Fig. 2.26(a) the trajectories of Alice and Rob's resonators are plotted in a Minkowski diagram. The Minkowski diagram is a spacetime diagram where the horizontal axis represents space and the vertical axis time. It is constructed such that a photon travelling in vacuum follows a diagonal through the origin of the diagram. Alice's resonator that stays static on earth does not move on the spacial axis, see the green lines. On the other hand Rob's resonator boundaries move with respect to the laboratory frame, the red colour corresponds to segments of acceleration and blue corresponds to segments of constant velocity. He travels out in space and back home.

The idea of time dilation measurements in a superconducting resonator is quite simple. By flux tuning of the SQUIDs in the resonator ends, the electromagnetic field boundary conditions, a movement of a mirror is mimicked. There is a limited lifetime of the
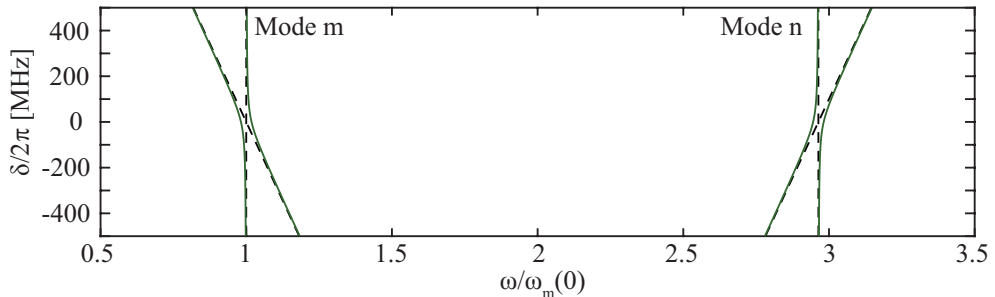
Figure 2.27: *Example of frequency up-conversion from mode n to mode m. The coupling between the modes is stated as an avoided level crossing.*

microwave signal in the resonator. This lifetime decreases when the resonator is detuned from zero flux. Hence, there is a limit on the maximum mimicked displacement of the boundary condition that can be reached, typically corresponding to a couple of millimetres for a resonator lifetime of some microseconds. The displacement should be compared with the resonator length that is around 1 cm. This means that Rob can not travel very far and thus the accumulated phase shift becomes very small. However, the trip can be repeated many times, increasing the possible accumulated phase shift. In practice, Rob would be shaking rather than travelling to Mars, illustrated by the trajectory in Fig. 2.26(b). According to calculations in Paper D, phase shifts larger than 100° are achievable with a shaking resonator.

2.4.5 Parametric frequency up-conversion

Frequency up-conversion is in this thesis used for characterisation purposes. It allows for probing the frequency of modes that are outside the bandwidth of the measurement setup. A weak probe tone is applied to an accessible mode around its resonance frequency, ω_m. At the same time the flux in the SQUID loop is modulated at a frequency close to the difference frequency between mode n and mode m, $\omega_n - \omega_m$, where $\omega_n > \omega_m$. Then parts of the signal is converted from mode m to mode n, which appears as an avoided level crossing, see Fig. 2.27. The resulting frequencies are given by the formulas

$$\omega_{m,\pm} = \omega_m - \delta \pm \sqrt{\epsilon^2 + \delta^2}$$
$$\omega_{n,\pm} = \omega_n + \delta \pm \sqrt{\epsilon^2 + \delta^2}, \tag{2.73}$$

where δ is the detuning given by the frequency diagram in Fig. 2.28, and ϵ is the effective pump strength. Apart from probing modes outside the measurement bandwidth, this could also be used for calibration of the pump strength ϵ.

Frequency up-conversion works well for nonlinear resonators, where the level spacing between the modes is non-equidistant. In the case of an equidistant spectrum the effect also exist, however the pump would address an infinite number of transitions and therefore be very weak for a single transition. This method is also more efficient the closer the
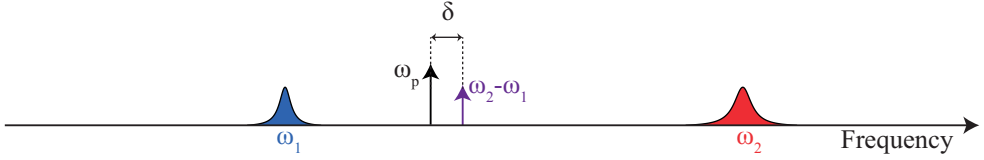
Figure 2.28: *Definition of the detuning in frequency up-conversion when $n = 2$ and $m = 1$.*
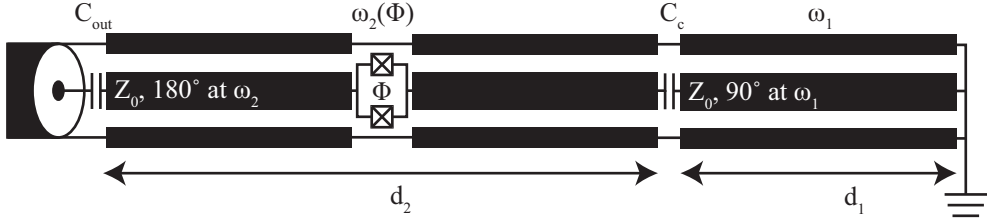
Figure 2.29: *Schematic of the tunable coupler circuit. The coupling between the storage resonator, with the resonance frequency ω_1 and the transmission line on the left is controlled by the tunable coupling resonator, with the flux-tunable resonance frequency $\omega_2(\Phi)$.*

modes are, the coupling between modes is the strongest for neighbouring modes. For further reading see Refs.[22, 23, 68].

2.5 The tunable coupling

In order to create larger quantum networks, one important building block is a tunable coupling - an element allowing information transfer to be turned on and off. Paper E and F presents a system layout with two coupled resonators where one of the resonators is frequency-tunable and can be tuned in and out of resonance with the second one, see Fig. 2.29. In this scheme, the tunable resonator controls the coupling between the storage resonator and the outside world. Searching the literature we find several different layouts for a tunable coupling, for instance using a simple tunable element [69] or for architectures using parametric coupling [70–72].

In our experiment, the two resonators are coupled and form a hybrid system, when probed close to resonance they form an avoided level crossing

$$\omega_\pm = \frac{1}{2}(\omega_1 + \omega_2) \pm \sqrt{g^2 + \left(\frac{\Delta\omega}{2}\right)^2}. \tag{2.74}$$

Here $\Delta\omega = \omega_2 - \omega_1$ and $g = C_c Z_0 (2\omega_1^2 + \omega_2^2)$, the coupling between the resonators, set by the capacitance C_c. The escape rates of the two modes created by the coupled resonances

are given by

$$\Gamma^+_{ext} = \cos^2\left(\frac{\theta}{2}\right)\Gamma_{ext,1} + \sin^2\left(\frac{\theta}{2}\right)\Gamma_{ext,2} \qquad (2.75a)$$

$$\Gamma^-_{ext} = \sin^2\left(\frac{\theta}{2}\right)\Gamma_{ext,1} + \cos^2\left(\frac{\theta}{2}\right)\Gamma_{ext,2}, \qquad (2.75b)$$

where $\theta = \arctan\frac{2g}{\Delta\omega}$. The escape rate of the coupling resonator is

$$\Gamma_{ext,2} = \frac{\kappa}{2} = \frac{1}{\pi}\omega_2(Z_0\omega_2 C_{out})^2$$

given directly by the design of the coupling capacitance C_{out}, while the storage resonator has a residual coupling to the transmission line that is written

$$\Gamma_{ext,1} = \frac{2}{\pi}\frac{\omega_1(Z_0\omega_1 C_c)^2(Z_0\omega_1 C_{out})^2}{1 + (\omega_1 L_{SQ,0}/Z_0)^2}.$$

The relation between the couplings are given by the parameter $\xi = \kappa/4g$. This parameter defines three different regimes. First $\xi < 1$, the underdamped regime. In the underdamped regime, the rate, at which the signal is transferred between the resonators, is larger than the rate, at which it decays to the transmission line. Therefore, the energy has time to oscillate between the resonators before it escapes to the transmission line. For a critically damped system, $\xi = 1$, the energy can be directly released from the storage resonator to the transmission line without any oscillation. In the overdamped system, $\xi > 1$, the coupling between the coupling resonator and the transmission line is stronger than the coupling between the storage and the coupling resonator. Hence, the release of a stored signal to the transmission line is limited by a combination of both couplings, but mainly C_{out}.

Depending on the regime, different types of experiments can be performed using the tunable coupler. In Paper E we present a sample optimised for storage purposes. The storage resonator is loaded with a microwave signal by turning the two resonators on resonance. Thereafter, the coupling resonator is detuned to close the storage, to later be opened by tuning back on resonance and the stored signal can leak out. By choosing the detuning of the resonators, at which the signal is released, the speed and shape of the released signal can be controlled.

In Paper F the focus is, instead of storage of microwave information, on the shaping of a microwave signal. Here, an underdamped system is used. Using a large detuning between the resonators, the coupling resonator can be loaded while the storage resonator stays empty. Then a swap operation can be performed, when the two resonators are tuned on resonance. The microwave signal in the coupling resonator is moved into the empty storage resonator. A second swap operation can be performed to move the signal back to the coupling resonator. The swap protocol allows loading the storage resonator with microwave contents that origin from different frequencies.

3

Experimental methods

For performing the experiments described in the thesis, some engineering techniques are needed. The samples need to be fabricated and connected to a measurement setup. Furthermore, for measurements at milliKelvin temperatures, we need a system that can cool down and stay cold for a longer time. In this chapter I introduce different fabrication methods as well as some cryogenic cooling techniques. I also step through some measurement setups and sample design aspects. This chapter does not contain everything you could know about the different subjects but some of my experiences and learnings.

3.1   Fabrication techniques

The samples have been fabricated in the Nanofabrication Laboratory at Chalmers using standard fabrication methods. In the thesis, different materials and processes have been used and detailed recipes can be found in Appendix A. The substrates used are sapphire and silicon, and the metals niobium and aluminium, with some minor pieces of gold. The following sections present the different fabrication processes.

3.1.1   Substrate pretreatment

For silicon, the most important pretreatment before metal deposition is a dip in Hydrofluoric (HF) acid. The acid removes the native oxide on the surface. However, the oxide is quickly regrown if exposed to air. Therefore, a fast load into vacuum of the deposition system is needed. The silicon oxide hosts two-level fluctuators, and by removing the oxide, losses can be reduced. Further pretreatment can be done by heating the substrate to high temperature, annealing.

The sapphire substrates used in the thesis are c-plane substrates. These are pretreated by annealing at 1050°C in an oxygen/nitrogen atmosphere for some hours. The annealing is done to reduce surface roughness [73].

More extensive cleaning of both silicon and sapphire can be done by solvents to remove organic residues. As you can see in the recipes in Appendix A, three of them contain pretreatment with a solvent cleaning and one does not.

3.1.2 Metal deposition

The superconducting circuits consist of metal. During this thesis two different metal deposition techniques have been used, evaporation and sputtering. Both take place in a high vacuum environment.

Evaporation

An electron gun is pointed towards a metal target which evaporates. This vapour then hits the sample, where the metal condenses and forms a thin film. The thickness of the metal is monitored via a vibrating crystal. During evaporation when the metal thickness increases, the crystal vibration frequency changes. A change which through a calibration can be translated to a metal thickness.

Evaporation with an electron gun is possible for various materials but in this thesis it has been used for aluminium, gold, chromium, titanium and palladium.

Sputtering

In sputtering, atoms of a target metal are physically ejected by bombardment of atoms or ions of a transfer gas. The ejected target atoms are then bombarding the substrate with high energy. By controlling the pressure of the transfer gas, the energy contents of the deposition plasma can be controlled. In this thesis, sputtering has mainly been used for deposition of niobium.

3.1.3 Lithography

For lithography we use polymer mixtures called resists. Different resist types are used for different exposure methods. When exposed, the polymer bindings in the resist are changed. Resist exposure can be done using a mask aligner with a UV-light bulb, a laser beam or electrons. The exposed resist is developed in a matching developer. The developer either dissolves the exposed part of the resist (positive resists) or the unexposed part (negative resists) and a pattern is formed.

Photolithography

The photolithography process is illustrated in Fig. 3.1. UV-light is shined through a mask, defining a pattern in the resist. This is a very fast exposure process for large areas, though resolution and alignment precision is usually limited. The limitation depend on the alignment system and the wavelength of the UV-light. Typical alignment accuracy and minimum feature size of photolithography is of the order of $1\,\mu$m.
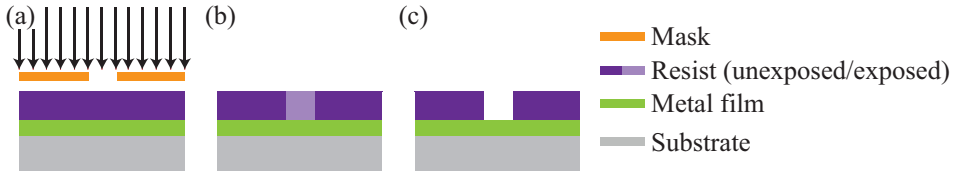
Figure 3.1: *Photolithography. A substrate is covered by photoresist, between the resist and the substrate there could be a metal film or the resist could be spun directly on the substrate. (a) Resist exposure by shining UV-light through a mask. (b) The resist changes properties where it was exposed. (c) A developer resolves and removes the exposed resist while leaving the unexposed unaffected. Hence, a pattern has been defined.*

Laser lithography

In laser lithography, the pattern is written using a laser beam. The precision and resolution is slightly better than photolithography, but there is no dramatic difference. The advantage with laser writing compared to photolithography is that no mask is needed and for developing designs this is convenient. The disadvantage, compared to photolithography, is that the writing time increases.

Electron beam lithography

As the name suggests, electrons are used for exposure of the resist. This method has the highest resolution, with fine tuned calibration, structures down to a few nm can be exposed. However, this is also the slowest lithography method. Since the electron beam is small, it takes long time for it to scan larger areas.

It can also be noted that the substrate needs proper grounding. For substrates that conduct electricity (at room temperature) such as silicon this is not a problem, but for sapphire, which is an insulating substrate, electron beam exposures can be difficult. The electron beam easily causes charging effects due to trapping of electrons if there is no path to ground. Some various interesting results can be found in Appendix C.2.

3.1.4 Patterning

A pattern is defined in the resist by a suitable lithography method. The resist pattern can be transferred to the metal film and form circuits by two different techniques, etching and lift-off.

Etching

The etching process is illustrated in Fig. 3.2. A substrate is covered with a thin film metal using either evaporation or sputtering, and then coated with a resist layer. The resist is exposed using one of the methods described above, and after development the underlying metal layer is exposed. This metal could then be either physically or chemically etched. In physical etching, also called dry etching, the material is etched by bombardment of ions, which physically remove the metal. In chemical etching, also called wet etching, the
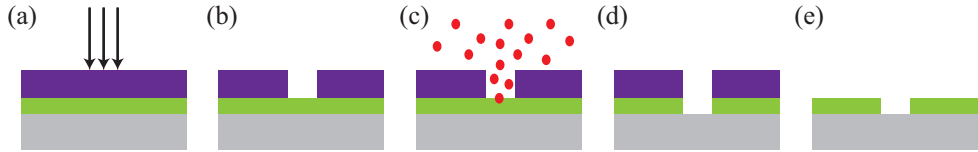
Figure 3.2: *Illustration of an etching process. (a) Resist exposure through a suitable lithography technique. (b) Resist development. (c) Etching, either physical, by bombardment of ions, or chemical, by dipping in a solution that dissolves the material. (d) The metal is patterned. (e) The resist is removed.*
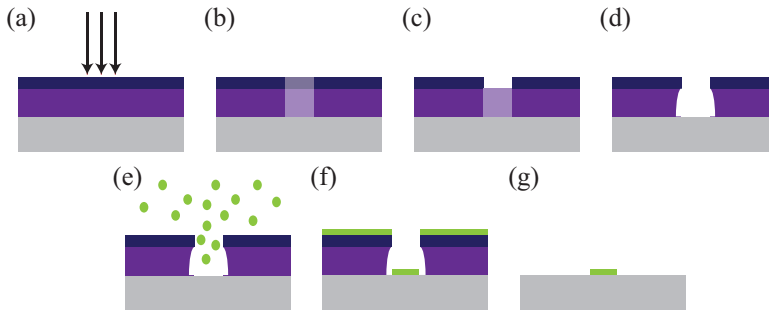
Figure 3.3: *Illustration of a lift-off process. (a) A pattern is exposed using a suitable lithography technique. (b) Both top resist and bottom resist are exposed. (c) Top resist layer development. (d) Bottom resist layer development and a small undercut is created. This undercut is crucial for successful lift-off. (e) Metal is evaporated towards the sample. (f) A thin film of metal is formed on top of the resist and on the substrate. (g) Lift-off, which removes the resist.*

substrate is dipped in a solution that dissolves the metal but preferably does not affect the other parts. An advantage of using etching compared to other patterning techniques is that the interface between metal film and substrate can be properly cleaned before metal deposition. A clean metal-substrate interface has been shown to decrease dielectric losses [43, 74]. To even further reduce the dielectric losses, the substrate in open areas can be etched in order to reduce the electromagnetic field inside the substrate [75, 76].

Lift-off

The lift-off process is illustrated in Fig. 3.3. Two resist layers are placed directly on the substrate. The resists are exposed using one of the methods described above and the resist is developed, either using two different developers for the two layers or using a developer that develops the bottom layer more effectively than the top layer. Note how proper development of the two layers cause an undercut as illustrated in Fig. 3.3(d). Metal is deposited, most commonly through evaporation and due to the undercut there is no risk that the metal sticks to the resist walls. Since sputtering generates heat it could damage the resist and is not optimal for lift-off. After metal deposition, the resist is dissolved in a remover and excess metal is lifted off.

In this thesis, the SQUIDs are fabricated using lift-off and two versions of shadow
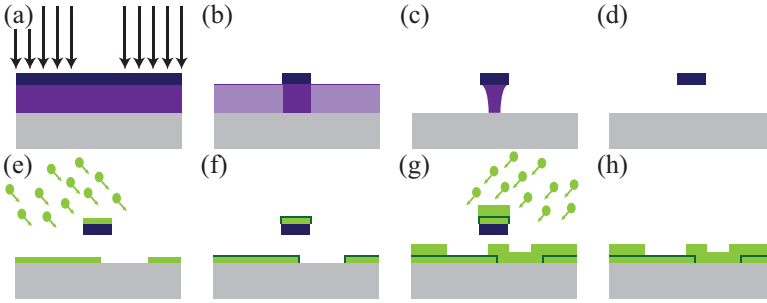
Figure 3.4: *Two angle evaporation, to fabricate junctions. (a) Resist exposure, usually by electron beam lithography, due to resolution requirements. (b) Top layer development. (c) Bottom layer development. (d) The bottom layer is developed until a bridge is formed. (e) Metal is evaporated at an angle and a small strip of the substrate is left bare due to the shadow of the resist bridge. (f) Metal oxidation, the oxide pressure and the oxidation time can be controlled to adjust the thickness of the oxide. (g) Metal is evaporated at a second angle. (h) In the middle a metal-insulator-metal junction is formed.*

evaporation. In the first one, a small resist bridge is created and evaporation is done using two different angles with an oxidation in between, see Fig. 3.4. The second technique is to expose a narrow cross in the resist and then metal is deposited with an oxidation step and a 90° rotation of the mounting panel in between, see Fig. 3.5. In this figure, each panel consist of one illustration of the top view and one side view.

3.2 Cryo cooling

We do our measurements at low temperatures, typically at tens of mK, to access the superconducting regime of our samples. But also to reduce the amount of thermal noise $k_B T \ll \hbar\omega$, *i.e.* to have no thermal excitations. These low temperatures are acquired using a cryostat, a cryogenic refrigerator that can reach very low temperatures. There are different types of cryostats; "wet" cryostats, using a bath of ^{4}He, and "dry" cryostats, using a pulse tube and a compressor. These two basic cooling techniques give a temperature of ~ 4 K. To go lower in temperature we use ^{3}He. For simple test measurements we can use a so-called ^{3}He cryostat. It cools to base temperature using He^3 evaporation and can reach temperatures around 300 mK. Lower temperatures need a mixture of ^{3}He and ^{4}He, which is used in a dilution cryostat, allowing for measurements down to 10 mK.

3.2.1 The ^{3}He cryostat

A schematic of our ^{3}He cryostat can be found in Fig. 3.6. It is a Janis cryostat model He-3-SSV. The inner part of the cryostat, the inner vacuum chamber (IVC) is placed in a ^{4}He bath inside a dewar. Liquid ^{4}He has a boiling temperature of 4.2 K. Hence, a bath of ^{4}He cools the IVC to this temperature. The cryostat then cools in stages with different temperatures and it is of high importance that there is as low thermal contact
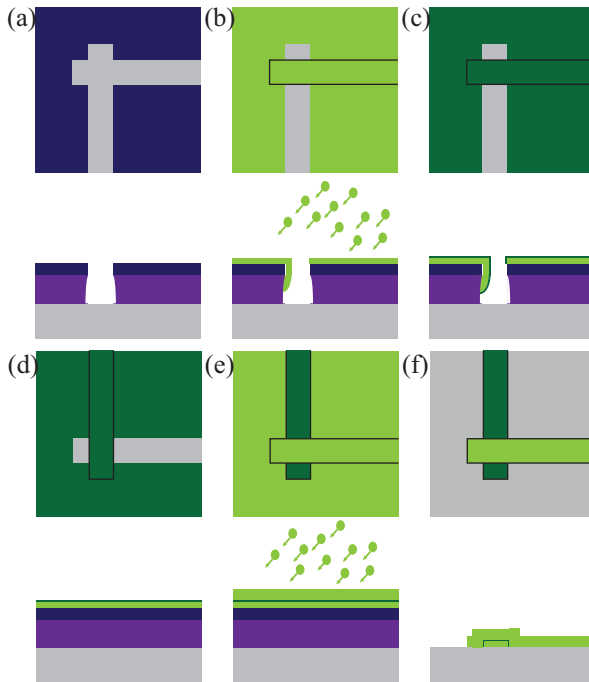
Figure 3.5: *Each panel show both a top view of the structure and a side view. (a) Two layers of resist are exposed and developed. (b) Metal is evaporated at an angle that prevents the perpendicular trench from being filled. (c) Oxidation of the metal. (d) The substrate is rotated 90°. (e) A second metal layer is evaporated. (f) The resist is removed and a junction is formed.*
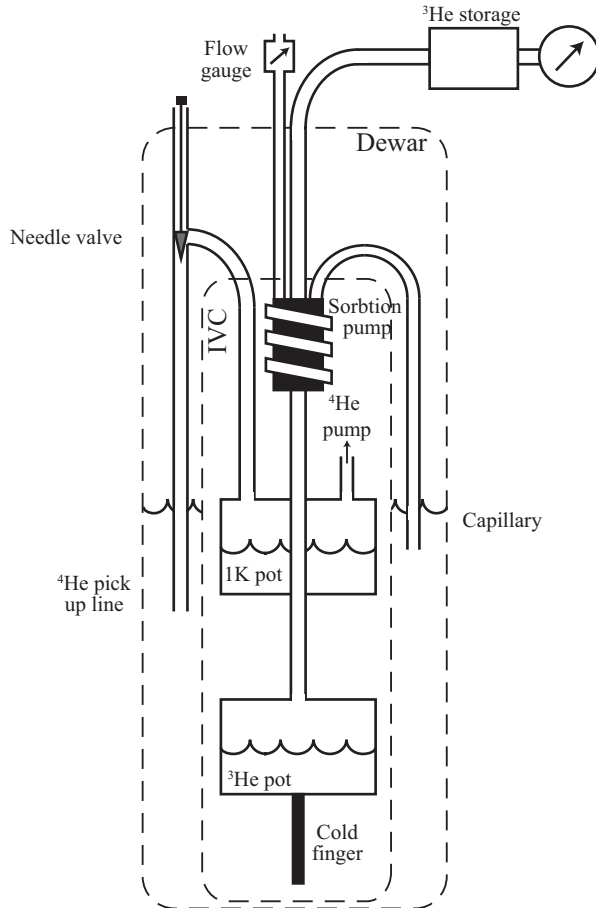
Figure 3.6: *Schematic of our ^{3}He-cryostat.*

between the stages as possible. Therefore, the IVC is kept under vacuum since air would give thermal contact between the outside and the cryostat inside the IVC.

By using the 1 K pot, the temperature can be lowered. A pump is turned on that removes the most energetic (warmest) atoms and the pot is refilled, with a rate controlled by the needle valve position, with liquid ^{4}He from the bath. The purpose of the 1 K-pot is to condense the ^{3}He, which can be done when below ~ 3 K.

The ^{3}He is forced out of its storage by heating the sorbtion pump. Then it is condensed in the 1K-pot and the ^{3}He-pot is filled with liquid ^{3}He. The last step to reach base temperature is to pump on the liquid ^{3}He. This is done by cooling the sorbtion pump, liquid ^{4}He is taken from the bath through a capillary and evaporates through the flow gauge used to control the flow, *i.e.* the cooling power.

After a few minutes, the ^{3}He-pot reaches the base temperature around 300 mK and cools the cold finger where the sample is mounted. The cryostat then stays cold as long as the ^{3}He lasts in the ^{3}He-pot. When the ^{3}He-pot is empty a new condensation must be performed.

3.2.2   The dilution cryostat

A dilution refrigerator uses a mixture of ^{3}He and ^{4}He. When this mixture is cooled below 0.7 K a phase separation occurs. The liquid is divided into two phases, one ^{3}He-concentrated phase and one ^{3}He-poor phase, where the concentrated phase floats on top of the diluted ^{3}He-poor phase. By removal of ^{3}He from the dilute phase, equilibrium is disturbed, and ^{3}He is taken from the concentrated phase to re-establish concentration balance. This process of ^{3}He crossing the phase boundary is endothermic, energy is consumed and the temperature is reduced.

The mixture is condensed using either a ^{4}He-bath and a 1 K-pot, "wet" cryostat, or a pulse tube cryocooler, the more modern "dry" cryostat. For a very thorough explanation of the dilution refrigerator, I recommend reading the thesis of Michaël Simoen [22]. The cryostats used in this thesis were mainly two modern "dry" cryostats (Bluefors LD250). However, also an older "wet" Oxford cryostat, has been used.

3.3   Measurement setup

The measurement setup is composed of commercially available microwave components. Here, I will mainly focus on the setups that have been used in the dry dilution refrigerators, since this is where the main measurements have been performed. In Fig. 3.7 typical input and output lines are presented. On the input line the cables are thermalised at all the different temperature stages. Attenuators are distributed to minimize heating and noise. The cables are thin coaxes, made of silver plated CuNi, which is a bad thermal conductor. The output line consists of a superconducting coaxial cable from the mixing chamber stage all the way to the amplifier. Superconductors have low loss and very poor thermal conductivity, which make them convenient (but expensive) for usage from low to high temperature stages. The amplifiers are high-electron-mobility-transistor (HEMT) amplifiers from the company Low Noise Factory and developed specially for cryogenic use.

Input   Output

- - - - - - - - - - - 300K

- - - - - - - - - 50K

-3dB   0dB

- - - - - - - - - - 3K

-6dB   0dB

HEMT
amplifier

- - - - - - - - - - 800mK

-10dB

- - - - - - - - - 100mK

-20dB

-1dB

- - - - - - - - 10mK
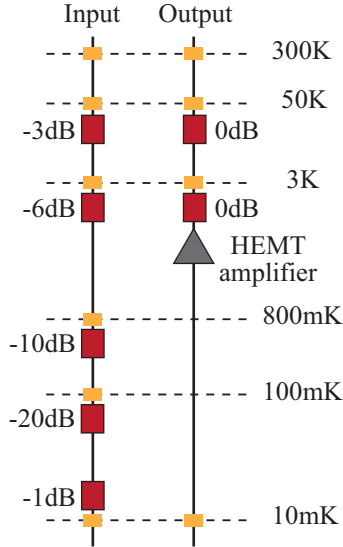
Figure 3.7: *Standard setup in the Bluefors cryostats. The input lines are attenuated to reduce the amount of room temperature radiation and thermalize the signal to the different temperature stages. The output line is low loss and with a HEMT amplifier for amplification of the output signal.*

In this thesis, amplifiers with two different frequency ranges have been used, $4 - 8$ GHz (LNF-LNC4_8A) and $1 - 12$ GHz (LNF-LNC1_12A).

For reflection type measurements, two different setup types have been used, see Fig. 3.8. In (a) the signal is routed through circulators and in (b) through a directional coupler. The signal routing allows the input and output signal to travel different paths, which in turn allows for proper attenuation of the input signal and amplification of the output signal. The microwave components as well as our amplifiers limit the available frequency range for measurements. The circulators are specified only for the $4 - 8$ GHz-band and thereby limits the available frequency range for measurements in a circulator setup. The measurement frequency limit in the isolator setup is set by the isolators that are specified in the $3 - 12$ GHz-range. However, the directional coupler can be more wideband and allow for a higher frequency drive signal.

3.3.1 Magnetic flux control

Static magnetic flux biasing of a single SQUID can be done by using an external coil, mounted close to the sample. For samples with multiple SQUIDs, the biasing is done on-chip, using on-chip flux tuning lines, to allow for individual control. An on-chip flux tuning line is a transmission line, close to the SQUID, that generates a magnetic field, when a current is applied. These can be designed in many different ways, for some examples see Fig. 4.10. A discussion on flux tuning line designs is found in Section 4.2, in the subsection about the doubly tunable resonator.

Figure 3.8: *Two reflection setups where (a) circulators or (b) a directional coupler and isolators are used to route the signal and isolate from amplifier noise. Above the* 10 mK*-stage, the input and output lines are drawn in Fig. 3.7.*

On-chip flux tuning lines are also used for fast modulation of the magnetic flux. For high frequency modulation, the on-chip flux tuning line is connected to a typical input line (Fig. 3.7) and then grounded either on-chip, on the sample holder or capped by a 50 Ω terminator outside the sample box. For a combination of dc and ac signals in the on-chip flux tuning line, a bias-T is used to combine these two at low temperature. If needed, the combined signal can be transported off-chip and a second bias-T can be connected to allow for proper termination of both the ac and dc signal. Typical flux tuning line setups with and without bias-T are sketched in Fig. 3.9.

3.3.2 Sample mounting

The fabricated samples are glued (using Russian BF6-glue) in sample boxes and bonded by aluminium or gold wires, an example is shown in Fig. 3.10. Different types of boxes have been used in the thesis, two designs are shown in Fig. 3.11. Most measurements have been performed using the design in panel (a) and (b), where the bonding is done to a printed circuit board (PCB). However, it was found out that these PCBs cause loss. Therefore my colleges, Andreas Bengtsson and Jonathan Burnett, developed new boxes, panel (c) and (d), where no PCB is used but the sample ground plane is bonded directly to the box and the contact pads are bonded directly to the pins of the SMA-connectors. This design is better from several perspectives, one is the absence of the PCB but also the smaller dimension places possible parasitic box modes at higher frequencies.

3.3.3 Digitizer measurements

We use a digitizer for heterodyne detection of signals, a schematic is sketched in Fig. 3.12. It has an analogue down-conversion step and a digital step that divides the signal into the in- and out-of-phase quadratures. The input signal is down-converted using a mixer. In

Figure 3.9: *(a) Simple setup for high frequency flux modulation. (b) Using a bias-T both dc and ac signals can be combined in the on-chip flux tuning line. (c) If the on-chip flux tuning line is not grounded on-chip, the signal can be be divided back into ac and dc components and terminated properly. Above the* $10\,mK$*-stage the ac lines are identical to the input line in Fig. 3.7. The dc lines are twisted pair wires.*
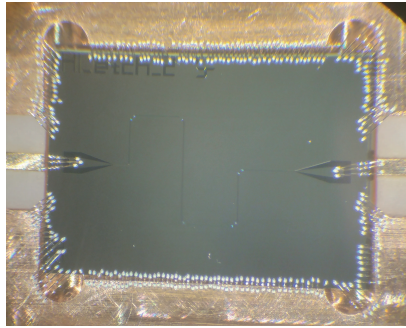
Figure 3.10: *A sample bonded directly to the copper sample box and the centre pin of the connectors.*
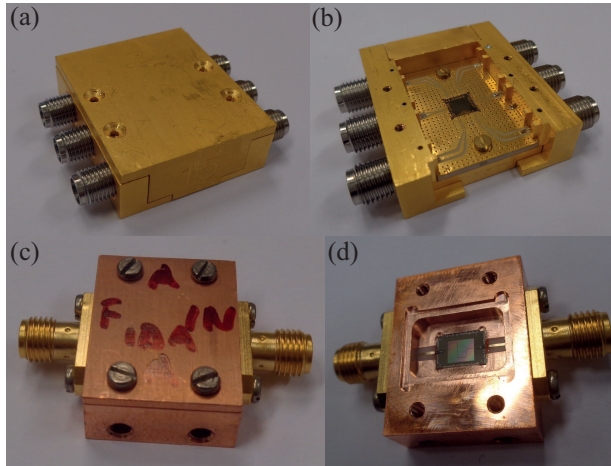
Figure 3.11: *Two types of sample boxes that have been used in this thesis. (a) The outside and (b) inside of an old style sample box using a printed circuit board (PCB). (c) The outside and (d) inside of a newer sample box design. A zoom in on a sample can be found in Fig. 3.10.*
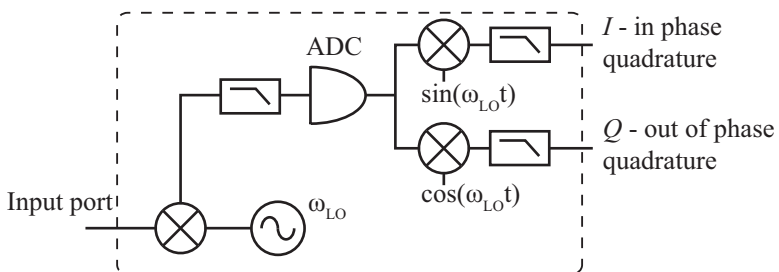
Figure 3.12: *Schematic of a digitizer. The input signal is down-converted using a mixer. Then the signal is low pass filtered and sampled in an analogue to digital converter. Digitally the in- and out-of-phase quadratures are extracted.*
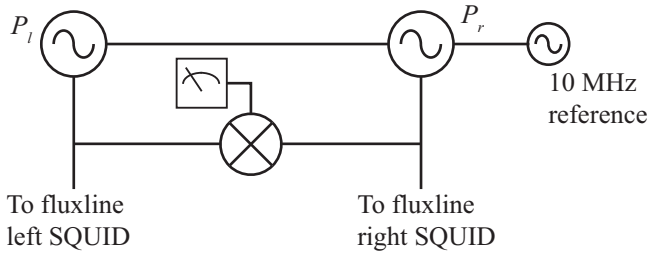
Figure 3.13: *Two separate sources are connected to the same 10 MHz reference signal. The output signals from the sources are split in two parts so that the relative phase of the two output signals can be combined in a mixer and measured by a voltmeter.*

our systems the local oscillator is always set to 187.5 MHz. The mixer outputs both the upper and the lower side band, $\omega_{input} \pm \omega_{LO}$. After the mixer there is a low pass filter to extract the lower side band, $\omega_{input} - \omega_{LO}$. Then the signal is sampled in an analogue to digital converter (ADC). The digitalized signal is then digitally mixed to extract the in- and out-of-phase quadratures. From the quadratures, for instance the total output power can be calculated $P = I^2 + Q^2$.

For a system that switches between different states, such as a subharmonic oscillator or a parametric oscillator, the I and Q quadrature traces show this switching as jumps between signal levels. These traces are used to create a picture of the system phase space distribution. From the traces, histograms are created that clearly show the most populated states of the system. An example of quadrature raw data is shown in Fig. 4.16 and the corresponding histogram is presented in Fig. 4.14(g).

3.3.4 Phase control for double pumping

For double pumping of the doubly tunable resonator, two separate signal sources are used. The setup is described in paper B, but as a complement I also describe it here. The two microwave sources are always set to the same frequency, however their relative phase is randomly set each time the frequency is changed. Therefore, I continuously measure the relative phase of the sources to allow for post-processing of the datasets.

The output signals of the two microwave sources are split in power splitters and one part goes to the on-chip flux tuning lines and the other to a microwave mixer, see Fig. 3.13. Since the two sources always are set to the same frequency, the mixing output is a dc component, that is measured with a multimeter. This dc component is proportional to $\cos(\phi_l - \phi_r)$, where ϕ_l and ϕ_r are the phases of the two signals at the mixer inputs. This phase difference is in turn related to the actual phase difference of the flux pumps at the sample. This allows for post correction of the phase in the data.

3.4 Circuit design

There are many aspects to consider when designing a circuit, choose dimensions of the coplanar waveguide, set the strength of the coupling capacitor and dimensions of
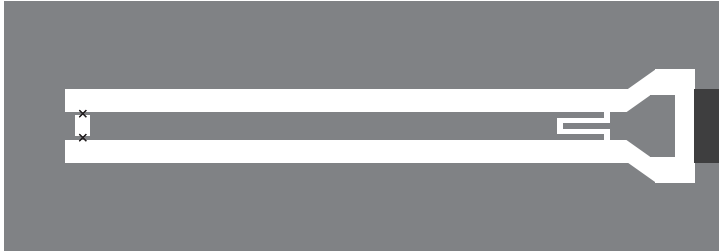
Figure 3.14: *Simplified version of a typical layout of a SQUID-terminated λ/4-resonator. To the left is the SQUID and to the right is the coupling capacitor with a metal piece behind, intended for bonding to a contact. The darker piece of metal behind the bonding pad could be left and create a huge superconducting loop. Or it could be removed and there would be no loop.*

the SQUID-loop and junctions. Here I will focus on two design aspects of the circuit environment where I have gained some experience from my particular experiments.

3.4.1 Design aspects of superconducting loops

An interesting question when designing a circuit is whether to connect the ground planes behind the contact pads or not. Due to the Meissner effect, magnetic flux is expelled from the area covered by superconducting material. In Fig. 3.14, I present a typical layout of a coplanar waveguide λ/4-resonator with a SQUID at the end (schematic in Fig. 2.9(b)). To the right you find the coupling capacitor and to the right of that, a piece of conductor intended for bonding, a contact pad.

To the right of the contact pad, a piece of ground plane is marked with a darker grey colour. This piece of superconductor creates a large superconducting loop. Due to the Meissner effect magnetic flux can be trapped in superconducting loops, causing noise. The larger the area of the loop, the larger the risk of trapping flux. However, a circuit embedded in a superconducting loop is also protected from external field fluctuations. An advantage with keeping the dark grey piece is that the ground plane pieces on the two sides of the resonator are better connected.

The best solution remains unknown. For other people in the group, leaving the dark piece has worked very well. However, for me there has been indications that this huge superconducting loop leads to flux noise. In Appendix B.2, two test measurements on the same design with and without a superconducting connection behind the contact pads have been tried. Both samples are measured in the same setup, with the same type of magnetic shielding. The results show that the superconducting loop indeed shields the resonator and makes it less sensitive to external magnetic fields. However, the resonance frequency measured with the shielding dark piece of ground plane is very noisy. On the other hand, when the superconducting loop is cut, the resonance frequency measured is very stable. Therefore, I avoid superconducting loops as much as I can.

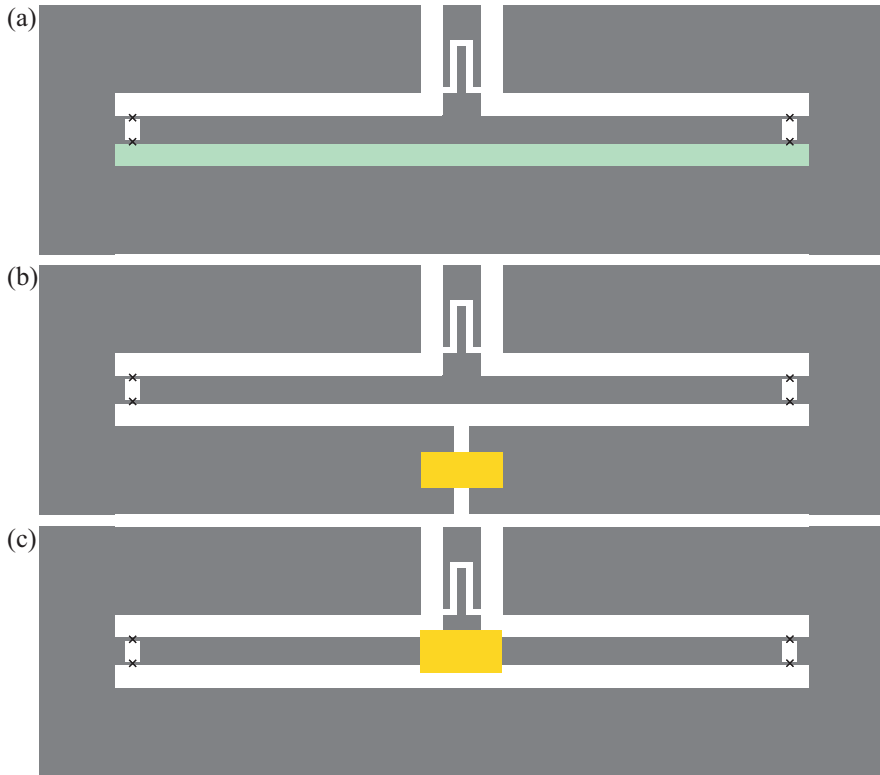Figure 3.15: *Layouts of doubly tunable resonator designs. (a) The straight forward layout we get from the schematic in Fig. 2.12. (b) The design used for the main measurements where the superconducting ground plane is cut and connected with gold to ensure good electrical contact. (c) Another version of using a gold connection to break the parasitic superconducting loop is to have a piece of gold in the middle of the resonator.*

3.4.2 Design aspects of the doubly tunable resonator

A direct translation of the schematic in Fig. 2.12 gives the layout of Fig. 3.15(a). Note here how, if nothing is done, on the lower side of the resonator, there is an extra SQUID loop with a large area. The loop is formed by the resonator centre conductor and the ground plane and marked with a light green colour. Compared to the SQUID loops this parasitic loop is huge and is also a SQUID loop. To solve the problem, the ground plane is cut in two and bridged with gold, see panel (b). The purpose of the gold is to ensure good electrical contact throughout the full ground plane, however since gold remains a normal conductor also at low temperatures the remaining loop is not superconducting and does not trap flux. In panel (c) you find a second version of breaking the parasitic superconducting loop. Here the superconductivity is broken in the middle of the resonator. Since gold is a normal metal this can induce some losses, however for the first resonator mode, there is a current minima in the middle of the resonator. Minimal current means that the losses should be small.

Even though the loop is not superconducting there remains a loop through the resonator and the lower part of the ground plane. This loop is big and could potentially inductively couple to other structures on-chip or in the sample box.

4

Results

Here I present measurement results from several different samples. The key findings are presented in the papers which are attached at the end of this thesis. However, in the thesis I extend the picture by presenting results from more samples and bias points. There will be some analysis and discussion on different implications. I start with characterization of resonators and continue with fast modulation of the SQUID nonlinearity. The characterization is done on samples without SQUIDs as well as single-SQUID and double-SQUID tunable resonators. For the doubly tunable resonator, I discuss different designs, loss mechanisms and dc crosstalk. In the fast modulation section, I present measurement results that are extensions of the Paper A and B contents on different types of period multiplication subharmonic oscillations. In section 4.3.5, additional information on the doubly tunable resonator that supports the claims in Paper C are presented. In section 4.4 I do a short review of the results of Paper E and F on microwave manipulation in a tunable coupling system.

4.1 Resonator characterization

Characterisation measurements are done using a vector network analyser (VNA) in reflection setups, see Fig. 3.8. The measured data consist of both magnitude and phase of the reflection coefficient as a function of frequency. Fitting the resonance with Eq. (2.20) allows for extraction of Q-values and resonance frequency.

4.1.1 Linear resonator

The linear resonator is a plain transmission line resonator without any SQUID, *i.e.* without any nonlinearity. The sample I show data from is a $\lambda/2$-resonator, with the design presented in Fig. 3.15(a), but with continuous metal instead of SQUIDs. It is a niobium resonator on a silicon substrate, fabricated using the recipe in appendix A.4. The measurements were performed in our ^{3}He cryostat at roughly $300\,\mathrm{mK}$.

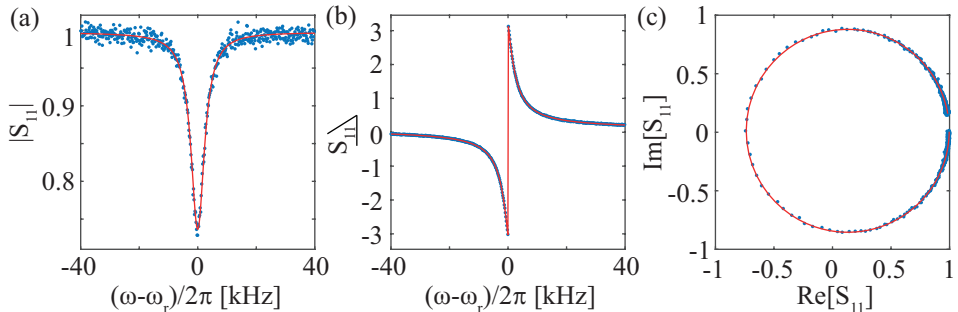The raw data of a reflection measurement is presented in Fig. 4.1 as blue dots. The

Figure 4.1: *An example of a resonance data trace (blue dots) with corresponding fit (red line). This specific one is for a probe power of −117 dBm, the extracted resonant frequency and Q-values are $\omega_r/(2\pi) = 4.9796\ GHz$, $Q_{ext} = 9.4 \cdot 10^4$ and $Q_{tot} = 8.2 \cdot 10^4$. In (a) and (b) you find the magnitude and the phase of the reflection coefficient. (c) The reflection coefficient plotted in the polar plane.*
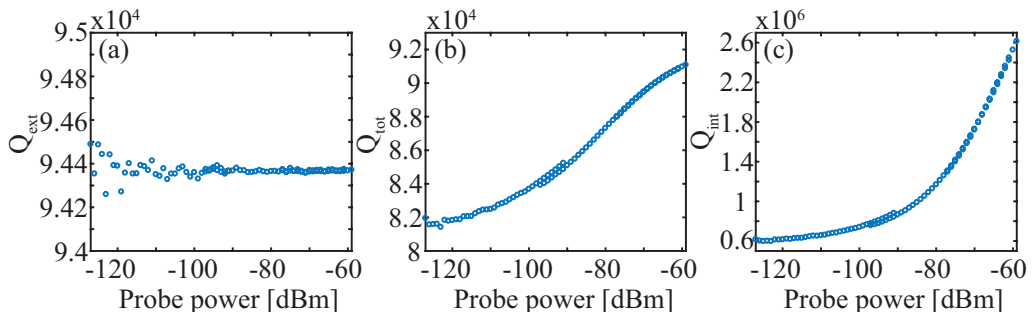
Figure 4.2: *Probe power dependence of the quality factors. (a) External quality factor. (b) Total quality factor. (c)Internal quality factor. The increase with larger probe power indicates that one of the dominating loss factors could be two level fluctuators.*

different panels show (a) the magnitude response, (b) the phase response and (c) a polar plot of the real and imaginary parts of the reflection coefficient. Here some processing of the data has been done, the background has been normalised to ensure that $|S_{11}| = 1$ far from resonance and the electrical delay in the measurement setup has been compensated. The extracted resonance frequency and Q-values at low power are $\omega_r/(2\pi) = 4.9796\ \mathrm{GHz}$, $Q_{ext} = 9.4 \cdot 10^4$ and $Q_{tot} = 8.2 \cdot 10^4$. The internal Q-value is calculated using Eq. (2.12) to $Q_{int} = 6.3 \cdot 10^5$.

The data in Fig. 4.1 represent a probe power of −117 dBm. In Fig. 4.2, extracted Q-values are presented for many different probe power values. The power scale spans from single photon level up to millions of photons. As seen, the total Q-value increases with the probe power while the external Q-values remains the same, which means that the internal Q-value also is increasing with probe power. This is a signature that the main loss mechanism is the two-level fluctuators in the substrate [42, 77]. At larger probe power, the two-level fluctuators are saturated and interact less with the resonator and

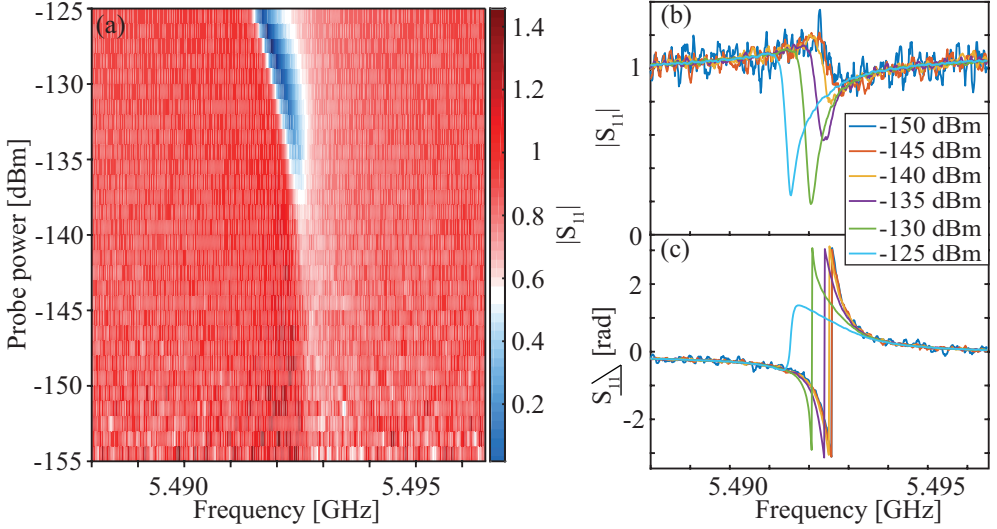Figure 4.3: *Reflection measurement on a SQUID-terminated $\lambda/4$-resonator biased close to zero flux. (a) Magnitude response versus probe power. (b) Linecuts from the magnitude response. (c) Linecuts from the corresponding phase response.*

cause less loss.

4.1.2 Resonator with a nonlinear element

In a reflection measurement, the resonator with a nonlinear element behaves just as a plain linear resonator, for low probe power. However, when the probe power is increased, the nonlinearity affects the response. The nonlinear elements treated in this thesis are, either a single Josephson junction or two Josephson junctions in parallel, a SQUID. By low probe power I assume a probe power that generates a current well below the critical current of the Josephson junction(s).

As an example of nonlinear effects, I show data from a $\lambda/4$-resonator terminated with a SQUID, Fig. 2.9(b), made of aluminium on a silicon substrate, sample #3 in table 4.1. For zero flux bias, the magnitude response is plotted versus probe power in Fig. 4.3(a). The reflection measurement is performed using a VNA. Linecuts of the magnitude response are plotted in (b), together with the corresponding phase traces in (c). For low probe power, $\lesssim -140$ dBm, the magnitude response is barely noticeable. Together with the fact that the phase does a 2π-wrap this indicates an overcoupled resonator. Ideally, the magnitude response would be a dip or just flat, however there is a S-shape. This S-shape is probably due to an impedance mismatch between the transmission line and the resonator. Above -140 dBm the depth of the magnitude response starts to grow. At larger probe power the dip appears even deeper and also shifted towards red (negative) detuning. Also, the phase response shows an asymmetric behaviour for the larger probe power values. This asymmetry is due to the bifurcation described in section 2.3.2. When the probe power is increased, the photon population in the resonator increases, and the generated current in
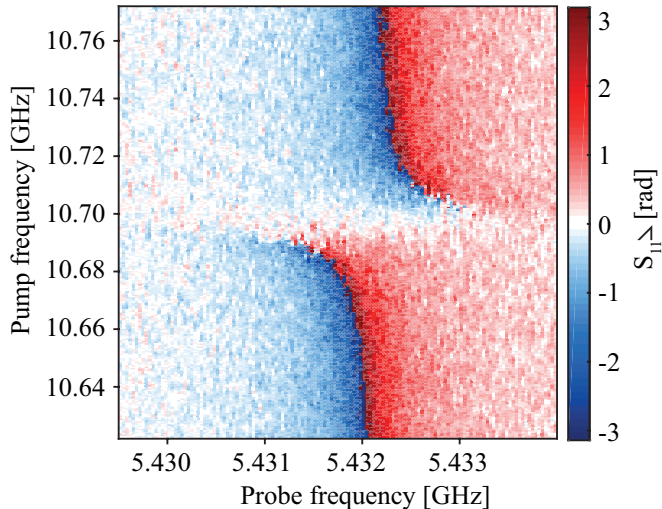
Figure 4.4: *Example of an avoided level crossing from which we can extract the difference $\omega_2 - \omega_1$. From the horizontal axis we find the frequency of the first mode, $\omega_1/2\pi = 5.432\ GHz$. The pump frequency at which the avoided level crossing appears indicate the difference $(\omega_2 - \omega_1)/2\pi = 10.70\ GHz$, yielding $\omega_2/2\pi = 16.132\ GHz$.*

the resonator becomes comparable to the SQUID critical current. The resonance shifts and the measured reflection coefficient no longer gives the full information about the resonance since it can only measure one of the branches at a time.

4.1.3 Measurements of modes outside the available measurement band

To explore the resonator spectrum outside the setup measurement band, parametric up-conversion can be used, see section 2.4.5. A weak probe signal is applied to one of the measurable resonator modes, at the same time as we fluxpump the SQUID at the difference frequency between the measurement mode and another resonator mode, photon conversion between the modes is detected as an avoided level crossing [68]. The probe signal is applied to the input port of the reflection setup, while the flux pump is applied through an on-chip flux pump line. The probe mode frequency is known and then the difference frequency between the modes can be extracted. Hence, the wanted mode frequency is simply $\omega_p + \omega_1 = \omega_2$. A measurement example is shown in Fig. 4.4. The data is taken from a SQUID-terminated $\lambda/4$-resonator, Fig. 2.9(b). It is the same example as presented in Paper A.
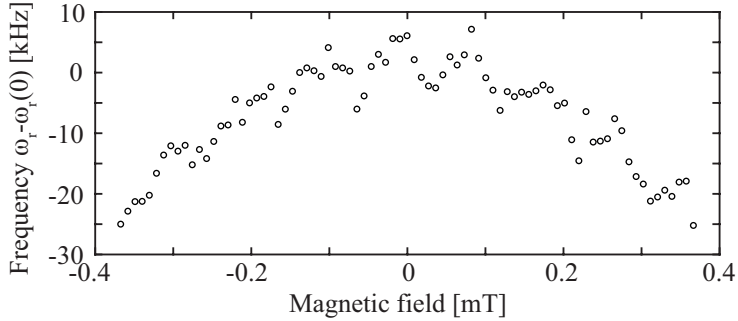
Figure 4.5: *A minor effect of magnetic field can be found in a plain niobium resonator without a SQUID.*

4.2 Static biasing of a tunable resonator

By sweeping the applied flux bias of the samples, the resonance frequency dependence on magnetic flux can be explored. Depending on the resonator design, different behaviour is expected.

Firstly, as a reference, Fig. 4.5 shows the frequency tuning of a plain niobium $\lambda/4$-resonator without any SQUID, solely a transmission line of niobium. To first order, a plain resonator should not show any flux dependence. Nevertheless, there is a small shift in resonance frequency in Fig 4.5, we attribute this to a modification of the kinetic inductance of the resonator. It should however be noted, that the measured resonance shift is of the order of kHz while the resonance frequency is around 5 GHz. The magnetic field strength is calibrated by a SQUID-tunable resonator placed on the same chip. The measurement was performed in a dilution cryostat at 10 mK.

Another resonator type, that should not be sensitive to magnetic fields, is a $\lambda/4$-resonator terminated by a single Josephson junction. The sample under study is a niobium resonator with aluminium SQUIDs and measurements were performed at 10 mK. Interestingly, the measurement results show that the resonance frequency is sensitive to magnetic flux, see Fig. 4.6. Again, the magnetic field strength is calibrated using a SQUID-tunable resonator placed on the same chip. Compared to the plain resonator, Fig. 4.5, the effect is large however still small compared to the resonance frequency that is around 5 GHz. This magnetic field sensitivity could possibly be explained by flux penetrating into the junctions, reducing the Josephson inductance. The larger jumps at 0.22 and 0.3 mT also indicate that there was some rearrangement of trapped flux close to the junction.

4.2.1 Quarter wave-length SQUID-terminated resonators

Here I will show measurement data from some different $\lambda/4$-resonators, see schematic in Fig. 2.9(b). Most of them have nominally symmetric SQUIDs while one sample has an asymmetric SQUID. The spectra for these resonators are given by the dispersion relation in Eq. (2.28), however for the case of an asymmetric SQUID the inductive term has to
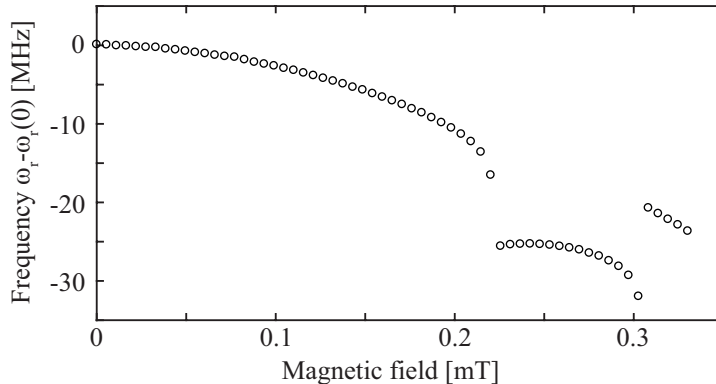
69

Figure 4.6: *Magnetic flux sensitvity of a resonator terminated by a single Josephson junction.*

be rewritten accordingly. The first resonator mode is always probed directly through a reflection measurement. For one sample, the second mode is also directly probed while the other samples required second mode extraction through frequency up-conversion, as described in section 2.4.5.

Symmetric SQUID

For a symmetric SQUID, the inductance is given in Eq. (2.9), this is the case assumed in the dispersion relation, Eq. (2.28). In Fig. 4.7, the data and corresponding fits of three different samples are shown. Extracted parameters of the samples are given in Table 4.1. Sample #1 is the same as presented in Paper A and sample #2 is very similar to #1, only minor differences in resonator length and junction design, which results in different participation ratios. Both these samples are fabricated using the recipe in section A.1 and have their lowest mode placed around 5 GHz. This means that the second mode is around 15 GHz and thereby outside the available measurement band (maximum $3 - 12$ GHz). Hence, the data points for the second mode on these samples are measured by parametric frequency up-conversion. Sample #3, on the other hand, is designed to allow for direct measurements of both the first and the second mode. This sample is fabricated using recipe A.2. Then there is a fourth sample. This sample is fabricated with the same recipe as #1 and #2 and the design is very similar apart from the fact that resonator #4 is longer to have a lower resonance frequency. In this sample the second mode is below 12 GHz and can be directly probed in our measurement setup. The data has not been fitted, hence the lack of extracted parameters in the table.

The nonlinearity of the SQUID gives rise to a non-equidistant resonator spectrum. The modes have different separation. For the fits in Fig. 4.7 the anharmonicity, $3\omega_1 - \omega_2$ is plotted in Fig. 4.8. Here, both sample #1 and #2 behave very similar, starting at some positive value at zero flux, and then cross zero at larger flux bias. In contrast, sample #3 starts at negative anharmonicity at zero flux, and stays below zero for the full flux period. The reason for the difference in anharmonicity sign is found in the junction design. Compared to sample #1 and #2, the junctions in sample #3 have very small metal layer
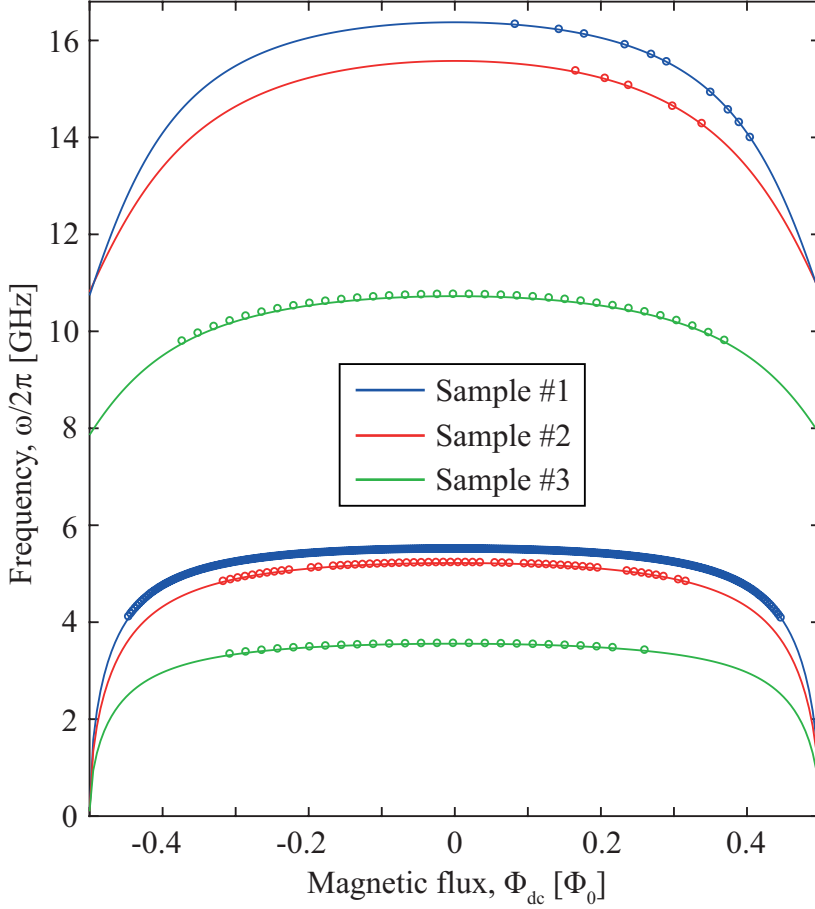
70

Figure 4.7: *The two first modes of three different samples. The dots correspond to data points and the lines are the best found fits. Specifications of the different samples are found in Table 4.1.*

Table 4.1: Specification of the $\lambda/4$ SQUID-tunable resonators presented in this thesis. Sample $\#1-4$ have symmetric SQUIDs while sample $\#5$ have an asymmetric SQUID. The properties stated in the table are, appendix reference to the recipe used for fabrication, the resonator length, d, the zero flux resonance frequency $\omega_1(0)$, the SQUID critical current, I_c (for sample $\#5$ that has an asymmetric SQUID the critical current of the respective junctions are given), the SQUID capacitance, C_{SQ}, the inductive participation ratio, γ_0, the inductance and capacitance per unit length, L_0 and C_0, the spectrum anharmonicity at zero flux, $3\omega_1(0) - \omega_2(0)$, the linewidth, $2\Gamma_1$ and the Q-values, $Q_{ext,1}$ and $Q_{tot,1}$.

Sample	#1	#2	#3	#4	#5
Fabrication recipe	A.1	A.1	A.2	A.1	A.1
d [mm]	5.1	5.2	7.9	6.8	5.1
$\omega_1(0)/2\pi$ [GHz]	5.504	5.225	3.557	4.035	5.244
I_c [μA]	1.90	1.47	0.85		1.05/0.31
C_{SQ} [fF]	86	63	~ 25		230
γ_0 [%]	7.7	10.7	10.6		11.5
L_0 [μH/m]	0.44	0.41	0.45		0.41
C_0 [nF/m]	0.16	0.17	0.14		0.17
$(3\omega_1(0) - \omega_2(0))/2\pi$ [MHz]	136	86	-56	21	
$2\Gamma_1(0)$ [MHz]	0.38	0.49	0.12		
$Q_{ext,1}(0)$ [10^3]	19	11.4	33.8		
$Q_{tot,1}(0)$ [10^3]	14.5	10.7	29.4		

overlaps and thinner oxide layer. This results in similar values for SQUID inductance, however the capacitance becomes small, due to the small overlaps. The capacitance is very small also compared to the geometric capacitance of the resonator, which is larger for sample #3 simply because the resonator is longer. Therefore, it is difficult to extract a number, a simple comparison of the junction area gives that sample #3 have roughly 40 % of the junction area of sample #2. That correspond to roughly a capacitance of 25 fF for sample #3.

Asymmetric SQUID

For an asymmetric SQUID, the inductance is given by the more complicated expression, Eq. (2.8). Hence, the inductive term in the dispersion relation, Eq. (2.28) needs to be replaced. The dispersion relation for the asymmetric SQUID is written as

$$k_n d \tan k_n d = \frac{1}{\gamma_0} \sqrt{\cos^2 \frac{\Phi\pi}{\Phi_0} + \left(\frac{\Delta I_c}{I_c}\right)^2 \sin^2 \frac{\Phi\pi}{\Phi_0}} - c(k_n d)^2. \tag{4.1}$$

In Fig. 4.9, I present resonance data extracted from sample #5. The sample is very similar to the symmetric SQUID samples #1 and #2. The difference is that this resonator has an asymmetric SQUID, $I_{c,1} \neq I_{c,2}$. Furthermore, the asymmetric SQUID gives a minimum on the tuning curve set by the difference between the critical currents of the two junctions, while the maximum on the tuning curve is set by the sum of the junction critical currents. The red line corresponds to the best fit found using Eq. (4.1).
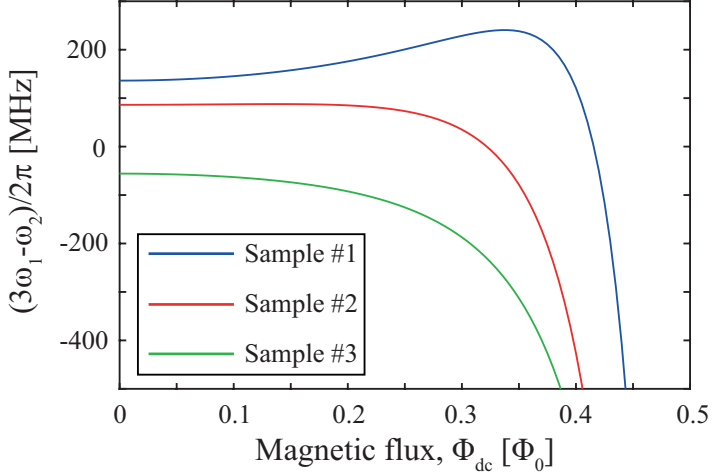
Figure 4.8: *Spectrum anharmonicity, extracted from the fits in Fig. 4.7 for the three samples. Note how sample #3, in contrast with the other samples, has a negative anharmonicity for all flux values.*
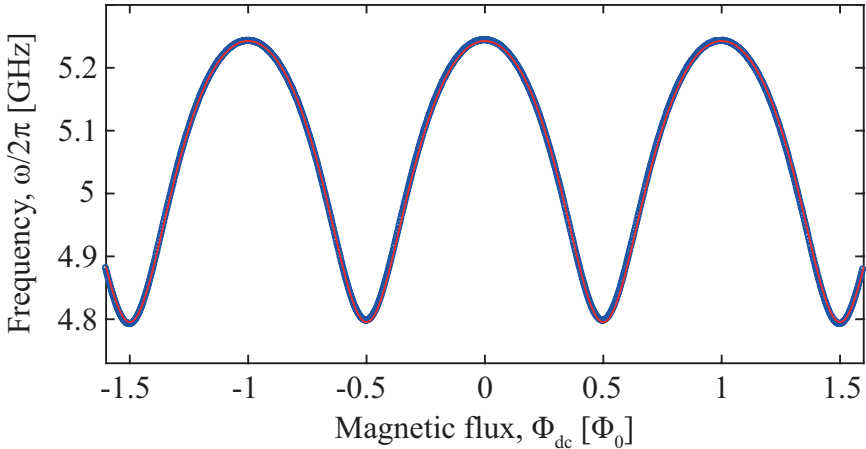
Figure 4.9: *Static tuning of the resonance frequency for sample #5 which has an asymmetric SQUID. Note how the resonance frequency has a minimum (set by the difference between the critical currents of the two junctions). The red line is calculated using the parameters $I_{c,1} = 1.05\,\mu A$, $I_{c,2} = 0.31\,\mu A$, $C_{SQ} = 230\,fF$, $L_0 = 0.41\,\mu H/m$, $C_0 = 0.17\,nF/m$.*

73
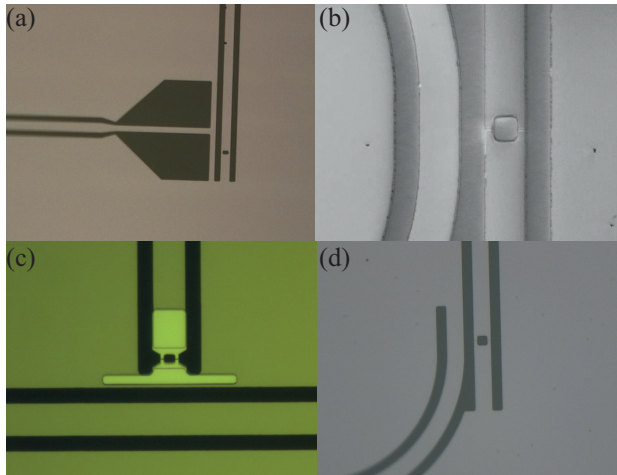
Figure 4.10: *Three different on-chip flux tuning line designs. (a) The flux tuning line splits in two lines with current in opposite directions and therefore opposite inductive coupling to the resonator. (b) The flux tuning line is a transmission line parallel to the resonator with no ground plane in between. A variation of this design can also be created where the flux tuning line is grounded on chip close to the SQUID. (c) Here, the flux tuning line is perpendicular instead of parallel to the resonator. (d) Design very similar to panel (b) but here the flux tuning line is grounded on-chip.*

4.2.2 The doubly tunable resonator

In the double SQUID resonator we would like the two SQUIDs to be controlled independently, to have the tuning pattern as in Fig. 2.13. Therefore we use on-chip flux tuning lines, one for each SQUID. A brief overview and discussion on flux tuning lines can be found in section 3.3.1.

Preferably an on-chip tuning line should give a strong mutual inductance between the SQUID and itself but a minimal coupling directly to the resonator. In addition, for the double SQUID resonator, the mutual inductance should be strong between a SQUID and its own dedicated flux tuning line, but weak between a flux tuning line and the opposite SQUID. Aiming for larger quantum networks, crosstalk is a highly important issue. Here follow some of my experiences, working with the doubly tunable resonator.

For the doubly tunable resonator (DTR) there are several aspects to consider in designing the circuit and the setup, one is discussed in section 3.4.2. Many test measurements of different designs have been performed and here I present some of them. They are represented by the micrographs in Fig. 4.10. These five samples are:

- DTR #1: Flux tuning line design (a). No cut in the ground plane results in a huge parasitic SQUID loop, see Fig. 3.15(a). The sample is made of aluminium on silicon substrate, recipe A.3.

- DTR #2: Flux tuning line design (b). The ground plane is cut by the flux tuning line, hence there is no parasitic SQUID loop. The flux tuning lines are grounded by

bonding from the chip contact pads to the PCB ground plane. The sample is made of aluminium on silicon substrate, recipe A.3.

- DTR #3: Flux tuning line design (a). No parasitic SQUID loop due to gold-filled slot in the resonator middle, see Fig. 3.15(c). The sample is made of niobium with aluminium SQUIDs on a silicon substrate, recipe A.4.

- DTR #4: Flux tuning line design (c). The ground plane has a gold filled slot in the middle, opposite to the coupling capacitor to avoid a parasitic SQUID loop, see Fig. 3.15(b). The flux tuning line is grounded on the PCB ground plane. The sample is made of niobium with aluminium SQUIDs on a sapphire substrate, recipe A.1.

- DTR #5: Flux tuning line design (c), the ground plane has a gold filled slot in the middle, opposite to the coupling capacitor to avoid a parasitic SQUID loop, see Fig. 3.15(b). The flux tuning line continues off-chip and the line is grounded at room temperature. The sample is made of niobium with aluminium SQUIDs on a sapphire substrate, recipe A.1.

The idea with flux tuning line design (a) is that the two perpendicular arms in the flux tuning line end will have opposite inductive coupling to the resonator, so that the parasitic inductive coupling directly between the flux tuning line and resonator is minimal. In design (b) the direct coupling between the flux tuning line and the resonator is large, test measurements show that this coupling severely limits the achievable Q-values. To minimize the parasitic direct coupling, but retain the possibility to lock the current in a closed circuit design, (c) was created. Simply a transmission line perpendicular to the resonator.

Measurement results for the different samples can be found in Fig. 4.11 and 4.12. In the plots of the first figure, horizontal and vertical axes correspond to the current applied to the left and right flux tuning line respectively. The current applied to the flux tuning line scales to applied magnetic flux via the mutual inductance. The resulting flux in the SQUID loop can be written $\Phi_{\mathrm{dc},l/r} = M_{r/l}I_{l/r} + M_{ct,r/l}I_{r/l} + \Phi_{offset,l/r}$, where the mutual inductance between a SQUID and its own flux tuning line is denoted $M_{l/r}$ and the mutual inductance between a SQUID and the remote flux tuning line is $M_{ct,l/r}$. The current applied to the separate flux tuning lines are denoted $I_{l/r}$ and a possible flux offset given from the cooldown conditions is given by $\Phi_{offset,l/r}$.

In Fig. 4.11(a), I present the measurement results from sample DTR #1, the resonance frequency tunes in an elliptic pattern. This is an indication that the crosstalk is large. This could for instance be the current travelling in the ground plane from one side of the resonator to the other one. Though, note how more flux tuning periods are visible in the bottom left and top right corner. Note also that in this sample the parasitic SQUID loop is not broken, which means that the tuning could be different from expected.

A design that both avoids uncontrolled currents in the ground plane and cuts the parasitic superconducting loop is the flux tuning line design in Fig. 4.10(b). As the test measurement on DTR #2 presented in Fig. 4.11(b) shows, this results in very small crosstalk. Furthermore, the same result can be achieved when the flux tuning lines are grounded on chip above the SQUID, see Fig. 4.10(d). Note that in the design tried, the grounding of the flux tuning lines is in a direction where the uncontrolled ground currents
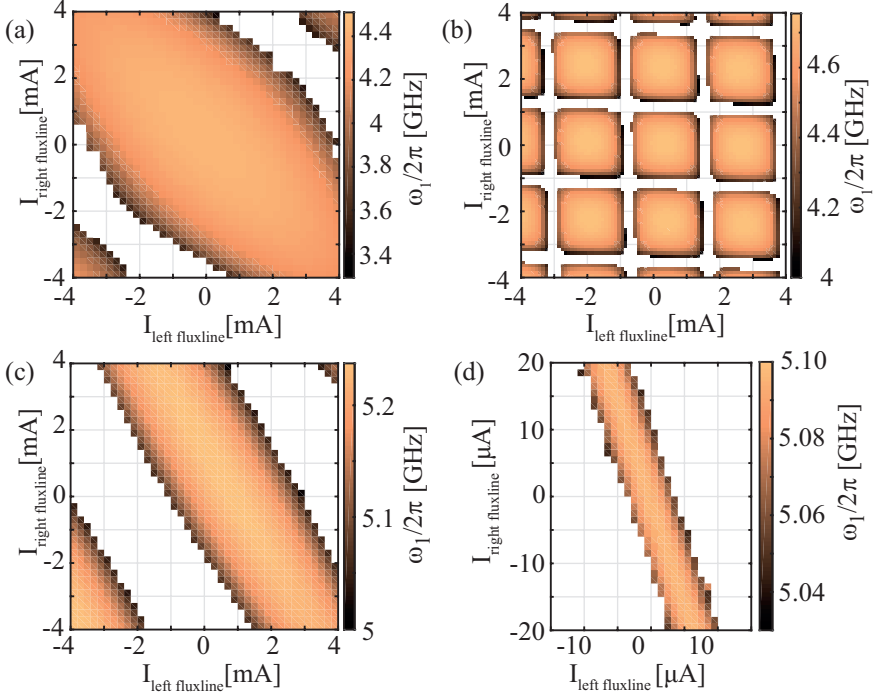
Figure 4.11: *Extracted first mode resonance frequencies, for static biasing of both the left (horizontal axis) and right (vertical axis) SQUID. (a) Sample DTR #1. The measurement show an elliptic shape, which can be interpreted as a signature of the parasitic SQUID loop and/or large crosstalk. (b) Sample DTR #2. The pattern is fairly quadratic which means that the crosstalk is small and there is good individual control of the two SQUIDs. (c) Sample DTR #3. The elliptic shape indicates large crosstalk. The reason for this large crosstalk is unknown. Since there is no parasitic SQUID loop, that should not be the problem. (d) Sample DTR #4. Note how the scale on the current is suddenly micro Ampere instead of milli Ampere. In addition there is no sign of a second flux period. This is an indication that the tuning is rather a saturation of the SQUID critical current than flux tuning.*

Figure 4.12: *Static biasing of a doubly tunable resonator using the flux tuning line design in Fig. 4.10(c). This data is from Paper C and the sample DTR #5. The flux tuning lines continue off-chip and up to room temperature where they are grounded. (a) Static biasing of the first resonator mode. (b) Example line cut from (a) showing the good fit to Eq. (2.33).*
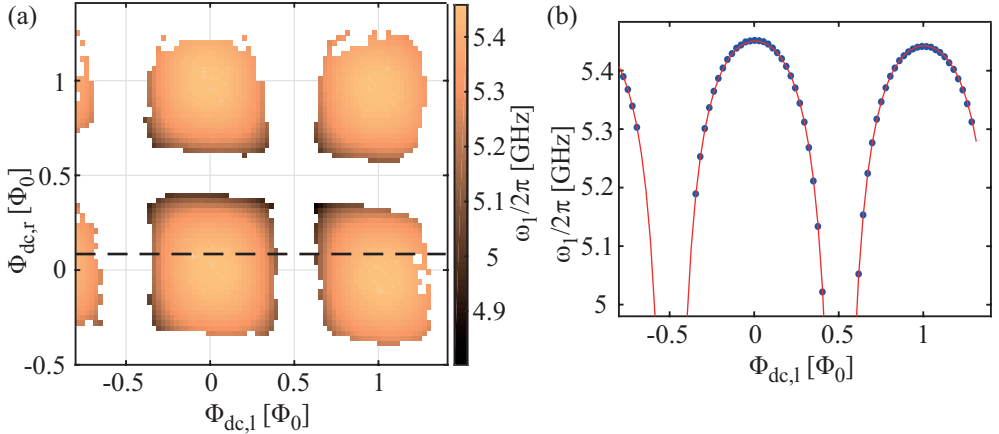
have long paths to reach the remote SQUID. From a crosstalk point of view, this design is a winner. However, from a loss point of view it is bad, test measurements typically show very low internal Q-value due to the direct coupling between the flux tuning line and the resonator.

The sample DTR #3 is special because it has a gold slot in the resonator middle (Fig. 3.15). This cuts the parasitic SQUID loop, but as seen in Fig. 4.11(c), not the crosstalk. Note that there is a second period visible which indicates that the frequency tuning mechanism is indeed flux tuning. The crosstalk could be because of uncontrolled currents in the ground plane that travels from the grounding of one flux tuning line to the other.

To solve the crosstalk problem and also have low loss, the on-chip flux tuning line can be placed perpendicular to the resonator, Fig. 4.10(c). For sample DTR #4, the flux tuning lines continue off-chip and are grounded on the sample box PCB. The measurement result is found in Fig. 4.11(d). In this measurement the SQUIDs can not be controlled individually. Also no second period is visible. Note also that the currents applied on the flux tuning lines are orders of magnitude lower than in the other panels. Micro ampere is of the order of the SQUID critical current. This indicates that the frequency tuning is rather something that saturates the SQUID than tunes it. Likely, the dc current reach the resonator and actually saturates the SQUIDs.

However, if the perpendicular flux tuning line design in Fig. 4.10(c) is used, but the circuit is set up so that the dc current is transported back up to room temperature and grounded there, the SQUIDs can be biased individually, see Fig. 4.12. This is the same sample and figure that are presented in Paper C. In the thesis this sample is known as DTR #5.

One conclusion from all my double SQUID dc-tuning tests is that, to be safe, you

want to transport the current away from the sample and preferably even back to room temperature. Another reflection is that the design in Fig. 4.10(b) is very convenient to use since it removes the need of gold slots to sort out the parasitic SQUID loop. However, as stated above, the coupling directly between the transmission lines causes large losses. A possible solution would be to minimize the part where the flux tuning line and the resonator are parallel, which is not fully done in Fig. 4.10(d).

4.3 Nonadiabatic modulation of a SQUID

As discussed in the theory section there are two methods to modulate the SQUID nonlinearity, either by current driving or by flux pumping. Here I present a larger library of measurement results that did not fit into Papers A, B and C. I start with subharmonic oscillations and continue with a standard parametric oscillator and the doubly tunable resonator.

The power scales in this section correspond to signal generator power subtracted by the installed attenuation. This means that the power scales in principle should be comparable, though it should be remembered that different measurements have been done using different setups and the cable losses may vary.

In order to have subharmonic oscillation excitations rather than SQUID excitations, it is important that the plasma frequency of the SQUID is substantially larger than the drive/pump frequency $\omega_{p,SQ} = 1/\sqrt{L_{SQ}C_{SQ}} \gg \omega_{d/p}$. Given the numbers from the fits in the previous section, the SQUID capacitance is less than $100\,\mathrm{fF}$ and the SQUID inductance around zero flux is of the order of $0.3\,\mathrm{nH}$. Then the SQUID plasma frequency is around $30\,\mathrm{GHz}$. Hence, for third order subharmonic oscillations, the plasma frequency should be at least a factor two larger than the drive frequency at zero flux, assuming a fundamental resonator mode around $5\,\mathrm{GHz}$. For higher order multiples though the drive will be closer to the plasma frequency and possibly interfere. It should also be noted that the plasma frequency decreases with flux which could make the problem larger at larger flux values.

4.3.1 Period tripling subharmonic oscillations

I discovered the subharmonic oscillations while working with a flux pumped doubly tunable resonator, however to reduce the number of unknown parameters, it has been investigated mostly in a current driven $\lambda/4$ SQUID-terminated resonator. In this section I focus on current driving, an external drive signal is applied to the resonator input port, Fig. 2.18. Since theory predicts existence of the oscillations at red detuning, the measurement frequency, ω, is set to sweep from large negative detuning up to around zero. The drive frequency is fixed to 3ω. Starting from the measurement frequency is important here. The measurement frequency can not be set to $1/3$ of the drive since then, for all frequencies not directly dividable by three, there will be rounding errors. Rounding errors cause improper phase matching and effectively a phase drift in the measurement. A figure illustrating this is found in appendix D.1.

The current driven subharmonic oscillations can be detected for many different flux bias values. In Fig. 4.13 I present regions, in which the subharmonic oscillations can be
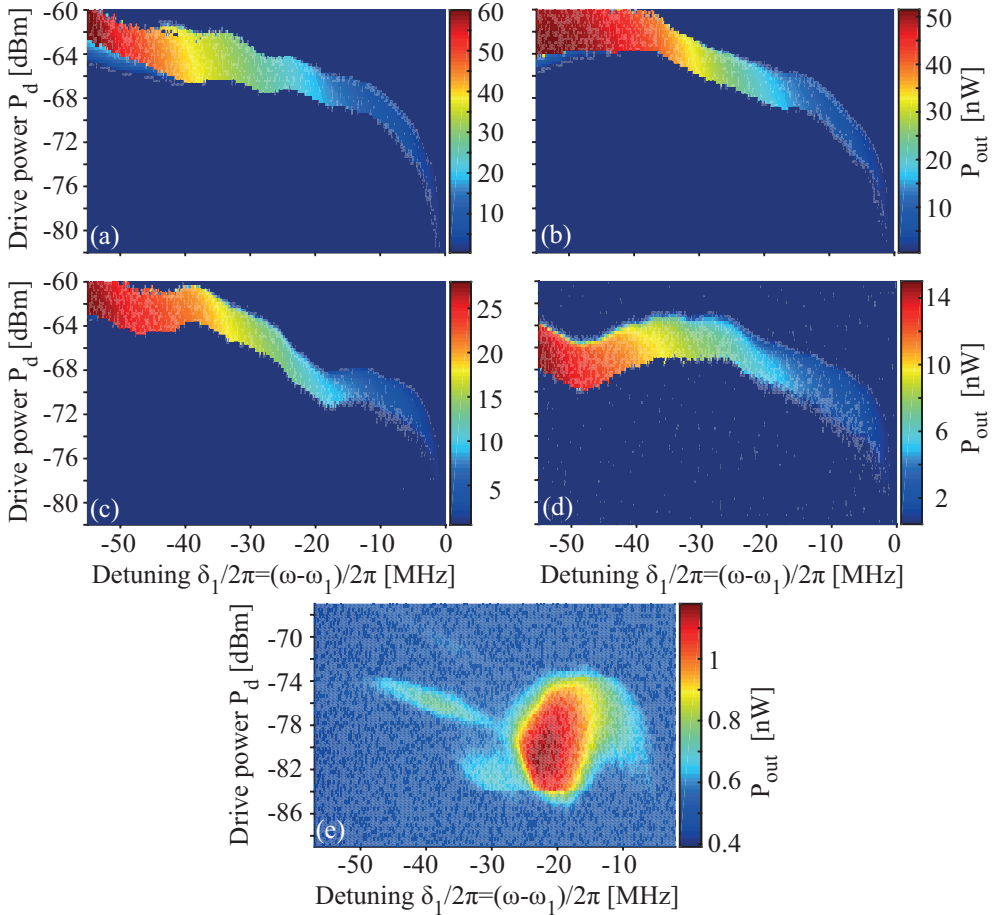
Figure 4.13: *Current driven subharmonic oscillations measured in sample #1, see table 4.1. This is also the same sample as presented in Paper A. The panels correspond to (a) $0\,\Phi_0$, $\omega_1/2\pi = 5.504\,GHz$ (b) $0.1\,\Phi_0$, $\omega_1/2\pi = 5.483\,GHz$ (c) $0.2\,\Phi_0$, $\omega_1/2\pi = 5.409\,GHz$ (d) $0.3\,\Phi_0$, $\omega_1/2\pi = 5.234\,GHz$ (e) $0.4\,\Phi_0$, $\omega_1/2\pi = 4.747\,GHz$. Note that the detuning range is much larger here than in Fig. 4 of Paper A. The measurement temperature was $12\,mK$.*

found, for sample #1 flux biased at 0, 0.1, 0.2, 0.3, and $0.4\,\Phi_0$. For the four first bias points, the regions are fairly similar, they start at some finite red detuning value and persists in a narrow power interval towards larger red detuning. The wavy structure of the regions we attribute to background structures in the measurement setup. The oscillation intensity increases with increased red detuning. However, the larger the flux, the lower the intensity of the oscillations, see the difference in the colour scales. When the flux is increased to $0.4\,\Phi_0$ the subharmonic oscillations are suddenly very weak in intensity and they disappear already at small detuning. Two reasons for this behaviour at large flux are easy to find. First, at this large flux the SQUID critical current is suppressed and the threshold for nonlinear effects is low. Secondly, the anharmonicity of the resonator spectrum is here very small, which decreases the predicted size of the region of existence for the subharmonic oscillations.

In Paper A we present a selection of zero-flux-histograms for sample #1. Here I will show more. For sample #1, more histograms measured at zero flux are found in Fig. 4.14, and they are extracted at the measurement points indicated by the white circles in Fig. 4.15.

In Fig. 4.14(a) the ground state of the system is presented. This is the state, in which I always find the system above and below the subharmonic region. The size of the blob gives a measure of the system noise level. At the lower boundary of the subharmonic oscillation region there is a competition between the ground state in the middle, and the triplet excited state. This can be seen in Fig. 4.14(b,d,f). Also in (j) there is a faint spot in the middle. In the middle of the subharmonic oscillation region, the excited state wins and the histograms show only the triplet state, see Fig. 4.14(c,e,g,h,k). Interestingly, when the detuning is increased, the system starts showing a competition also at the upper region boundary, see Fig. 4.14(l). Also possibly Fig. 4.14(i) could be a mixture of the ground and the excited state, however the limited resolution of the measurement and the low signal level makes it impossible to distinguish whether there are three or four states involved.

The raw data for the histogram in Fig. 4.14(g), the in- and out-of-phase quadratures are presented in Fig. 4.16. However, only for the first 3000 samples. The sampling rate is 100 kHz. Note how the traces switch between three different levels. From these traces, the system switching rate can be extracted by counting the number of switches. For this specific measurement point, the extracted switching rate is around 1 kHz, however the switching rate depends strongly on the exact measurement parameters.

In Fig. 4.17, histograms for sample #1 with flux bias $0.18\,\Phi_0$ are presented. The measurement points are indicated in Fig. 4.18. A comparison of these histograms and the ones of Fig. 4.14 show that the behaviour is very similar for $0.18\,\Phi_0$ compared to zero flux. At the lower boundary, see Fig. 4.17(b,d,g,j), the histograms feature the triplet excited state together with the ground state. However, in (d) and (j) the ground state is very weak. Inside the region of subharmonic oscillations, and at the upper boundary, only the triplet state is visible, see Fig. 4.17(c,e,h,i,k,l). In (i) the measurement point is very close to the upper edge of the subharmonic region, therefore the oscillator intensity is very low and the histograms becomes a triangle. In this figure, I also show a background histogram from above the upper boundary, panel (f). It is found to be very similar to the background level below the subharmonic region, panel (a).
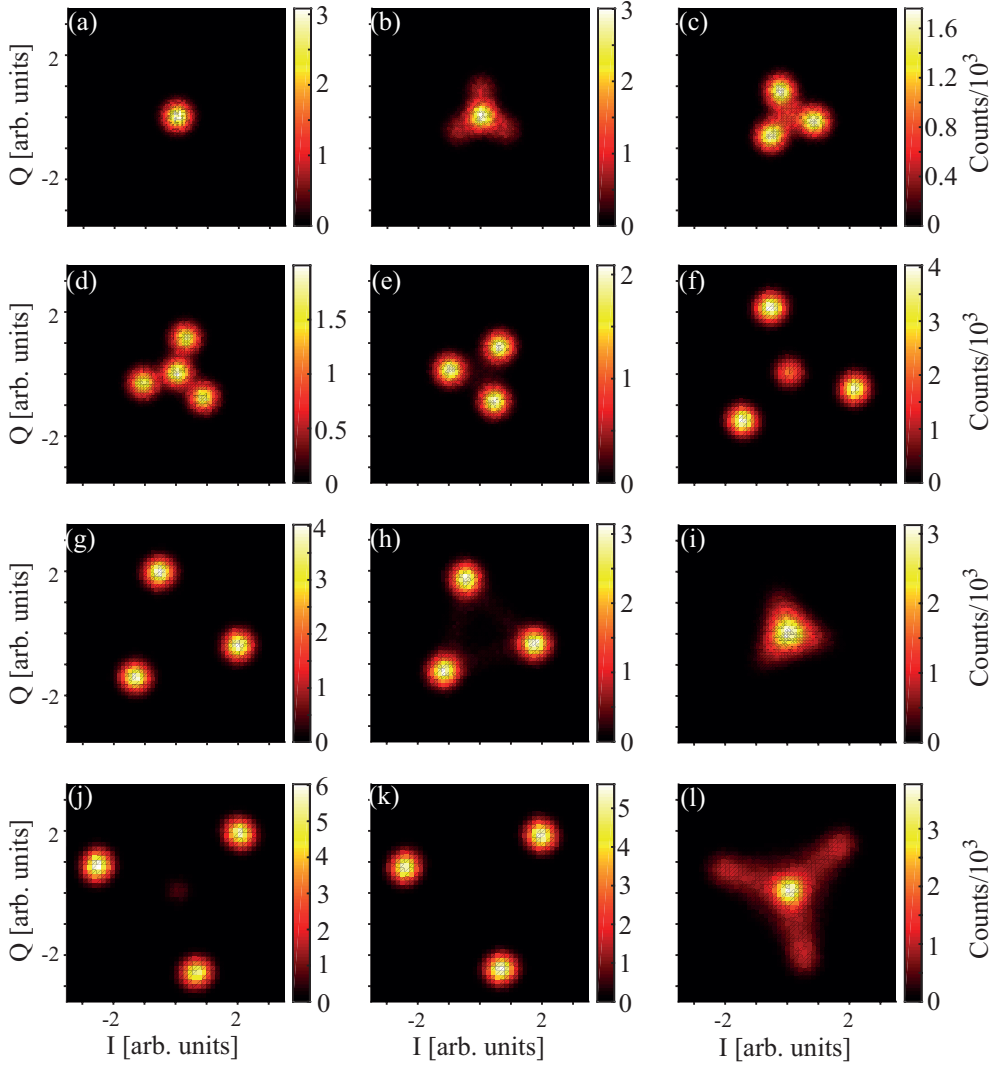
Figure 4.14: *Histograms measured at zero flux bias at the points indicated by the white circles in Fig. 4.15. The sampling rate is* $100\,kHz$ *and the number of samples* $5 \cdot 10^5$.
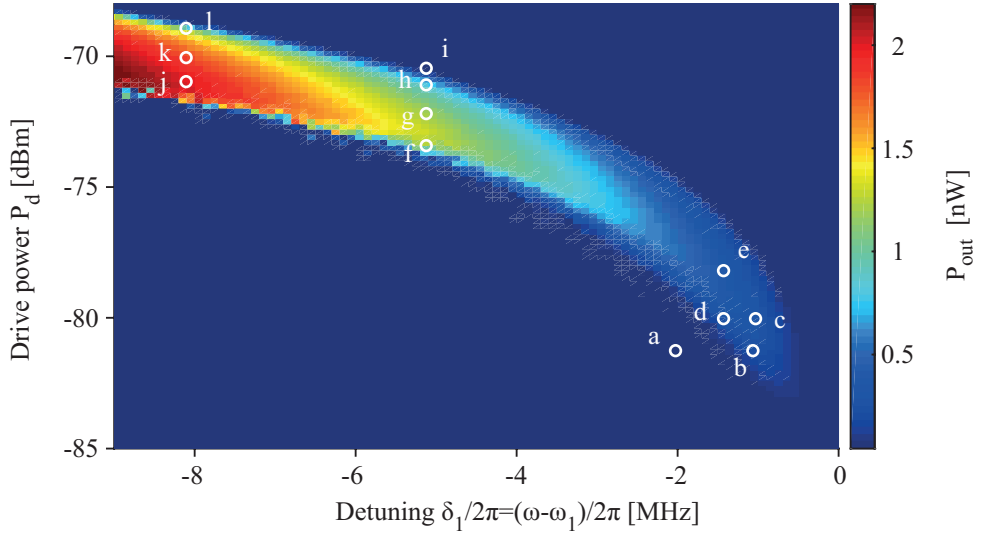
Figure 4.15: *Subharmonic oscillation region for sample #1 at zero flux bias and with a resonance frequency $\omega_1/2\pi = 5.504\,GHz$. The white circles indicate the positions of the histograms in Fig. 4.14.*

Figure 4.16: *Raw data for the quadrature traces forming the histogram in Fig. 4.14(g). The sampling rate is $100\,kHz$ and here the first 3000 out of $5 \cdot 10^5$ samples are displayed.*

Figure 4.17: *Histograms measured for sample #1 at 0.18 Φ₀ at the points indicated in Fig. 4.18. The traces are sampled at a frequency of $f_s = 100 \, kHz$ and consist of $5 \cdot 10^5$ samples.*

Figure 4.18: *Specification of the measurement points used in Fig. 4.17. This is measured using sample #1 biased at $0.18\,\Phi_0$ and the resonance frequency $\omega_1/2\pi = 5.432\,GHz$.*

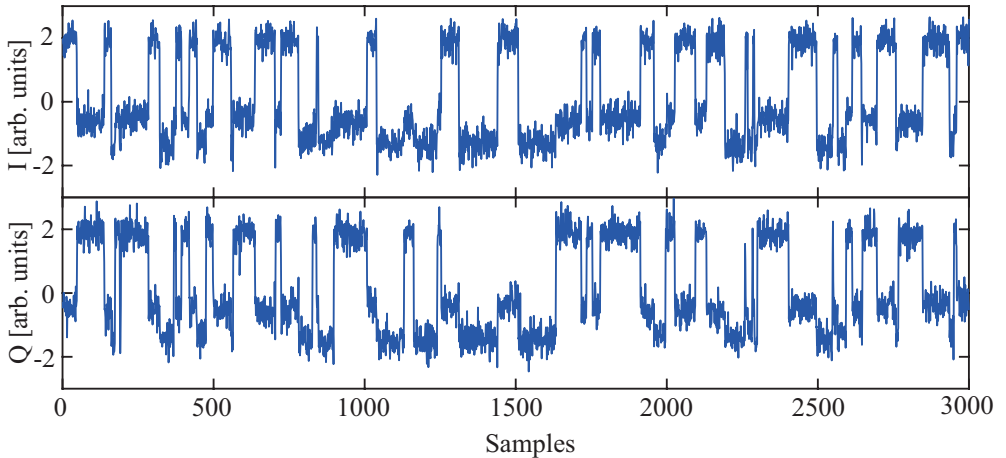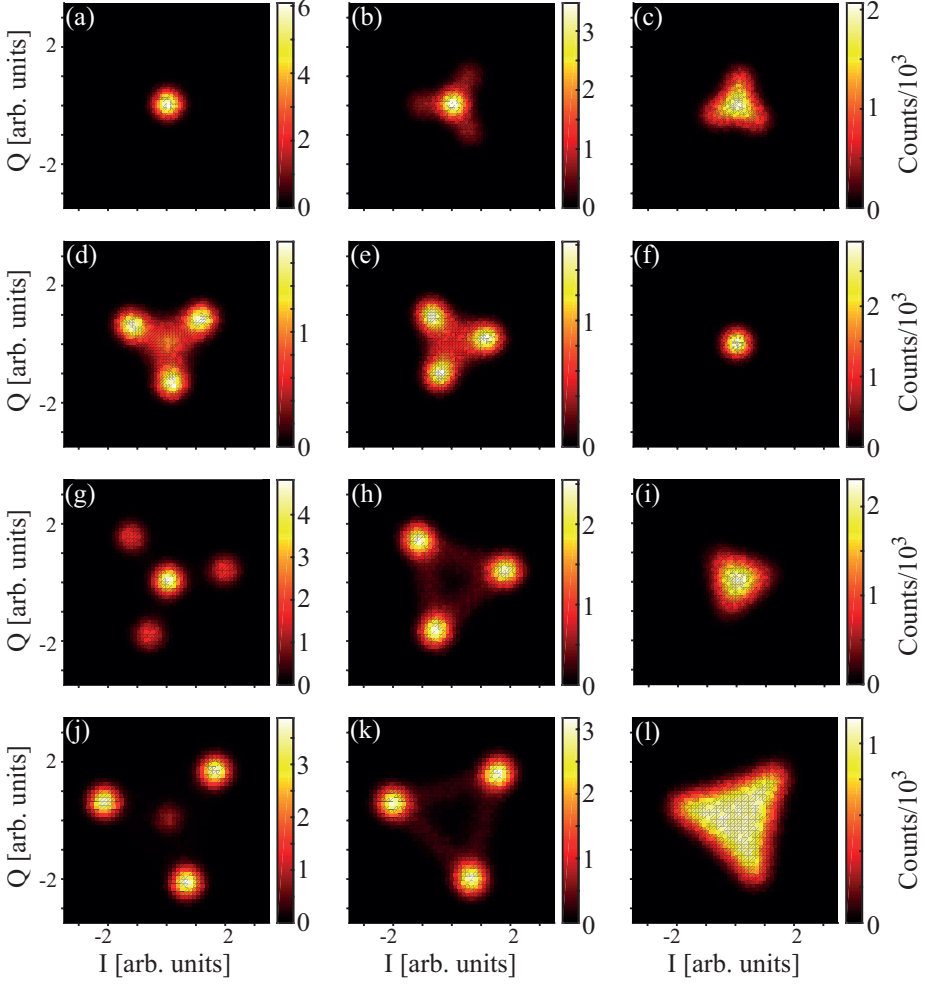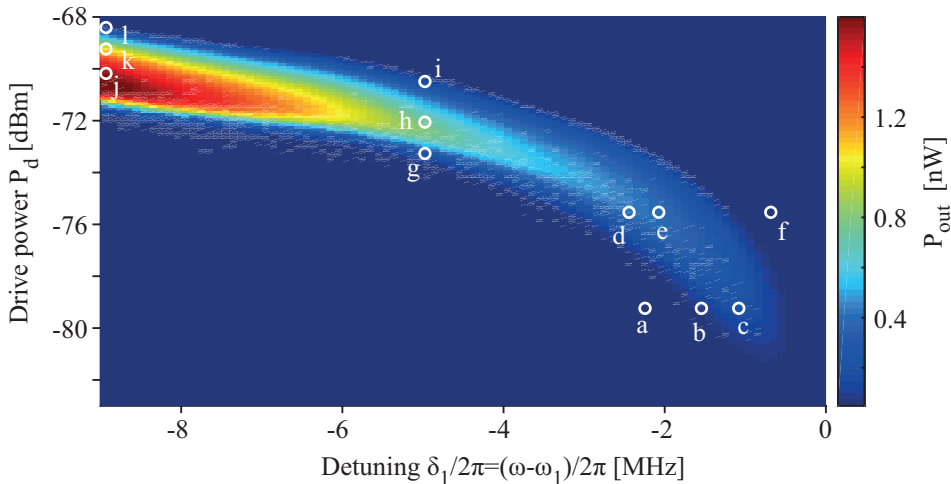The subharmonic oscillations have been observed in several different samples. In Fig. 4.19, histograms from sample #2 flux biased at $0.17\,\Phi_0$ are presented. The measurement points are indicated in Fig. 4.20. In this data set, all the histograms are taken at the same frequency but at different drive power. Hence, here the evolution of the system from the single ground state in (a) to the excited state can be followed. In (b) and (c) we see, in the competition between the ground state and the excited state, how the excited state first is weak and then grows stronger as the drive power is increased. Then, when we reach the middle (d) and the upper part (e-f) of the oscillation region the quadrature histograms show only the excited state. When the drive power is increased the amplitude of the state decreases.

In sample #1 and #2 the anharmonicity of the spectrum is positive, *i.e.* $3\omega_1 - \omega_2 > 0$, and for not too big flux bias values, the drive frequency is placed above the second mode, see Fig. 4.8. Contrarily, sample #3 has a negative anharmonicity for all flux bias values. The theory (Fig. 2.21 and 2.22) still predicts existence of the triplet excited state though in a smaller region, and indeed it can be measured, see Fig. 4.21. Again, the combination of the ground state and the triplet state in panel (b) is measured at the low drive power boundary, and the pure triplet state in panel (c) is measured in the middle of the subharmonic oscillation region.

In Paper A we show that we have a good agreement between theory and experiment for the case of positive anharmonicity. However, the negative anharmonicity regime is not explored. It can be noted that the subharmonic oscillation regions for sample #1 and #2 spread over larger ranges of both drive power and detuning compared to sample #3. This could be because of the spectrum anharmonicity. In the theory plots in Fig. 2.21 and 2.22, the regions of predicted stability are smaller for the negative anharmonicity than for positive. Another difference between the samples is that sample #3 is fabricated with a different technique and is of better quality. The better Q-value leads to narrower

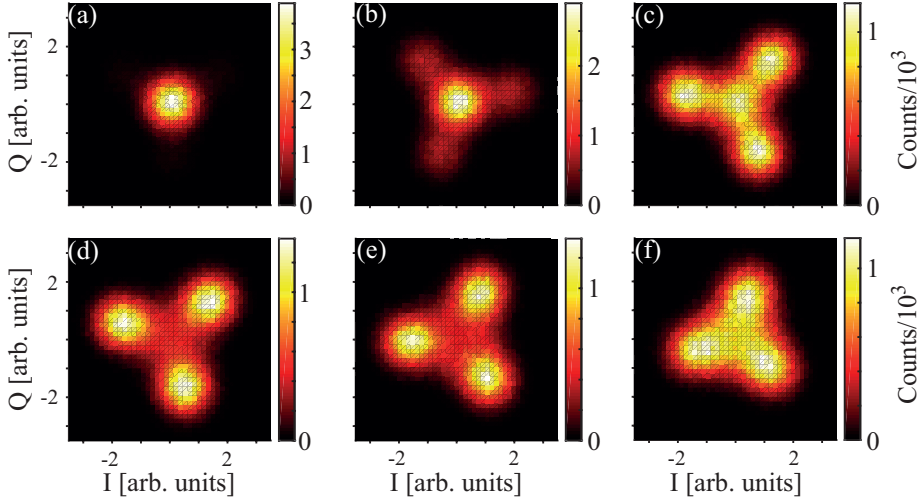Figure 4.19: *Histograms from sample #2 biased at $0.17\,\Phi_0$ and the resonance frequency $\omega_1/2\pi =$ 5.149 GHz. The measurement points are indicated in Fig. 4.20. The data is sampled at 100 kHz and consist of $4 \cdot 10^5$ samples.*
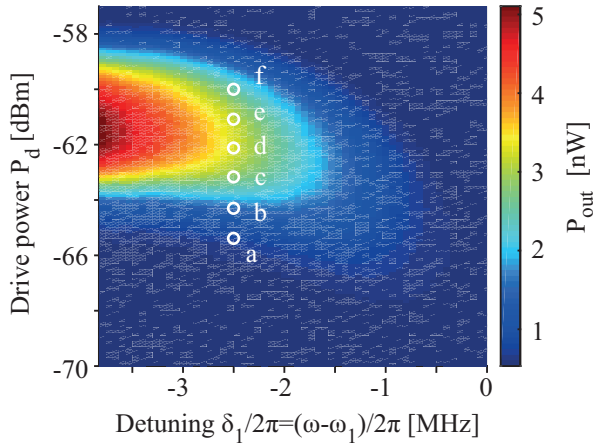

Figure 4.20: *The white circles indicate the measurement points for the histograms in Fig. 4.19. The data is measured on sample #2 biased at $0.17\,\Phi_0$.*
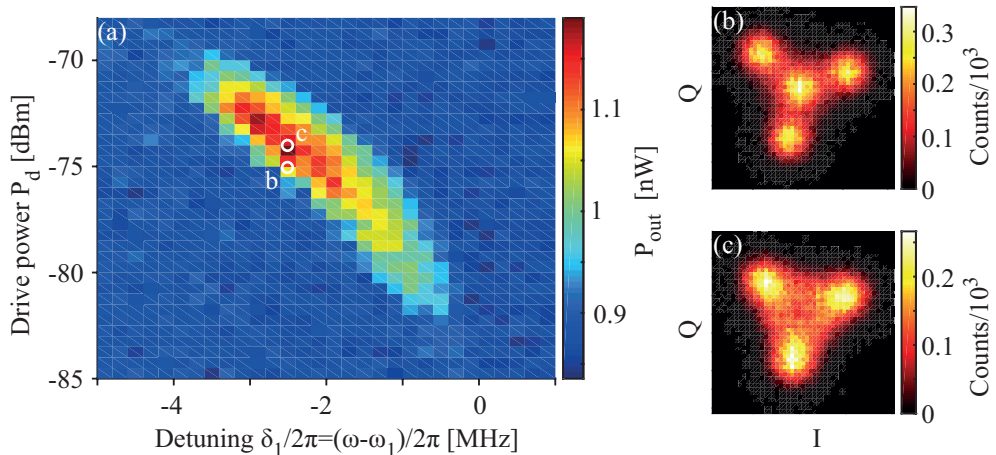
Figure 4.21: *Subharmonic oscillations in sample #3, which has a spectrum with negative anharmonicity. The histogram data is sampled at $100\,kHz$ and consist of $1 \cdot 10^5$. (a) Region of subharmonic oscillations. The white circles indicate the measurement points of the histograms in panel (b) and (c). (b) Quadrature histogram measured at the lower edge of the region. (c) Quadrature histogram measured in the middle of the region.*

modes, possibly this could also contribute to the more narrow subharmonic oscillation effect. Lastly, there is one difference between the different measurement setups, in which the samples have been measured, the sample boxes are different. Both sample #1 and #2 are measured using old style sample boxes with PCBs, these boxes are known to host parasitic modes. These background modes could facilitate the down-conversion process, similar to the increased efficiency induced by the second resonator mode. In contrast, sample #3 is measured in a new sample box, known to be free of spurious modes up to $12\,\mathrm{GHz}$, which is higher than $3\omega_1$. Hence, the reduced size of the subharmonic region could therefore possibly also be related to the absence of parasitic box modes.

Also sample #1 and #2 has regimes with negative anharmonicity, however no subharmonic oscillator effect has been observed in these cases. On the other hand, the asymmetric SQUID sample #5, characterized in Fig. 4.9, has shown weak subharmonic oscillations at negative anharmonicity. This sample has positive anharmonicity at zero flux but then it decreases and is negative around half a flux quantum. This is where I actually have measured a weak subharmonic response, at around half a flux quantum.

Analysis of a subharmonic region

In Paper A we show how we can fit three line cuts of Fig. 4.15 which is measured at zero flux bias. In Fig. 4.22, I show a fit of the subharmonic region in Fig. 4.18, measured at $0.18\,\Phi_0$. The first mode resonance frequency is $\omega_1/2\pi = 5.432\,\mathrm{GHz}$ and the Q-values are very similar to the zero flux values given in Paper A.

The drive power applied from a microwave source is related to the external drive field
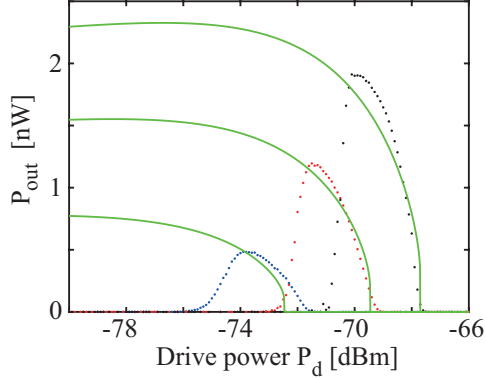
Figure 4.22: *Output power of the subharmonic oscillator versus drive power for sample #1 at the bias point* $0.18\,\Phi_0$. *The dotted traces correspond to three line cuts of Fig. 4.18,* $\delta_1 = -3.5,\ -7,\ -10.5\,MHz$. *The green traces correspond to a fit.*

$|B_2|^2$ as

$$P_d = 3\hbar\omega|B_2|^2 10^{Att/10},$$

where *Att* denotes the total attenuation of the microwave signal from the source to the sample. Furthermore, the external drive populates the second mode following Eq. (2.59), which gives

$$P_d = 3\hbar\omega\frac{(3\omega_1 - \omega_2)^2 r_2^2}{2\beta^2\Gamma_{ext,2}}10^{Att/10},$$

where $\Gamma_{ext,2} = \omega_2/2Q_{ext,2}$. The second mode population acts as a parametric pump on the first mode which gives rise to a population in the first mode according to Eq. (2.56). The generated signal in the first mode is then measured as

$$P_{out} = \hbar\omega r_1^2 2\Gamma_{ext,1}10^{G/10},$$

where $G = 66\,\text{dB}$ denotes the total gain on the output line. Combining these three expressions above gives one single fitting parameter, $X = Q_{ext,2}10^{Att/10}$. Other resonator specific parameters are found in Table I in Paper A. The fit in Fig. 4.22 is for $X = 1.5\cdot10^{11}$. A discrepancy between the theory curve and the measurement data can be seen in Fig. 4.22, at he low power side of the subharmonic region. As discussed in Paper A, this is because the theory only predicts the existence of the excited state and the ground state but not which one the system prefers.

The six-blob histogram

As a peculiar detail I found a very special form of the third order subharmonic oscillations in sample #2, see Fig. 4.23 and Paper B. For small detuning values, the system shows either a combination of the triplet excited and ground state, or only the excited state. However, for larger values of the detuning, the middle state suddenly divides into three states. We have not come up with an explanation for this effect, but as seen here, it
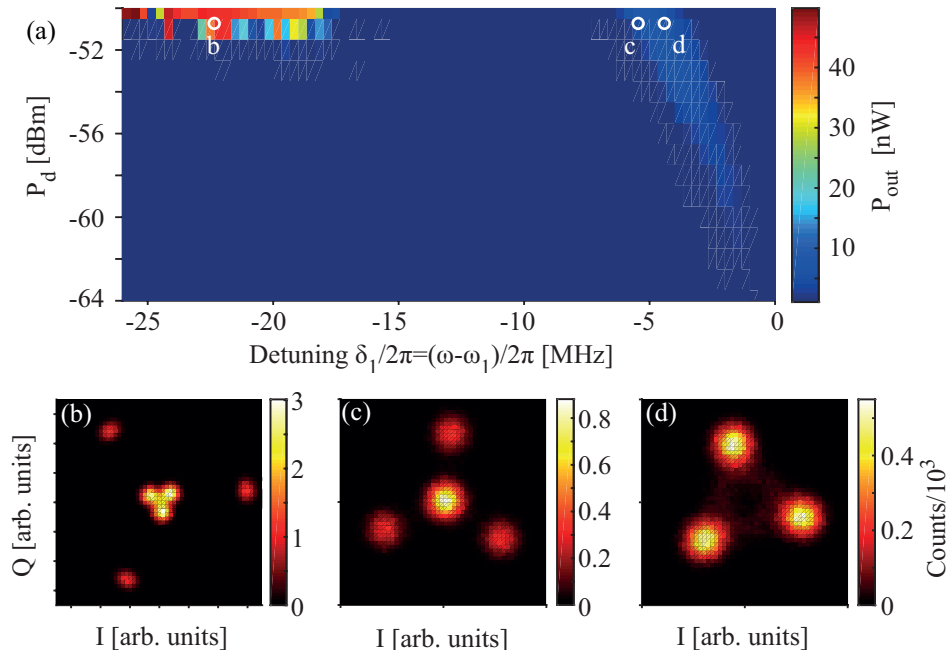
Figure 4.23: *Quadrature histograms of subharmonic oscillations measured in sample #2 at $0.1\,\Phi_0$. (a) Subharmonic oscillation region, the white circles indicate the measurement points of the histograms in panel (b-d). Note the special feature in (b), where the state is divided up into two distinct triplets.*

appears at larger detuning where the signal levels are stronger. The effect could be due to some higher order nonlinearity triggered by the strong subharmonic oscillator intensity.

Subharmonic oscillations with a probe signal

The configuration is described in Fig. 4.24. There is an external current drive signal at $\omega_{drive} = 3\omega$ and the measurement is set to be $\omega_{meas} = \omega$. In addition, a probe signal is applied at $\omega_{input} = \omega + \delta$. The probe and the drive signals are applied through the same cable, they are combined in a microwave combiner at room temperature.

Figure 4.25 shows measurements with zero detuning between the measurement frequency and the probe signal. The three different panels represent increasing probe power. Note how all the three states have similar intensity in panel (a). In (b), the top right state has decreased in intensity and in (c) one state is gone, and of the remaining two states, one is bright and one is weak. The system, without a probe signal, is defined by the phase portrait in Fig. 2.20, which illustrates a metapotential with three excited states and one middle ground state. The effect of the probe signal in Fig. 4.25 indicates that the metapotential is tilted, the stronger the probe, the larger the tilt. In (a), when the probe signal is weak, the metapotential remains flat and all three states are populated. When the probe power is increased, the metapotential gains a small tilt and as seen in
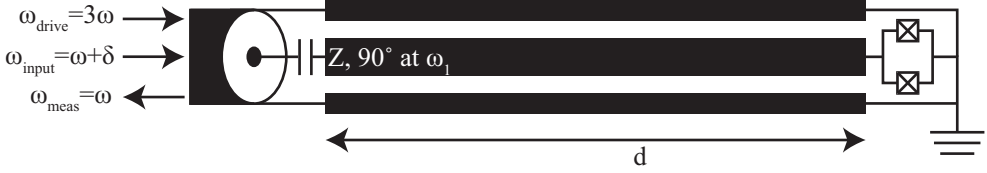
Figure 4.24: *Measurement configuration for subharmonic oscillations measured with an applied probe signal. The measurement is fixed at frequency ω and the drive at 3ω. An additional probe signal is applied at $\omega + \delta$.*
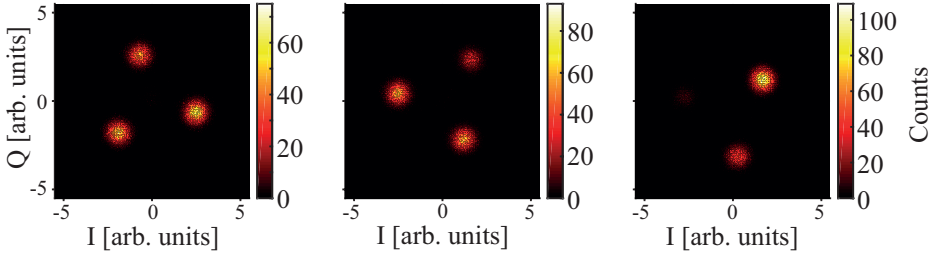

Figure 4.25: *Quadrature histograms of a subharmonic oscillator with an additional probe signal applied. The detuning between the probe signal and the measurement frequency is is set to zero. The three different panels are taken for three different powers of the probe signal, (a) $-146\,dBm$, (b) $-136\,dBm$ and (c) $-126\,dBm$. They are all sampled at $100\,kHz$.*

(b) one state becomes less populated, an indication that it is energetically less favourable. Furthermore, in (c) when the probe power is even higher, the tilting effect grows stronger. One state remains strong, one is weak and one barely visible.

More interesting effects can be created, when the detuning between the measurement signal and the probe is set to a finite value. In Fig. 4.26, $\delta = 1\,$Hz and this gradually deforms the states into crescent like features.

4.3.2 Current driving vs flux pumping

In Fig. 4.27, I present a comparison between (a) driving the SQUID with an external signal applied to the input port, and (b) by pumping through the on-chip flux pump line, for modulation at 3ω. The two graphs show similar features. The onset of oscillations occur at in principle the same frequency. The increase in oscillation intensity with detuning is very similar. The points at which the response disappears and reappears occur at the same frequencies in both cases. One difference is the wiggles of the oscillation region. Likely, these wiggles are due to background resonances in the setup and in the sample box. Since the current drive and the flux pump signal goes through different cables, they are likely to show different backgrounds. This flux pumping result can be explained either by an asymmetry in the SQUID (as discussed in Paper B) or by a parasitic coupling between the on-chip flux pump line and the resonator. Even though the SQUID is designed to be symmetric, due to imperfections in the fabrication process, a small asymmetry is not
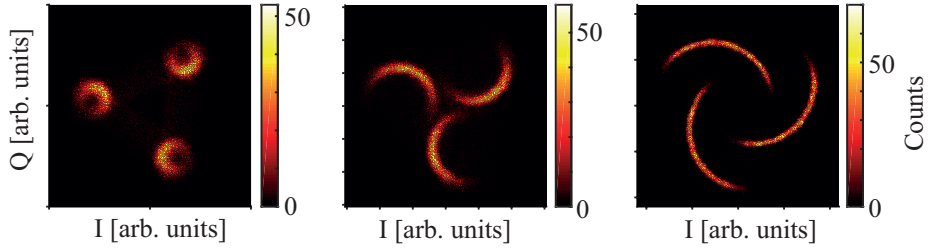
Figure 4.26: *Quadrature histograms of a subharmonic oscillator with an additional probe signal applied slightly detuned from the measurement frequency. The detuning is $\delta = 1\,Hz$. The panels common parameters are $f_{sampling} = 10\,kHz$ and $\#samples = 1 \cdot 10^5$. The probe power for the three panels are $P_{probe} = $ (a) $-126\,dBm$ (b) $-116\,dBm$ (c) $-106\,dBm$.*
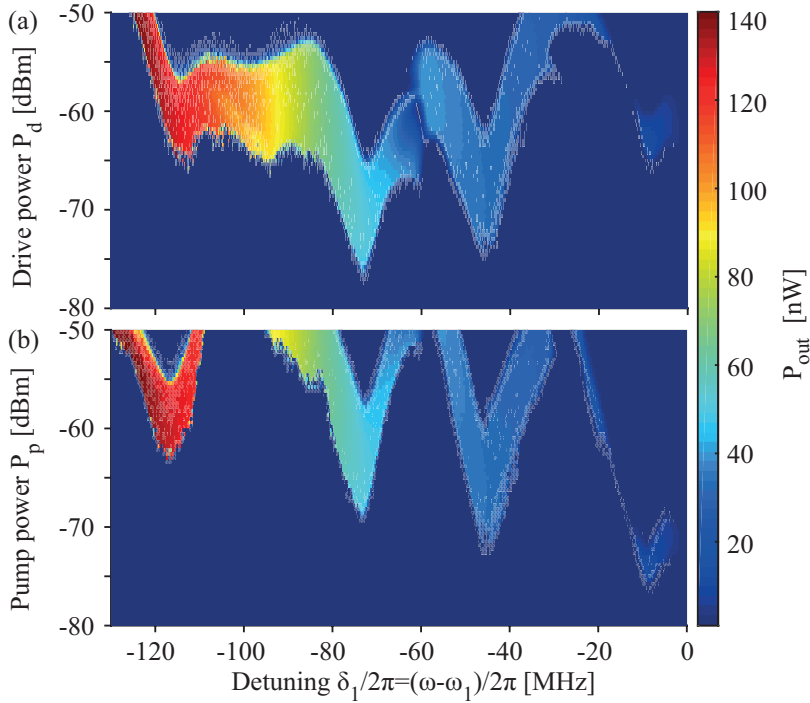
Figure 4.27: *Flux bias $\Phi_{dc} = 0.17\,\Phi_0$. (a) Subharmonic oscillations generated through current driving. (b) Subharmonic oscillations generated through pumping the on-chip flux tuning line.*
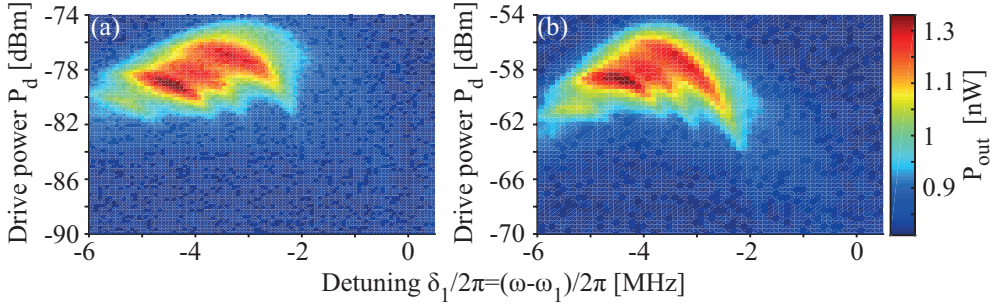
Figure 4.28: *Subharmonic oscillation regions for (a) an external drive of the Josephson junction and (b) for pumping the Josephson junction through the on-chip flux pump line.*

surprising.

To further investigate the effect of current driving versus flux pumping, a control sample was fabricated with a single Josephson junction instead of a SQUID, terminating the resonator. The Josephson junction is to first order flux insensitive and should, in the case of pure flux pumping, not give any effect. For the current drive it does not matter, whether the nonlinear element is a SQUID or a single junction, the effect should be the same since the SQUID is just effectively a flux-tunable junction. In Fig. 4.28, the two modulation methods are compared for the single junction sample. In (a) an external current drive signal is applied at 3ω, and subharmonic oscillations are measured at ω. In (b) a microwave signal is applied to the on-chip flux pump line at 3ω and again, even though the resonator is supposed to be insensitive to flux, subharmonic oscillations are measured at ω. The similarity of the two panels in Fig. 4.28 indicate that there is some mechanism, coupling the flux pump signal to the resonator and cause a current drive. This coupling could be an effect of parasitic coupling between the flux pump line and the resonator. Another possible coupling mechanism would be via spurious modes in the sample box. From the available data there is no possibility to deduce which mechanism is the dominating one.

4.3.3 Period multiplication subharmonic oscillations

The subharmonic oscillations are not limited to period-tripling. In Paper B we show that we can generate, from period-doubling subharmonic oscillations, up to period-quintupling, in a $\lambda/4$-resonator. Both in Paper B, and here in this section of the thesis, I focus on SQUID modulation through the on-chip flux pump line. In the Paper we present how the period-multiplication effect in a superconducting resonator can be connected to the theory model presented by Guo *et al.* [78]. As discussed in the paper we have two cases, flux pumping at even or odd multiples of ω. Pumping at even multiples correspond to parametric pumping, while pumping at odd multiples requires an asymmetry in the SQUID to generate a period-multiplication effect. It is not clear how large asymmetry is required but my measurements indicate that the imperfections in the fabrication process are enough. The expected asymmetry of a nominally symmetric SQUID is of the order of a

Table 4.2: An overview of different cases, if subharmonic oscillations are expected from theory or not for different modulation frequency multiples. The different SQUID modulation mechanisms are current driving and flux pumping. The SQUID can either be symmetric and have two junctions with equal critical current or asymmetric and have two junctions with different critical current. For the flux pump case there could be a parasitic coupling between the flux pump line and the resonator, this is in the table denoted CT for crosstalk.

Frequency	Current drive	Flux pump		
		Sym SQUID	Asym SQUID	Sym SQUID
		No CT	No CT	With CT
2ω	No	Yes	Yes	Yes
3ω	Yes	No	Yes	Yes
4ω	No	Yes	Yes	Yes
5ω	Yes	No	Yes	Yes

few percent. A summary, of whether theory predicts existence of subharmonic oscillations or not for different cases, is found in table 4.2. For current driving at even multiples, no effect is expected. Even so, I have measured period-doubling by current driving, see Appendix B.3.

Period-quadrupling subharmonic oscillations

Period-quadrupling subharmonic oscillations indicate that I use a modulation frequency that is four times the measurement frequency. An example of the effect, generated by applying a microwave signal at 4ω to the flux pump line, is given in Fig. 4.29 for sample #4 biased at $\Phi \approx 0.1\,\Phi_0$. In panel (a) I present the subharmonic region and in the measurement points indicated by the white circles I extract the quadrature histograms presented in (b)-(g).

The histograms in Fig. 4.29 show quartet excited states. In some of the histograms there is an indication of an additional middle ground state apart from the quartet excited state, for instance panel (b,d,g). In panel (f), there are faint lines between neighbouring states, indicating that switching appears between neighbouring states. In contrast, the pattern in (b) indicates that switching also can go through the middle, because of the existence of the stable ground state.

One limiting factor here, visible in Fig. 4.29(a), is the limitation on pump power. The available microwave source could not supply more power. However, within the setup limitations I can conclude that for 4ω-pumping there is no detected frequency down-conversion for zero flux. Since the frequency down-conversion for pumping at even multiples is a regular parametric process, we would not expect any effect at zero flux.

As shown, a period-quadrupling effect is observed for a flux pumped tunable resonator. According to theory, no effect is expected for current driving. In my measurements I can show, within the limitations of the measurement setup, a minor effect at current driving. Though, the period-quadrupling effect is significantly stronger for flux pumping than for current driving, in agreement with theoretical arguments.

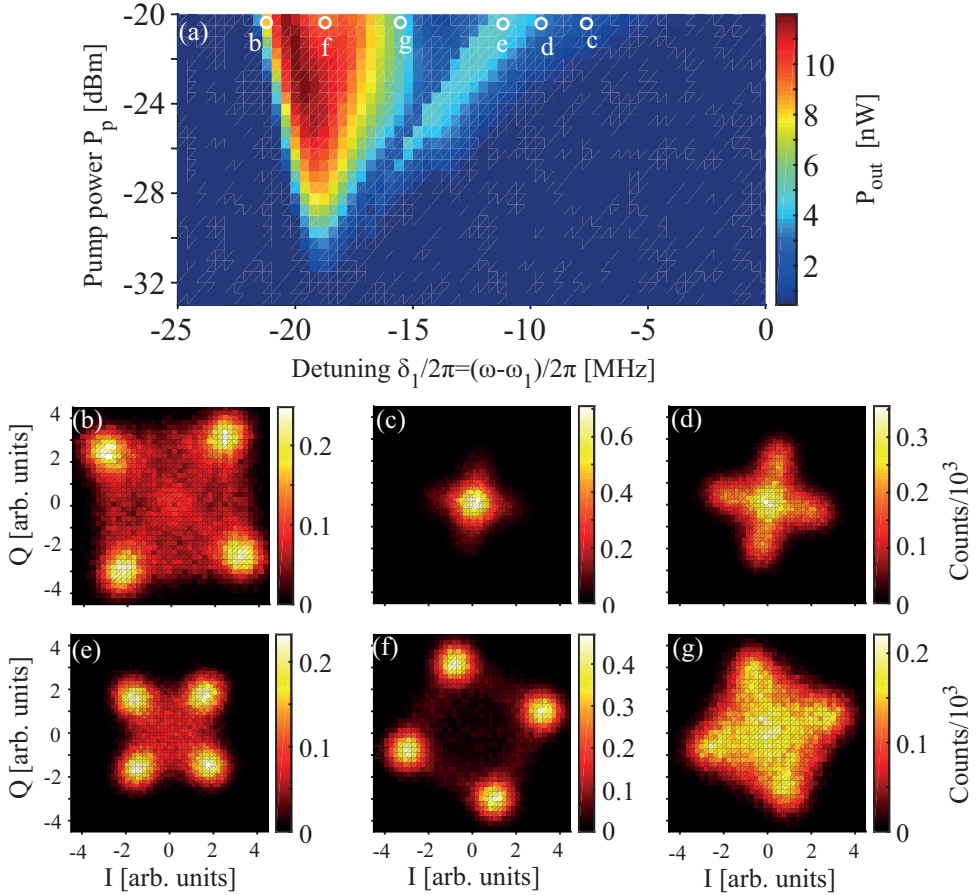Figure 4.29: *Period-quadrupling subharmonic oscillations generated by applying a microwave signal at frequency 4ω to the flux pump line and measuring at ω. (a) Region of subharmonic oscillations. Unfortunately, at the time, the measurement setup did not allow a larger pump power. (b)-(g) Quadrature histograms of the detected output signal. The measurement points are indicated by the white circles in (a).*
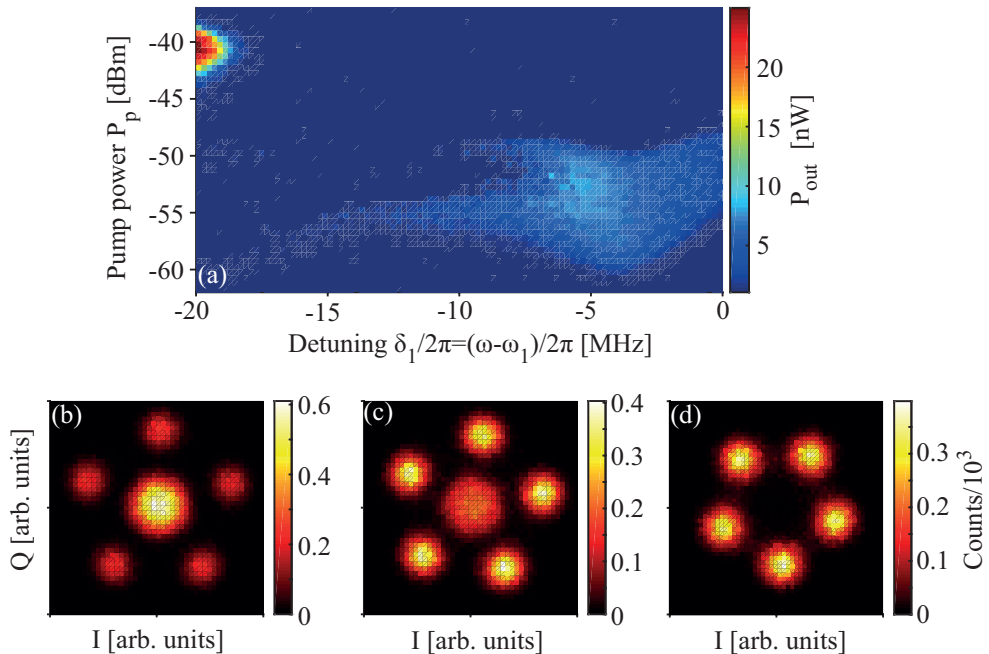
Figure 4.30: *Period-quintupling subharmonic oscillations generated by applying a flux pump signal at 5ω and detecting the output signal at ω. (a) Subharmonic oscillation region, that here is divided into two pieces. (b-d) Two different types of quadrature histograms are found, one with only a quintet excited state and one with both the quintet state and a ground state in the middle.*

Period-quintupling subharmonic oscillations

For generating period-quintupling subharmonic oscillations I apply a microwave signal to the flux pump line at a frequency 5ω and I set the digitizer readout frequency to ω. Following the discussion from Paper B, a generation of subharmonic oscillations at an odd multiple requires a small asymmetry in the SQUID. Alternatively, the pump signal can couple via a parasitic crosstalk from the flux pump line to the resonator modes and populate them. In turn this excitation can facilitate down-conversion to the first mode where I read out subharmonic oscillations. The data presented in Fig. 4.30 is extracted from sample #2. Panel (a) shows the generated output power and in (b)-(d) three quadrature histograms are presented, all measured in the strong output power part in the top left corner of (a).

To get an idea of how the system switches between the states a test with varying sampling frequency was performed, see Fig. 4.31. For the fastest sampling, panel (c), it seems like the switching is mainly through the middle state, possibly some nearest neighbour switching occurs as well. At the lower sampling rates, in panel (a) and (b), there are indications that there could be switching between neighbouring excited states.

Some reflections from the period-quintupling measurements. The required pump power to reach the subharmonic oscillation threshold is generally lower for period-quintupling
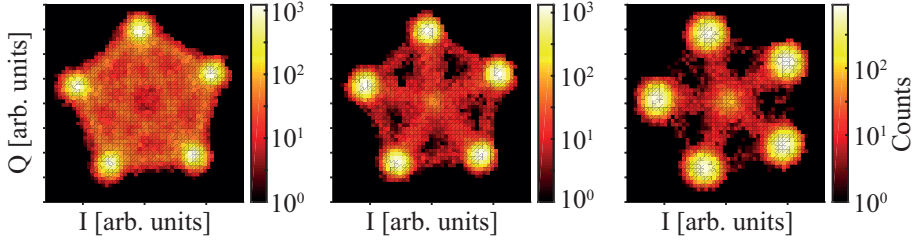
Figure 4.31: *Period-quintupling subharmonic oscillation histograms measured with different samplings frequencies, 10, 50 and 100 kHz. Here, the colour scale is presented in logarithmic scale to highlight the traces of switching between different states.*
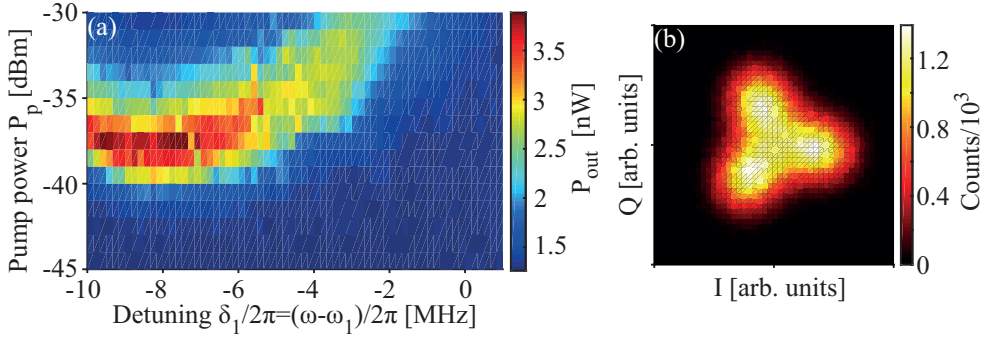
Figure 4.32: *6ω subharmonic oscillations at the bias point $0.3\,\Phi_0$. In (a) the subharmonic oscillation region and in (b) a quadrature histogram extracted at the maximum generated output power in (a). Interestingly there seems to be only three states.*

compared to period-quadrupling. Furthermore, the regions, in which the subharmonic oscillations are generated, are very similar for current driving and flux pumping in the period-quintupling case.

6ω subharmonic oscillations

In most samples, attempts at 6ω-modulation has not given any response. However, as a curiosity, for sample #2 an effect was found for modulation through the on-chip flux pump line, see Fig. 4.32. The quadrature histogram shows three bright spots not six. I show this only as a curiosity. For this sample, with a fundamental mode resonance frequency around 5 GHz, $6\omega \sim 30$ GHz. It is likely, that the SQUID plasma frequency is found lower or close to the modulation frequency. It remains unknown how the generated radiation is affected by direct excitation of the SQUID.
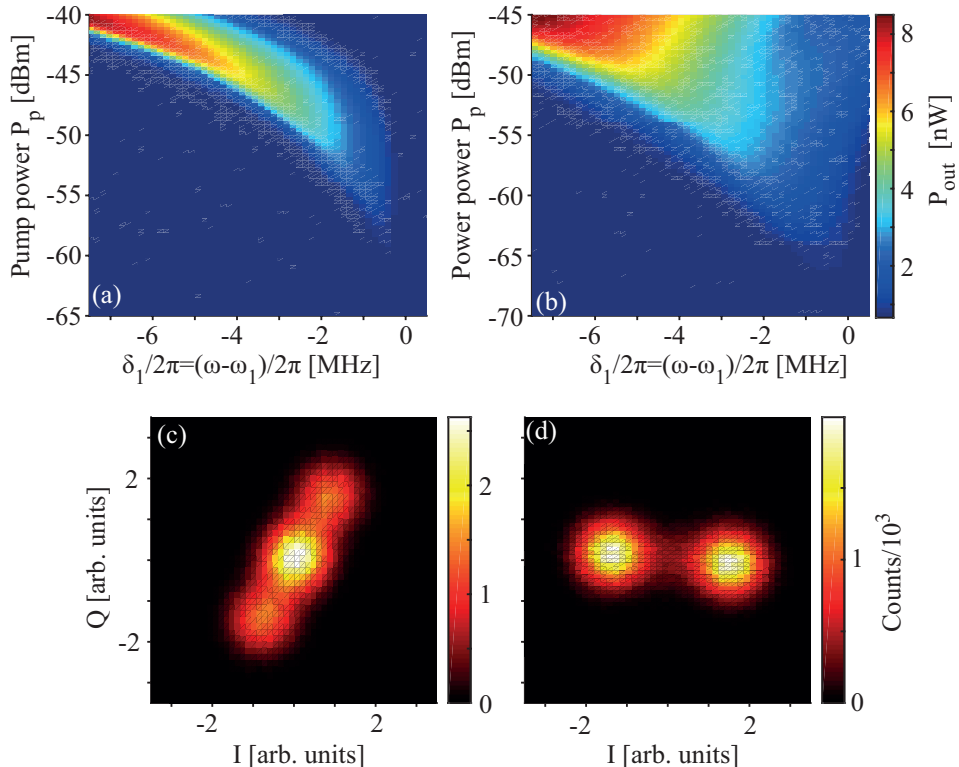
Figure 4.33: *Parametric oscillation regions generated by flux pumping the SQUID at 2ω, (a) $0.1\,\Phi_0$ and (b) $0.3\,\Phi_0$. Two typical quadrature histograms, (c) measured at the lower region boundary of (a) and (d) measured in the middle of the region in (a).*

4.3.4 Standard parametric oscillator

For use as a comparison with the doubly tunable resonator, I here present some standard parametric oscillator properties, measured using the single-SQUID tunable resonator, sample #2 (see Table 4.1). Here we assume that the SQUID modulation mechanism is purely flux pumping. Remember the theoretical predictions in Fig. 2.23 and 2.24. The parametric oscillation region is, due to nonlinearity, shifted in frequency, an effect especially pronounced at low flux bias. In experiments this effect is easily observed, see Fig. 4.33(a) and (b). Furthermore, the system indeed shows a combination of a ground state and two π-shifted states at the lower oscillation boundary and two separate states in the middle of the region, see Fig. 4.33(c) and (d).

4.3.5 Photon generation in the doubly tunable resonator

In paper C our measurement results on the doubly tunable resonator are presented. As written, we find some very promising results in nice agreement with theory. For example, we find that, for a single pump measurement, the system behaves as a parametric
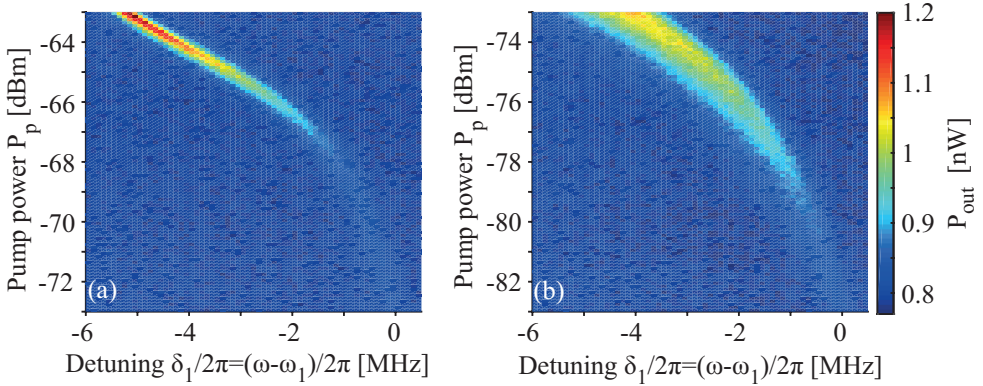
Figure 4.34: *Single pump parametric regions for the doubly tunable resonator. (a)* $0.1\,\Phi_0$ *(b)* $0.3\,\Phi_0$.
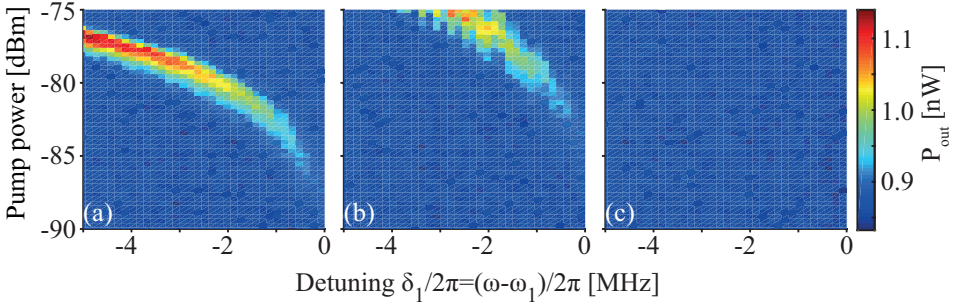
Figure 4.35: *Double pump parametric regions for three different values of the phase difference between the pumps. (a)* $\varphi = 0°$ *(b)* $\varphi = 90°$ *(c)* $\varphi = 180°$

oscillator, it forms a parametric region, and inside that region, a histogram can be measured illustrating two π-shifted states. Furthermore, for a double pump configuration, parametric regions can be measured, where the region threshold depends on the phase difference between the two pumps. However, there are also some contradicting findings and here I will show some additional measurement results, indicating parasitic effects. The experimental data in Paper C is measured on sample DTR #5. This is also the sample, from which the data in this section is collected.

For a single flux pump at 2ω, the doubly tunable resonator should behave very similar to the standard parametric oscillator. In Fig. 4.34 I have plotted the regions for (a) $\Phi_{dc,l} = \Phi_{dc,r} = 0.1\,\Phi_0$ and (b) $\Phi_{dc,l} = \Phi_{dc,r} = 0.3\,\Phi_0$, and these should be very similar to the regions of Fig. 4.33. It can be noted that the doubly tunable resonator generate very narrow parametric regions, compared to the standard parametric oscillator. In addition, the pump power required to generate an output signal is roughly $10\,\mathrm{dB}$ lower here compared to the standard parametric oscillator. Even though the on-chip flux pump lines and SQUIDs are very similar.
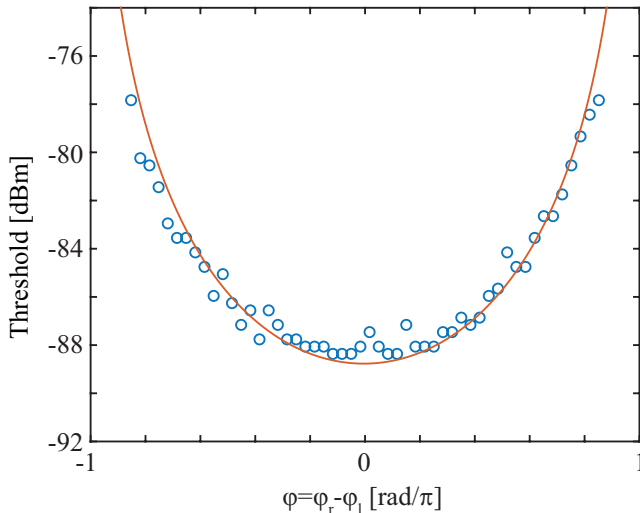
Figure 4.36: *Extracted thresholds for the parametric regions created by using both flux pumps in the doubly tunable resonator. The red line corresponds to a theory comparison using Eq. (2.72a).*

Also for double pumping of the doubly tunable resonator, parametric regions can be generated. In Fig. 4.35, regions for pump phase differences 0, 90 and 180 degrees, for the bias point $\Phi_{\mathrm{dc,l}} = \Phi_{\mathrm{dc,r}} = 0.3\,\Phi_0$ are presented. For each pump phase difference, the threshold has been extracted, see blue circles in Fig. 4.36. These thresholds have been compared to the model in Eq. (2.72a). The theoretical threshold can be extracted by setting $\epsilon = \sqrt{\delta^2 + \Gamma^2}$. For simplicity I work with $\delta \approx 0$. The effective pump amplitudes are given by $\delta f_{r/l} = M_{ac}\sqrt{2}\sqrt{10^{(P_p - P_{att})/10}/50}$, where P_{att} denotes the attenuation on the pump line and M_{ac} is the mutual inductance between the on-chip flux pump line and the SQUID. The resonator parameters used in the comparison are found in Table 2 of Paper C. The specific bias point used here has the resonance frequency $\omega_1/2\pi = 5.160\,\mathrm{GHz}$ and $Q_{tot} = 1 \cdot 10^4$. The phase offset has been adjusted so that the minimum threshold is at zero. Since it is difficult to separate the attenuation and the mutual inductance I use the parameter $k = M_{ac}\sqrt{2}\sqrt{10^{P_{att}/10}/50}$. I also assume, that the crosstalk is symmetric $\xi_{ac,r} = \xi_{ac,l} = \xi_{ac}$. The red theory comparison in Fig. 4.36 has been calculated for $k = 5.5 \cdot 10^{-5}$ and $\xi_{ac} = 1$. This theory trace does not fit perfectly to the data, by taking more imperfections into account such as differences in pump power for the two pumps, a better agreement could be found. However, the following paragraph will explain why there is no point in spending time finding a good fit using a flux pumping model.

To probe the microwave crosstalk between a SQUID and its opposite flux pump line, a doubly tunable resonator, where one SQUID was replaced by a continuous transmission line, was fabricated. Since there is only one SQUID, the effect of the opposite flux pump line is a direct measure of the ac crosstalk. In Fig. 4.37, single pump parametric regions for (a) using the flux pump line with a SQUID, and (b) using the flux pump line without a SQUID are presented. Ideally, there should be no effect when there is no SQUID, though as seen in the graphs, the generated effect is almost identical independently which flux
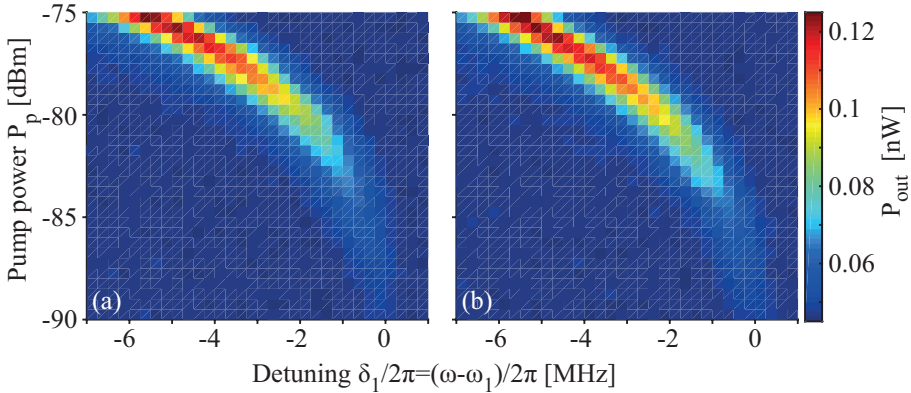
Figure 4.37: *Single pump parametric regions for a single SQUID control sample. (a) Pumping on the flux pump line with a SQUID. (b) Pumping on the flux pump line without SQUID.*

pump line is used. This is an indication that the crosstalk is very close to 100 % or the SQUID is modulated by another mechanism than flux pumping. A guess, supported by the measurement results of double pumping of the single SQUID sample (Fig. 4(c) in Paper C), is that the SQUID is current driven due to a parasitic coupling between the flux pump line and the resonator.

4.4 Microwave manipulation with the tunable coupling

Paper E and F present experimental results of microwave signal manipulation using the tunable coupling architecture in Fig. 2.29. There are two samples, A and B, where sample A is close to the critical regime and sample B is in the underdamped regime.

Paper E treats the measurement results of sample A. It is shown that the escape rate from the storage resonator to the transmission line can be tuned over three orders of magnitude, by changing the flux in the SQUID loop of the coupling resonator and thereby tune its resonance frequency. The storage resonator is loaded by tuning the coupling resonator on resonance with the storage resonator. Then the coupling is turned off for some time and then the microwave signal is released when the coupling is turned back on. In a controlled pulse sequence with varying storage time, a maximum storage time of $18\,\mu s$ has been extracted. The possible storage time is mainly set by the intrinsic Q-value of the storage resonator, which for sample A is 6×10^5. This corresponds to a storage time of $18\,\mu s$ for the storage resonator frequency $5.186\,\mathrm{GHz}$. Note that there is an additional factor of $1/2$ to convert the voltage decay rate to an energy decay rate.

After storage the microwave signal is released by tuning the coupling resonator back on resonance. The fastest possible release is found for zero detuning between the coupling and storage resonator, $14\,\mathrm{ns}$. However, the release time and the shape of the released signal can be controlled by choosing a finite detuning between the coupling and storage

resonator.

In Paper F we perform experiments using sample B. This sample is in the underdamped regime, the coupling between the two resonators is stronger than the coupling to the transmission line. On resonance we observe oscillations in the two-mode system due to the relatively strong coupling between the resonators compared to the coupling to the transmission line. The energy has time to oscillate between the resonators before leaking out. This also means that, compared to sample A, the release time is much longer in sample B, limited by the coupling to the transmission line.

Direct loading of the storage resonator can only be done at the resonance frequency of the same. However, the coupling resonator can be tuned over a wide frequency range. If off-resonant, the coupling resonator can be loaded with a coherent state while leaving the storage resonator empty. Then by performing a swap operation, *i.e.* tuning the resonators on-resonance, the contents of the two resonators can be swapped. The signal can be stored for some time in the storage and then a second swap operation is performed to transfer the signal back to the coupling resonator and read out. This process has been demonstrated in excellent agreement with theoretical predictions.

5

Conclusion and outlook

In this thesis I have presented three different systems that all rely on tunable superconducting resonators. These systems have been characterized and two of them, the subharmonic oscillations and the tunable coupling, have been shown very promising. Classically, we have shown interesting properties of these systems. Since low loss superconducting circuits are used, it is likely that quantum versions of the effects could also be created. Even though there are some problems with the doubly tunable resonator, it remains an interesting system, possible to use for experiments on relativistic effects, as well as for creation of non-classical states.

The period-tripling subharmonic oscillations are now extensively studied in the classical, weak signal regime. What remains unknown is for instance, the behaviour at higher signal levels, such as the double triplet state. There are also possibilities to further explore the negative anharmonicity regime. On a classical, many photon level the positive and negative anharmonicity results are not that different, however in the quantum regime, possibly there could be something interesting.

To further understand the more general period-multiplication subharmonic oscillation case, some more theory work is needed, in combination with more systematic measurements. Here, we show that the subharmonic oscillations exist for pumping at different multiples and there are reasons to believe that these could form interesting non-classical physics. However, from the present measurement results it is difficult to draw conclusions because of several unknowns, one is the possible presence of direct SQUID excitations, due to the proximity of the SQUID plasma frequency. Therefore, new measurements should be done with a SQUID where the plasma frequency is maximized and possibly the resonator frequency minimized, with respect to the limitations of our measurement setup.

The doubly tunable resonator has been realized in this thesis, and remains an interesting idea even if there are technical problems. I strongly believe that the parasitic coupling problem causing huge crosstalk and current driving could be solved. A stepped impedance design could be one way to go, to increase the distance between the pump frequencies and higher resonator modes. Another solution could be to change the sample design, the impedance in the ground plane loop, formed by the resonator centre conductor and the ground plane, could be increased, to avoid circulating currents. Possibly, the best design

is a variation of the parallel on-chip flux tuning line design (Fig. 4.10(b)). Since this one has an outlook to cut at least partly also the ac crosstalk.

At the moment, no attempts have been made to measure the time dilation in the doubly tunable resonator. However, the problems encountered in the parametric pumping are not necessarily relevant for the twin paradox measurements. Assuming that the parasitic coupling between the on-chip flux tuning lines and the resonator, is connected to resonator modes, the space trip could be realized with signals with frequencies far from the mode frequencies.

In both the subharmonic oscillations project and the doubly tunable resonator there is potential interaction with parasitic box or other background modes. Both these projects would benefit from having less parasitic modes in the sample boxes. This could be achieved, both by decreasing the frequency, since there are less parasitic modes at lower frequencies, or by designing new better boxes where the parasitic modes are pushed to higher frequencies.

The tunable coupling is shown to work very well for storage of microwave fields. There is an excellent agreement between theory and experiments. One improvement would be to increase the Q-value of the storage resonator, to increase the possible storage time, with the new fabrication recipe (section A.2) colleagues in the group has shown Q-values of plain resonators of over a million [79]. Another interesting next step would be to incorporate this tunable coupling in a larger quantum network for instance as a tunable coupling between quantum bits.

Appendix A

Cleanroom recipies

A.1   Nb-recipe, sapphire substrate

1. Annealing sapphire substrates

    - 1050°C for 6 h

2. Nb-resonator

    - Sputter Nb, 80 nm
    - Spin resist: S1805, 3000 rpm, 1500 rpm, 45 s
    - Bake 2 min 115°C
    - Exposure, pneumatic focus, Focus:−5 %, Intensity:80 %, Transmission:100 %
    - Develop 40 s in MF319
    - Rinse in water
    - Blowdry
    - Ashing 30 s, 50 W
    - Reactive Ion Etch with NF_3 (50 sccm), laser endpoint detection, around 60 s
    - Ashing 2 min, 50 W, to remove the top layer of the resist.
    - Clean in warm remover $\sim$ 10 min
    - Rinse in IPA
    - Blowdry

3. Au-structures

    - Ashing 2 min, 50 W
    - Spin bottom resist: LOR3A 3000 rpm, 1500 rpm, 45 s
    - Bake 5 min 190°C

- Spin top resist: S1813 3000 rpm, 1500 rpm, 45 s
- Bake 2 min 110°C
- Laser writer exposure, pneumatic focus, Focus:0 %, Intensity:100 %, Transmission:100 %
- Development 60 s in MF319
- Rinse in water
- Blowdry
- Ashing 15 s, 50 W
- Ar-ion etching, 6 min, 300 V, 1 A
- Evaporate, Cr: 2 nm, Au: 110 nm, Pd: 10 nm
- Lift-off in remover, needs a full day or over night
- Rinse in IPA
- Blowdry

4. Lithography, Al-layer

- Ashing 2 min, 50 W
- Spin bottom resist: MMA(8.5)EL10, first step, 500 rpm, 333 rpm, 6 s, second step, 2000 rpm, 400 rpm, 50 s
- Bake 5 min, 170°C
- Spin top resist: ARP6200/2 2:1 500 rpm, 333 rpm, 6 s
- Bake 5 min 160°C
- E-beam exposure, aperture 6, 2 nA, dose: $380 \, \mu C/cm^2$

5. Dicing, without any extra protective layer.

6. Deposition Al-SQUID, two-angle evaporation

- Develop top layer, n-Amylacetate 1 min
- Blowdry
- Develop bottom layer, MIBK/IPA, 5 min (time has to be adjusted for each wafer)
- Quick rinse in IPA
- Blowdry
- Ashing 15 s, 50 W
- Ar-ion etching, two angles ±30°, 1+1 min
- Evaporate, two angles with oxidation in between, ±30°, $30 + 110$ nm, dynamic oxidation 0.2 mbar 30 min
- Lift-off in warm remover, important to add some movement otherwise the Al can collapse onto the surface and stick (see Fig. C.2).
- Clean in IPA
- Blowdry

A.2 Al-recipe, high resistivity silicon substrate

1. Cleaning of high resistivity Silicon

   - Acetone 5 min with ultrasonic 100% normal mode
   - Methanol 5 min with ultrasonic 100% normal mode
   - IPA 5 min with ultrasonic 100% normal mode
   - Standard cleaning 1, 10 min
   - Quick dump rinse (QDR)
   - HF 2% 1 min
   - QDR
   - Blowdry

2. Deposition of aluminum in Plassys

   - Heat to 300°C and keep for 10 min
   - Cool down and pump overnight, pressure $= 6e - 8$ mbar
   - Deposit 150 nm at 1 nm/s
   - Static oxidation 10 mbar, 500 sccm, 10 min

3. Etching of aluminium

   - Spin AZ1512HS at 4000 rpm, 1 min
   - Bake 100°C 50 s
   - Expose in DWL (laser writer), F: -5, I: 80, T: 100
   - Develop AZ Developer:H_2O 1:1 30 s
   - QDR
   - Blowdry
   - Ashing 20 s, 25 W
   - Etch in transene type A 40°C 1 min 5 s
   - QDR
   - Blowdry
   - 1165 85°C 5 min+5 min in ultrasonic 40% sweep mode
   - Methanol with ultrasonic 40% sweep mode
   - IPA with ultrasonic 40% sweep mode
   - Blowdry

4. Deep etching of aluminium and silicon

   - Spin AZ1512HS at 4000 rpm 1 min

- Bake 100°C 50 s
- Expose in DWL, F: −5 %, I: 80 %, T: 100 %
- Develop AZ Developer:H_2O 1:1 30 s
- QDR
- Blowdry
- Ashing 20 s, 25 W
- Etch in transene type A 40°C 1 min 10 s
- QDR
- Blowdry
- Reactive Ion Etch with NF_3
- Ashing 30 s, 50 W
- 1165 85°C 5 min+5 min in ultrasonic 40% sweep mode
- Methanol with ultrasonic 40% sweep mode
- IPA with ultrasonic 40% sweep mode
- Blowdry

5. SQUIDs, cross design

   - Spin Copolymer EL10 3000 rpm 1 min
   - Bake 160°C 5 min
   - Spin PMMA A6 6000 rpm 1 min
   - Bake 160°C 5 min
   - Expose with PEC (ebeam), 2 nA, 800 μC/cm^2
   - Develop MIBK:IPA 1:3 90 s
   - IPA 10 s
   - Blowdry
   - Ashing 20 s, 25 W
   - Load in the Plassys evaporator, align and note planetary angles
   - Deposit 50 nm 1 nm/s at 45° tilt
   - Static oxidation 2 mbar 100 sccm 15 min
   - Rotate stage
   - Deposit 110 nm 1 nm/s at 45° tilt
   - Static oxidation 10 mbar 500 sccm 10 min
   - Lift off in 1165 85°C
   - Fresh 1165 with ultrasonic 40% sweep mode
   - Methanol with ultrasonic 40% sweep mode

- IPA with ultrasonic 40% sweep mode
- Blowdry

6. Plasters

  - Spin Copolymer EL10 3000 rpm 1 min
  - Bake 160°C 5 min
  - Spin PMMA A6 6000 rpm 1 min
  - Bake 160°C 5 min
  - Expose without PEC (ebeam), 35 nA, 700 μC/cm^2
  - Develop MIBK:IPA 1:1 90 s
  - IPA 10 s
  - Blowdry
  - Ashing 20 s, 25 W
  - Ion mill 400 V, 20 mA, 60 V, 3.5 min
  - Deposit 200 nm 1 nm/s
  - Static oxidation 10 mbar 500 sccm 10 min
  - Lift off in 1165 85°C
  - Fresh 1165 with ultrasonic 40% sweep mode
  - Methanol with ultrasonic 40% sweep mode
  - IPA with ultrasonic 40% sweep mode
  - Blowdry

7. Cleave into chips and cleaning

  - Spin S1813 3000 rpm 1 min
  - Bake 110°C 2 min
  - Dice in Disco DAD
  - 1165 85°C for 5 min on hotplate and then 5 min in ultrasonic bath 40% sweep mode
  - Methanol 5 min with ultrasonic 40% sweep mode
  - IPA 5 min with ultrasonic 40% sweep mode
  - Blowdry
  - Ozone 30 min

A.3 Al-recipe, silicon substrate, lift-off recipe

1. Cleaning

   - $10 - 15 \, \text{min}$, remover 1165, $60°$C
   - Ultrasonic bath, 100%, $1 \, \text{min}$
   - IPA bath, $2 \, \text{min}$ circulation
   - QDR bath
   - Blowdry
   - Ashing $1 \, \text{min}$, $50 \, \text{W}$

2. Au-contacts

   - Spin HDMS primer. $3000 \, \text{rpm}$, $1 \, \text{min}$, $t_{acc} = 1.5 \, \text{s}$ bake $1 \, \text{min}$ $110°$C
   - Spin LOR3B, $3000 \, \text{rpm}$, $1 \, \text{min}$, $t_{acc} = 1.5 \, \text{s}$ bake 5min $200°$C
   - Spin S1813, $3000 \, \text{rpm}$, $1 \, \text{min}$, $t_{acc} = 1.5 \, \text{s}$ bake $2 \, \text{min}$ $110°$C
   - Photolithography, exposure $8.5 \, \text{s}$, low-vac mode
   - Development $40 \, \text{s}$, MF319 (lift up after $15 \, \text{s}$)
   - QDR bath+blowdry
   - Deposition, Ti: $30 \, \text{Å}$ ($2 \, \text{Å/s}$) Au: $800 \, \text{Å}$ ($5 \, \text{Å/s}$) Pd: $100 \, \text{Å}$ ($2 \, \text{Å/s}$)
   - Remover 1165, $70°$C, $1 \, \text{h}$ maybe less
   - IPA bath, $2 \, \text{min}$ circulation
   - QDR bath+blowdry

3. Semi-dicing (cut halfway through the wafer)

   - Spin S1813, $3000 \, \text{rpm}$, $1 \, \text{min}$, $1.5 \, \text{s}$ bake $110°$C $3 \, \text{min}$
   - Dicing in the Loadpoint. HUB blade $50 \, \mu\text{m}$, tape thickness $75 \, \mu\text{m}$, wafer thickness $380 \, \mu\text{m}$, depth of cut $0.950 \, \text{mm}$, semidicing $0.725 \, \text{mm}$
   - 1165, $70°$C, rinse with IPA+blowdry
   - Ashing $1 \, \text{min}$, $50 \, \text{W}$

4. SQUIDs, exposure done on full wafer development and evaporation on single chips

   - Spin MMA(8.5)EL10, step one $500 \, \text{rpm}$, $5 \, \text{s}$, $t_{acc} = 2 \, \text{s}$, step two $2000 \, \text{rpm}$, $45 \, \text{s}$, $t_{acc} = 5 \, \text{s}$, bake $5 \, \text{min}$, $170°$C
   - Spin ZEP520A 1:1 anisole, $3000 \, \text{rpm}$, $45 \, \text{s}$, $t_{acc} = 0.5 \, \text{s}$, bake $5 \, \text{min}$ $170°$C
   - Exposure (ebeam)
   - Develop top layer, o-xylene $2 \, \text{min}$
   - IPA rinsing+blowdry
   - Develop bottom layer, H2O IPA 1:4, $5 \, \text{min}$ $30 \, \text{s}$

- Rinse in IPA
- Blowdry gently!
- Evaporation (two-angle) Plassys, 45 nm+55 nm, oxidation at 0.2 mbar, 30 min, angle $\pm 26.5°$
- Remover 1165, 20 min "move" (to get rid of sticking Al) 70°C
- Rinse in IPA

A.4   Nb-recipe, silicon substrate

1. Cleaning

   - Dip in HF bath 30 s to etch oxide
   - QDR bath

2. Sputtering, DCA

   - Load the wafer within 20 min after HF cleaning!
   - Annealing 700°C, 20 min
   - Sputter Nb, 80 nm

3. Lithography

   - Spin resist: UV60-0.75, 3000 rpm, $t_{acc} = 1.5$ s, 1 min , bake 2 min 130°C
   - E-beam exposure, aperture 8, 45 nA, dose: 34
   - Bake 90 s 130°C
   - Develop 55 s MF24A

4. Etching

   - Reactive ion etch with NF_3 plasma (50 sccm), laser endpoint detection, around 40 s
   - To remove redeposited polymer layer, ashing 2 min, 50 W
   - Clean in remover

5. Lithography, Au-layer

   - Spin bottom resist: MMA(8.5)EL10, step one 500 rpm, 5 s, $t_{acc} = 2$ s, step two 2000 rpm, 45 s, $t_{acc} = 5$ s, bake 5 min, 170°C
   - Spin top resist: ARP6200/2 2:1, 3000 rpm, 1 min, $t_{acc} = 1$ s, bake 5 min 160°C
   - E-beam exposure, aperture 8, 70 nA, dose: $280 \, \mu C/cm^2$
   - Develop top layer, n-Amylacetate 2 min
   - Blowdry

- Develop bottom layer, H2O/IPA 1:4, 5 min
- Quick rinse in IPA
- Blowdry

6. Deposition Au-layer

   - Ashing 15 s, 50 W
   - Ar-ion etching, 7 min, 300 V, 1 A
   - Evaporate, Cr: 20 Å, Au: 1100 Å, Pd: 100 Å
   - Lift-off in remover

7. Dice alignment cuts

   - Spin protective resist. S1813, 2000 rpm, 1 min, 1.5 s bake 110°C 3 min
   - Use HUB-blade 50 μm
   - Cut one chip size out from pattern
   - Remove protective resist with remover, rinse with IPA+blowdry

8. Lithography, Al-layer

   - Spin bottom resist: MMA(8.5)EL10 500 rpm, 5 s,$t_{acc} = 2$ s 2000 rpm, 45 s, $t_{acc} = 5$ s bake 5 min, 170°C
   - Spin top resist: ARP6200/2 2:1 3000 rpm, 1 min, $t_{acc} = 1$ s bake 5 min 160°C
   - E-beam exposuree, aperture 6, 2 nA, dose: 300 μC/cm^2

9. Dicing

   - Use the same blade as for alignment dicing
   - Dice the wafer into single chips
   - Carefully remove the chips from the tape

10. Deposition Al-layer

    - Develop top layer, n-Amylacetate 2 min
    - Blowdry
    - Develop bottom layer, H2O/IPA 1:4, 7 min
    - Quick rinse in IPA
    - Blowdry
    - Ashing 15 s, 50 W
    - Ar-ion etching, two angles ±30°, 1+1 min
    - Evaporate, two angles with oxidation in between, ±30°, $30 + 110$ nm, dynamic oxidation 0.2 mbar 15 min
    - Lift-off in remover

Appendix B

Various interesting measurement results

Over the past years I gathered a huge amount of measurement data. Here I show some results that did not make it into the main thesis but make nice figures.
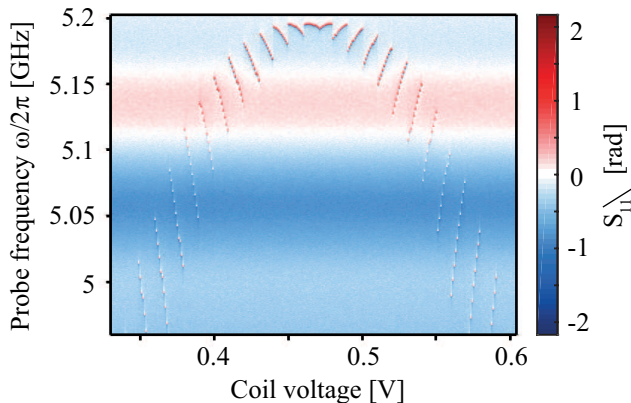
B.1 DC-tuning with parasitic superconducting loops

Figure B.1: *A SQUID-terminated $\lambda/4$-resonator. On the horizontal axis I step the static flux. Instead of a single parabola showing the tuned resonance frequency I found a parabola with a lot of fine structure. Nice picture but not optimal for the experiments I want to do. A further zoom in shows even more fine structures.*

A very interesting effect I have found was the dc tuning of Fig. B.1. This pattern is measured in a typical $\lambda/4$-resonator with a SQUID at the grounded end. The sample

was fabricated using recipe A.1, niobium on sapphire with aluminium SQUIDs. However, what was found is that in the aluminium evaporation, due to the two angle evaporation metal was evaporated on the edges of the chip. Since there is no resist on the edges of the chip this metal was not removed by the lift-off. In conclusion, I had a sample with an additional and big superconducting loop. This superconducting loop also had a weak link, the thin aluminium on the chip edge. I believe that the fine structure in Fig. B.1 was created by fluxes tunnelling in and out of this additional big superconducting loop.

B.2   Stable and unstable resonance

In section 3.4.1 I discuss different aspects of cutting ground planes into pieces versus keeping them continuous and risk trapping magnetic flux in large superconducting loops. In Fig. B.2 I show test measurements of two samples, the design difference between the two is that in (a) all possible superconducting flux traps are cut but in (b) flux can be trapped in big superconducting loops, similar to the drawing in Fig. 3.14.
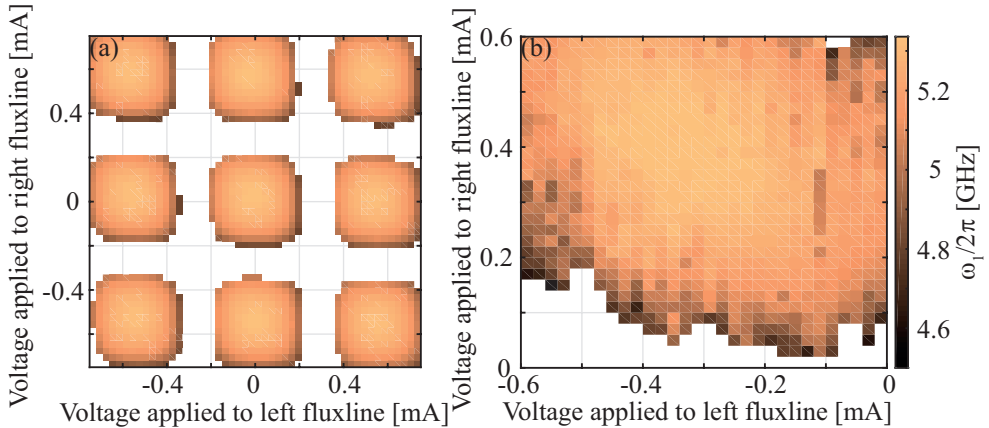

Figure B.2: *(a) dc tuning measurement of a doubly tunable resonator where the ground plane is cut behind all contact pads. (b) dc tuning measurement of a doubly tunable resonator where the ground plane is continuous and forms a superconducting loop around the full sample.*

These two samples and measurement results show two things. First it can be noted that the flux period is much smaller in (a) than in (b). This can be understood by the fact that when keeping the continuous groundplane and form superconducting loops, these loops expel magnetic fields. Another observation is that the extracted resonance frequencies in (b) show a very noisy pattern. In contrast the frequency pattern in (a) looks very stable. My interpretation of this is that the big superconducting loops cause flux trapping and noise.
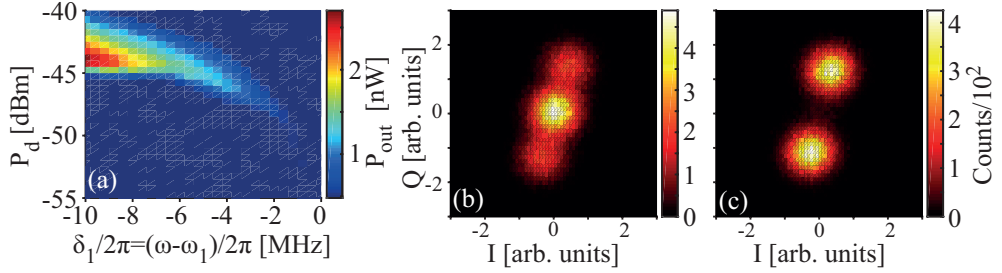
Figure B.3: *Period doubling subharmonic oscillations generated by current driving the SQUID in a $\lambda/4$-resonator. (a) Subharmonic oscillation region. (b) Histogram measured on the lower boundary of the region. (c) Histogram measured in the middle of the region.*

B.3 Period doubling subharmonic oscillations

Figure B.3(a) shows a period doubling subharmonic oscillation region, generated by current driving. Panel (b) and (c) show two quadrature histograms. In resemblance with the pattern for period tripling subharmonic oscillations, the low power boundary of the region shows an additional ground state in the middle. In the middle of the region, the histogram only presents two excited states. This is similar to the theoretical prediction for a parametric oscillator, Fig. 2.24.

The interesting part is that these subharmonic oscillations should not exist. According to theory (table 4.2) only current driving at odd multiples of the resonance frequency should give frequency down-conversion. However, possibly that if we just apply a strong enough drive signal higher order effects occur and period doubling can be observed. It can be noted that the threshold for generating period doubling through current driving is significantly higher than for generating period tripling.

Appendix C

Various fabrication results

Here follows some figures with varying fabrication results in the cleanroom.

C.1   Silicon substrate

When Mathieu Pierre and myself started fabricate samples with niobium on silicon we had some problems with the etching, this is shown in Fig. C.1. The problem was solved by switching the etch substance from CF_4 to NF_3. In Fig. C.2 I show some results from SQUID fabrication.
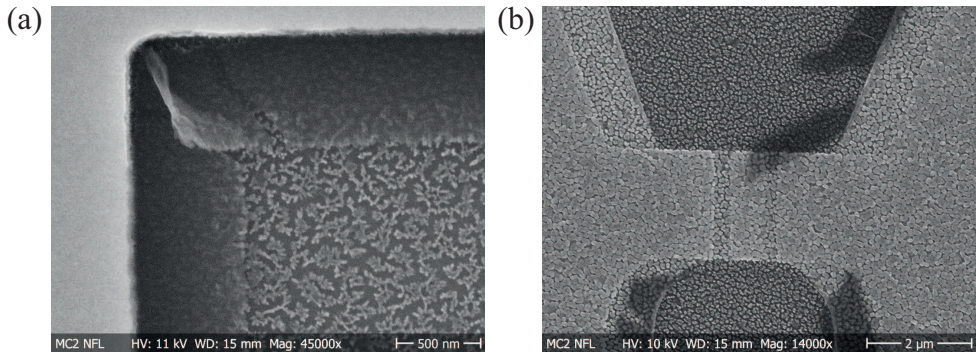

Figure C.1: *(a) Niobium on silicon, physically etched by CF_4. The grains on the substrate could be redeposition of some carbon compound, or something else. The partly transparent thin film could be redeposition of etch waste on the resist walls that does not lift off with the resist. The problem with the grains was solved by changing the etching substance to NF_3. (b) A Josephson junction on a substrate covered with grains (see Fig. C.1). It seems like the grainy structure on the substrate makes the aluminium to form a grainy film. The black shadows could be bad cleaning of the resist, possibly remaining remover or similar.*
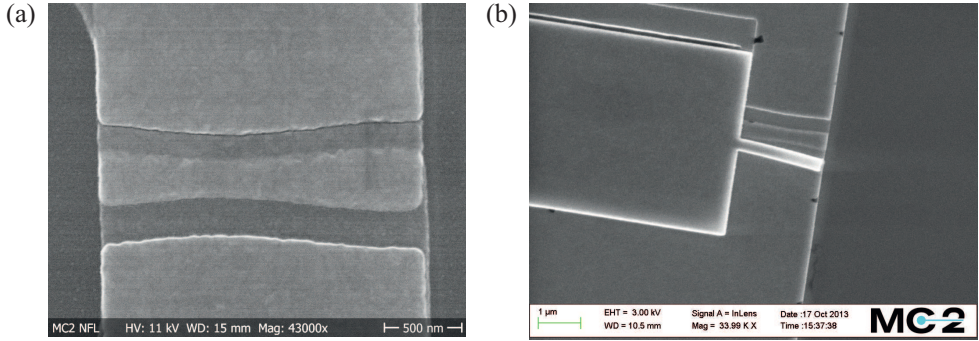
(a) (b)

Figure C.2: *(a)A Josephson junction where the resist bridge has got some damage and caused a waist structure of the junction. This sample is fabricated using recipe A.4. The resonator is made of niobium and then the SQUIDs in aluminium. To ensure good contact between the niobium and aluminium, the niobium oxide is argon-ion-etched. My guess is that the waist structure of the junction is due to either damage from the ion-etch or by violent development. (b) Lift-off problems of the SQUID loop. If lift-off is left unattended the aluminium, supposed to be lifted off, can collapse to the chip surface and stick there. If instead, the lift-off is active and there is some movement in the resist the aluminium is properly lifted. In this case the substrate was silicon.*
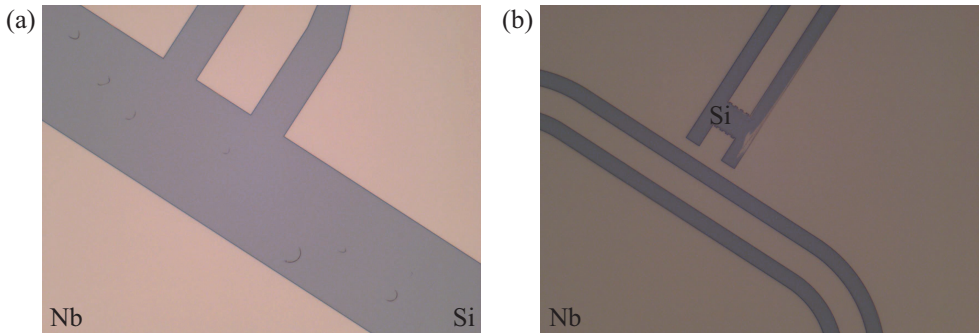

Figure C.3: *Niobium on silicon, after etching and cleaning. In both pictures the grey areas correspond to silicon and the other is niobium. (a) There is something that looks like droplets on the substrate. Unclear what. (b) It looks like the metal has been flowing out.*

C.2   Sapphire ebeam exposure results

Sapphire is an insulating substrate which makes it very sensitive to charging effects. In Fig. C.5, I show two examples of SQUIDs in the making, the pictures are from after ebeam exposure and development. This first example shows a working exposure. In Fig. C.6 I show a second set of pictures illustrating charging effects from an exposure that failed due to lack of grounding path.
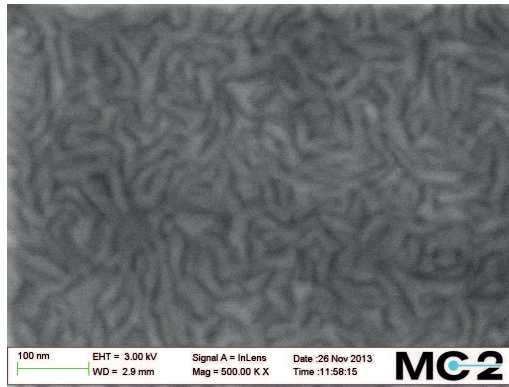
Figure C.4: *Zoom in on a niobium surface.*

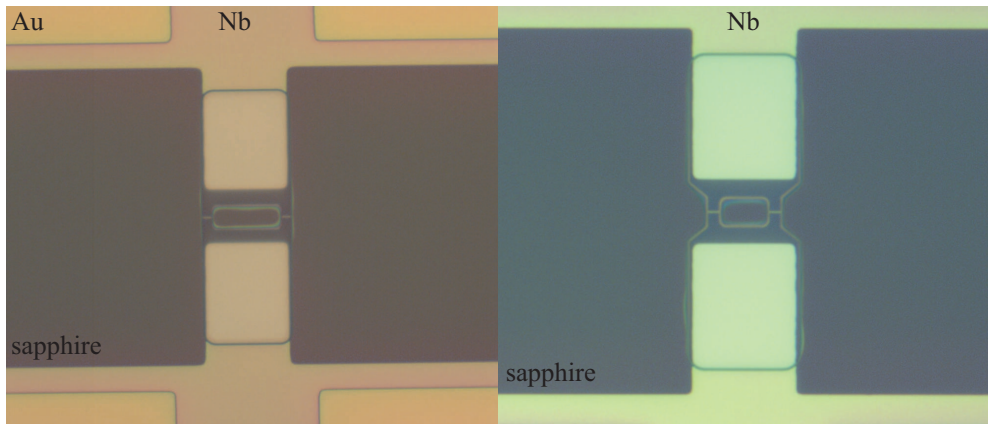Figure C.5: *SQUIDs in the making. This is typically how my resist patter looks after development. Note the nice undercut and that these samples after aluminium evaporation form working SQUIDs. However, apart from the yellowish undercut there is also a more uneven blueish edges. The origin of these uneven edges is unknown but possibly it has to do with charging effects due to the insulating sapphire.*
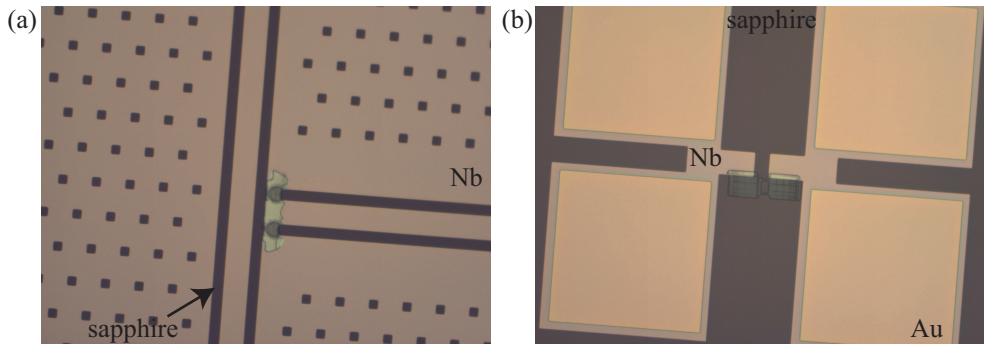
Figure C.6: *This figure shows the results of exposing the SQUIDs on a sapphire wafer, where the Nb has been etched so that each individual chip forms a Nb island. (a) Narrow Nb strip between the resonator and the on-chip flux pump line. I believe this is a charging/heating effect due to current concentration in a narrow strip. (b) SQUID test structure after development. Here, the exposed structure is displaced from its designed position and also underexposed. Probably, due to charging effects, the current beam is slightly misaligned.*
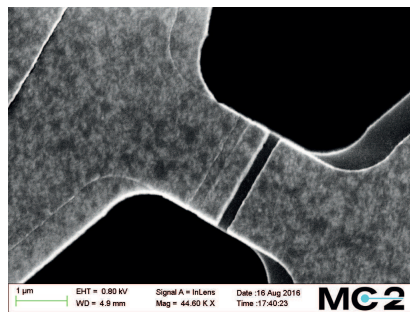

Figure C.7: *Due to the insulating substrate, SEM imaging on sapphire samples is more than difficult than silicon samples. Here I show an example of how a Josephson junction fabricated on a sapphire substrate. The dark shadows that makes the metal look dirty is Espacer, a chemical spun on top of the sample to help with charge distribution.*

Appendix D

Technical aspects of the subharmonic oscillation setup

D.1 Histograms with phase drift
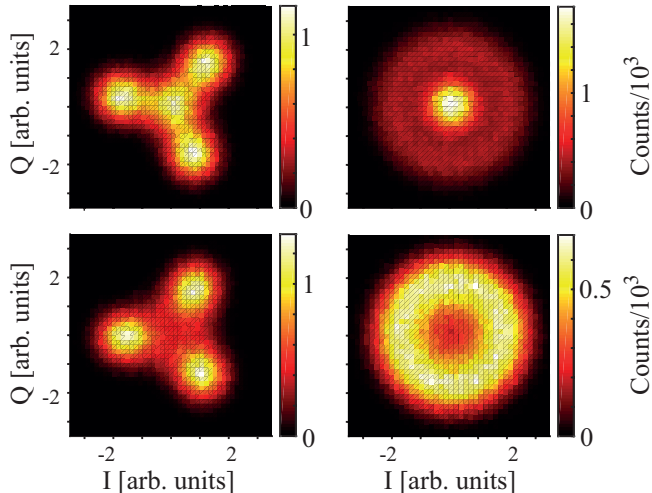
Figure D.1: *To the left, normal histograms. To the right, histograms measured with phase drift.*

Figure D.1 illustrates what happens when the measurement frequency of the digitizer do not match 1/3 of the drive frequency. The measurements are done by driving the SQUID in a $\lambda/4$-resonator at 3ω and measuring at ω. In the two left panels the detection frequency of the digitizer is exactly 1/3 of the signal generator drive frequency. In the two right panels the digitizer frequency, due to limited frequency resolution on the instrument

and that not all numbers are possible to divide by three, has a small mismatch with $1/3$ of the drive frequency.

D.2   Compare a setup with circulators and one with directional coupler

Even though microwave components are rated for a specific frequency range it is usually possible to get a signal through also at a higher frequency. However, there could be extra attenuation, noise and nonlinearity in the response. In the first current driving measurements at 3ω, the setup was not planned with current driving in mind. Therefore, the drive signal was sent through circulators. It worked but with extra attenuation and background ripples. The difference between a measurement with a circulator and a directional coupler setup is illustrated in Fig. D.2. Both measurements are done on exactly the same sample and at the same bias point.
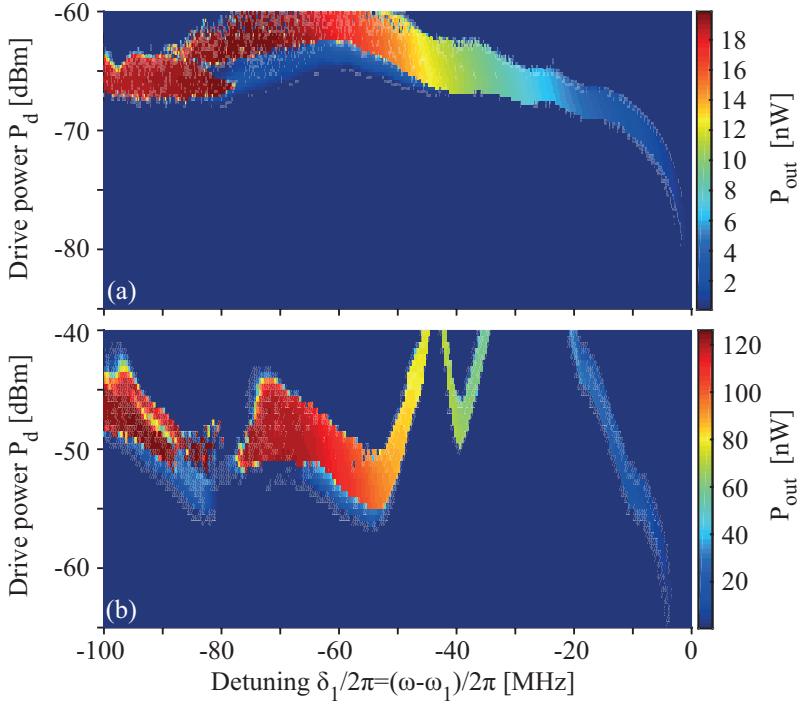

Figure D.2:   *A comparison between a subharmonic oscillation region measured with a (a) directional coupler setup and (b) a circulator setup.*

References

[1]   I.-M. Svensson, A. Bengtsson, P. Krantz, J. Bylander, V. Shumeiko, and P. Delsing. Period-tripling subharmonic oscillations in a driven superconducting resonator. *Physical Review B* **96**: 174503, 2017.

[2]   I.-M. Svensson, A. Bengtsson, J. Bylander, V. Shumeiko, and P. Delsing. Period multiplication in a parametrically driven superconducting resonator. *Submitted manuscript.* arXiv: `1802.09259`.

[3]   I.-M. Svensson, M. Pierre, M. Simoen, W. Wustmann, P. Krantz, A. Bengtsson, J. Bylander, V. Shumeiko, and P. Delsing. Microwave photon generation in a doubly tunable superconducting resonator. *Journal of Physics: Conference series* **969**: 1146, 2018.

[4]   J. Lindkvist, C. Sabín, I. Fuentes, A. Dragan, I.-M. Svensson, P. Delsing, and G. Johansson. Twin paradox with macroscopic clocks in superconducting circuits. *Physical Review A* **90**: 052113, 2014.

[5]   M. Pierre, I.-M. Svensson, S. Raman Sathyamoorthy, G. Johansson, and P. Delsing. Storage and on-demand release of microwaves using superconducting resonators with tunable coupling. *Applied Physics Letters* **104**: 232604, 2014.

[6]   M. Pierre, S. Sathaymoorty, I.-M. Svensson, P. Delsing, and G. Johansson. Resonant and off-resonant microwave signal manipulations in coupled superconducting resonators. *Submitted manuscript.* arXiv: `1802.09034`.

[7]   A. Bengtsson, P. Krantz, M. Simoen, I.-M. Svensson, B. H. Schneider, V. Shumeiko, P. Delsing, and J. Bylander. Nondegenerate parametric oscillations in a tunable superconducting resonator. *Submitted manuscript.* arXiv: `1801.04566`.

[8]   B. H. Schneider, A. Bengtsson, I.-M. Svensson, T. Aref, G. Johansson, J. Bylander, and P. Delsing. Observation of broadband entanglement in radiation from the dynamical Casimir effect. *Submitted manuscript.* arXiv: `1802.05529`.

[9]   M. Planck. Ueber das Gesetz der Energieverteilung im Normalspectrum. *Annalen der Physik* **309**: 553, 1901.

[10] G. Lewis. The conservation of photons. *Nature* **118**: 874, 1926.

[11] A. Einstein. Über einen die Erzeugung und Verwandlung des Lichtes betreffenden heuristischen Gesichtspunkt. *Annalen der Physik* **322**: 132, 1905.

[12] S. Haroche and D. Kleppner. Cavity quantum electrodynamics. *Physics Today* **42**: 24, 1989.

[13] A. Blais, R.-S. Huang, A. Wallraff, S. M. Girvin, and R. J. Schoelkopf. Cavity quantum electrodynamics for superconducting electrical circuits: An architecture for quantum computation. *Physical Review A* **69**: 062320, 2004.

[14] A. Wallraff, D. I. Schuster, A. Blais, L. Frunzio, R.-S. Huang, J. Majer, S. Kumar, S. M. Girvin, and R. J. Schoelkopf. Strong coupling of a single photon to a superconducting qubit using circuit quantum electrodynamics. *Nature* **431**: 162, 2004.

[15] R. J. Schoelkopf and S. M. Girvin. Wiring up quantum systems. *Nature* **451**, 2008.

[16] X. Gu, A. F. Kockum, A. Miranowicz, Y.-X. Liu, and F. Nori. Microwave photonics with superconducting quantum circuits. *Physics Reports*, 2017.

[17] M. Sandberg, C. M. Wilson, F. Persson, T. Bauch, G. Johansson, V. Schumeiko, T. Duty, and P. Delsing. Tuning the field in a microwave resonator faster than the photon lifetime. *Applied Physics Letters* **92**: 203501, 2008.

[18] A. Palacios-Laloy, F. Nguyen, F. Mallet, P. Bertet, D. Vion, and D. Esteve. Tunable Resonators for Quantum Circuits. *Journal of Low Temperature Physics* **151**: 1034, 2008.

[19] G. Tancredi, G. Ithier, and P. Meeson. Bifurcation, mode coupling and noise in a nonlinear multimode superconducting microwave resonator. *Applied Physics Letters* **103**: 063504, 2013.

[20] C. W. Sandbo Chang, M. Simoen, J. Aumentado, C. Sabín, P. Forn-Díaz, A. M. Vadiraj, F. Quijandría, G. Johansson, I. Fuentes, and C. M. Wilson. Generating multimode entangled microwaves with a superconducting parametric cavity. arXiv: `1709.00083`.

[21] I.-M. Svensson. "Photon generation in a doubly tunable resonator". MA thesis. Chalmers university of technology, 2012.

[22] M. Simoen. "Parametric interactions with signals and the vacuum". PhD thesis. Chalmers university of technology, 2015.

[23] W. Wustmann and V. Shumeiko. Nondegenerate Parametric Resonance in a Tunable Superconducting Cavity. *Physical Review Applied* **8**: 024018, 2017.

[24] W. Wustmann and V. Shumeiko. Parametric resonance in tunable superconducting cavities. *Physical Review B* **87**: 184501, 2013.

[25] P. Krantz. "The Josephson parametric oscillator - From microscopic studies to single-shot qubit readout". PhD thesis. Chalmers university of technology, 2016.

[26] T. V. Duzer and C. W. Turner. *Principles of Superconductive Devices and Circuits.* Prentice Hall PTR, 1999.

[27] H. K. Onnes. *The Superconductivity of Mercury.* Tech. rep. Comm. Phys. Lab. Univ. Leiden, 1911.

[28] L. N. Cooper. Bound Electron Pairs in a Degenerate Fermi Gas. *Physical Review* **104**: 1189, 1956.

[29] J. Bardeen, L. N. Cooper, and J. R. Schrieffer. Theory of superconductivity. *Physical Review* **108**: 1175, 1957.

[30] W. Meissner and R. Ochsenfeld. Ein neuer effekt bei eintritt der supraleitfähigkeit. *Naturwissenschaften* **21**: 787, 1933.

[31] B. D. Josephson. Possible new effects in superconductive tunneling. *Physics Letters*, 1962.

[32] F. London and H. London. The Electromagnetic Equations of the Supraconductor. *Proceedings of the Royal Society of London. Series A, Mathematical and Physical Sciences* **149**: 71, 1935.

[33] K. Bladh, T. Duty, D. Gunnarsson, and P. Delsing. The single Cooper-pair box as a charge qubit. *New Journal of Physics*, 2005.

[34] C. Fabry and A. Perot. Theorie et applications d'une nouvelle methode de spectroscopie interferentielle. *Annales de Chimie et de Physique* **16**: 115, 1899.

[35] C. P. Wen. Coplanar Waveguide: A Surface Strip Transmission Line Suitable for Nonreciprocal Gyromagnetic Device Applications. *Microwave Theory and Techniques, IEEE Transactions on* **17**, 1969.

[36] K. Watanabe, K. Yoshida, T. Aoki, and S. Kohjiro. Kinetic Inductance of Superconducting Coplanar Waveguides. *Japanese Journal of Applied Physics* **33**: 5708, 1994.

[37] S. Gevorgian, T. Martinsson, P. Linner, and E. Kollberg. CAD models for multilayered substrate interdigital capacitors. *Microwave Theory and Techniques, IEEE Transactions on* **44**, 1996.

[38] M. Göppl, A. Fragner, M. Baur, R. Bianchetti, S. Filipp, J. M. Fink, P. J. Leek, G. Puebla, L. Steffen, and A. Wallraff. Coplanar waveguide resonators for circuit quantum electrodynamics. *Journal of Applied Physics* **104**, 2008.

[39] D. M. Pozar. *Microwave Engineering 3rd edition*. Wiley, 2005.

[40] S. de Graaf. "Fractal superconducting resonators for the interrogation of two-level systems". PhD thesis. Chalmers university of technology, 2014.

[41] J. Burnett. "High precision readout of superconducting resonators : For analysis of slow noise processes". PhD thesis. Royal Holloway University of London, 2014.

[42] A. D. O'Connell, M. Ansmann, R. C. Bialczak, M. Hofheinz, N. Katz, E. Lucero, C. McKenney, M. Neeley, H. Wang, E. M. Weig, A. N. Cleland, and J. M. Martinis. Microwave dielectric loss at single photon energies and millikelvin temperatures. *Applied Physics Letters* **92**: 112903, 2008.

[43] C. Müller, J. H. Cole, and J. Lisenfeld. Towards understanding two-level-systems in amorphous solids-Insights from quantum devices, 2017.

[44] J. Burnett, T. Lindström, M. Oxborrow, Y. Harada, Y. Sekine, P. Meeson, and A. Y. Tzalenchuk. Slow noise processes in superconducting resonators. *Physical Review B* **87**: 140501, 2013.

[45] H. Wang, M. Hofheinz, J. Wenner, M. Ansmann, R. C. Bialczak, M. Lenander, E. Lucero, M. Neeley, A. D. O'Connell, D. Sank, M. Weides, A. N. Cleland, and J. M. Martinis. Improving the coherence time of superconducting coplanar resonators. *Applied Physics Letters* **95**: 233508, 2009.

[46] B. Yurke and J. S. Denker. Quantum network theory. *Physical Review A* **29**: 1419, 1984.

[47] M. Wallquist, V. S. Shumeiko, and G. Wendin. Selective coupling of superconducting charge qubits mediated by a tunable stripline cavity. *Physical Review B* **74**: 224506, 2006.

[48] J. Bourassa, F. Beaudoin, J. M. Gambetta, and A. Blais. Josephson-junction-embedded transmission-line resonators: From Kerr medium to in-line transmon. *Physical Review A* **86**: 013814, 2012.

[49] M. I. Dykman, C. M. Maloney, V. N. Smelyanskiy, and M. Silverstein. Fluctuational phase-flip transitions in parametrically driven oscillators. *Physical Review E* **57**: 5202, 1998.

[50] J. R. Johansson, G. Johansson, C. M. Wilson, and F. Nori. Dynamical Casimir Effect in a Superconducting Coplanar Waveguide. *Physical Review Letters* **103**: 147003, 2009.

[51] J. R. Johansson, G. Johansson, C. M. Wilson, and F. Nori. Dynamical Casimir effect in superconducting microwave circuits. *Physical Review A* **82**: 052509, 2010.

[52] Y. Zhang, J. Gosner, S. M. Girvin, J. Ankerhold, and M. I. Dykman. Time-translation-symmetry breaking in a driven oscillator: From the quantum coherent to the incoherent regime. *Physical Review A* **96**: 052124, 2017.

[53] K. Banaszek and P. L. Knight. Quantum interference in three-photon down-conversion. *Physical Review A* **55**: 2368, 1997.

[54] T. Felbinger, S. Schiller, and J. Mlynek. Oscillation and Generation of Nonclassical States in Three-Photon Down-Conversion. *Physical Review Letters* **80**: 492, 1998.

[55] S. T. Gevorkyan and V. O. Chaltykyan. Coherent superposition states of light and their interference in three-photon absorption process. *Journal of Modern Optics* **46**: 1447, 1999.

[56] C. Hayashi. *Nonlinear Oscillations in Physical Systems*. Princeton, 1985.

[57] D. W. Jordan and P. Smith. *Nonlinear Ordinary Differential Equations*. Oxford, 2007.

[58] C. M. Wilson, T. Duty, M. Sandberg, F. Persson, V. Shumeiko, and P. Delsing. Photon Generation in an Electromagnetic Cavity with a Time-Dependent Boundary. *Physical Review Letters* **105**: 233907, 2010.

[59] P. Krantz, Y. Reshitnyk, W. Wustmann, J. Bylander, S. Gustavsson, W. D. Oliver, T. Duty, V. Shumeiko, and P. Delsing. Investigation of nonlinear effects in Josephson parametric oscillators used in circuit quantum electrodynamics. *New Journal of Physics* **15**: 105002, 2013.

[60] A. Lambrecht, M.-T. Jaekel, and S. Reynaud. Motion Induced Radiation from a Vibrating Cavity. *Physical Review Letters* **77**: 615, 1996.

[61] A. Lambrecht, M. T. Jaekel, and S. Reynaud. Frequency up-converted radiation from a cavity moving in vacuum. *European Physics Journal D* **3**, 1998.

[62] J.-Y. Ji, H.-H. Jung, and K.-S. Soh. Interference phenomena in the photon production between two oscillating walls. *Physical Review A* **57**: 4952, 1998.

[63] D. A. R. Dalvit and F. D. Mazzitelli. Creation of photons in an oscillating cavity with two moving mirrors. *Physical Review A* **59**: 3049, 1999.

[64] V. V. Dodonov. Resonance photon generation in a vibrating cavity. *J. Phys. A-Math. Gen.* **31**: 9835, 1998.

[65] C. M. Wilson, G. Johansson, A. Pourkabirian, M. Simoen, J. R. Johansson, T. Duty, F. Nori, and P. Delsing. Observation of the Dynamical Casimir Effect in a Superconducting Circuit. *Nature* **479**: 376, 2011.

[66] A. Einstein. Zur elektrodynamik bewegter körper. *Annalen der physik* **322**: 891, 1905.

[67] W. Rindler. *Relativity: Special, General, and Cosmological*. Oxford University Press, 2006.

[68] E. Zakka-Bajjani, F. Nguyen, M. Lee, L. R. Vale, R. W. Simmonds, and J. Aumentado. Quantum superposition of a single microwave photon in two different "colour" states. *Nature Physics* **7**: 599, 2011.

[69] Y. Yin, Y. Chen, D. Sank, P. J. J. O'Malley, T. C. White, R. Barends, J. Kelly, E. Lucero, M. Mariantoni, A. Megrant, C. Neill, A. Vainsencher, J. Wenner, A. N. Korotkov, A. N. Cleland, and J. M. Martinis. Catch and Release of Microwave Photon States. *Physical Review Letters* **110**: 107001, 2013.

[70] A. J. Sirois, M. A. Castellanos-Beltran, M. P. DeFeo, L. Ranzani, F. Lecocq, R. W. Simmonds, J. D. Teufel, and J. Aumentado. Coherent-state storage and retrieval between superconducting cavities using parametric frequency conversion. *Applied Physics Letters* **106**: 172603, 2015.

[71] E. Flurin, N. Roch, J. D. Pillet, F. Mallet, and B. Huard. Superconducting Quantum Node for Entanglement and Storage of Microwave Radiation. *Physical Review Letters* **114**: 090503, 2015.

[72] W. Pfaff, C. J. Axline, L. D. Burkhart, U. Vool, P. Reinhold, L. Frunzio, L. Jiang, M. H. Devoret, and R. J. Schoelkopf. Controlled release of multiphoton quantum states from a microwave cavity memory. *Nature Physics* **13**: 882, 2017.

[73] F. Cuccureddu, S. Murphy, I. Shvets, M. Porcu, H. Zandbergen, N. Sidorov, and S. Bozhko. Surface morphology of c-plane sapphire (α-alumina) produced by high temperature anneal. *Surface Science* **604**: 1294, 2010.

[74] A. Megrant, C. Neill, R. Barends, B. Chiaro, Y. Chen, L. Feigl, J. Kelly, E. Lucero, M. Mariantoni, P. J. J. O'Malley, D. Sank, A. Vainsencher, J. Wenner, T. C. White, Y. Yin, J. Zhao, C. J. Palmstrøm, J. M. Martinis, and A. N. Cleland. Planar superconducting resonators with internal quality factors above one million. *Applied Physics Letters* **100**, 113510, 2012.

[75] R. Barends, N. Vercruyssen, A. Endo, P. J. de Visser, T. Zijlstra, T. M. Klapwijk, P. Diener, S. J. C. Yates, and J. J. A. Baselmans. Minimal resonator loss for circuit quantum electrodynamics. *Applied Physics Letters* **97**: 023508, 2010.

[76] A. Bruno, G. de Lange, S. Asaad, K. L. van der Enden, N. K. Langford, and L. DiCarlo. Reducing intrinsic loss in superconducting resonators by surface treatment and deep etching of silicon substrates. *Applied Physics Letters* **106**: 182601, 2015.

[77] W. A. Phillips. Two-level states in glasses. *Reports on Progress in Physics* **50**: 1657, 1987.

[78] L. Guo, M. Marthaler, and G. Schön. Phase Space Crystals: A New Way to Create a Quasienergy Band Structure. *Physical Review Letters* **111**: 205303, 20 2013.

[79] J. Burnett, A. Bengtsson, D. Niepce, and J. Bylander. Noise and loss of superconducting aluminium resonators at single photon energies. *To be published in Journal of Physics Conference series*, 2018.